Enhancement of Fluorescence-Based Immunoassay for Point-of-Care Testing Using the Plasmonic Nanopatch Metasurface

by

Daniela Cruz

Department of Biomedical Engineering
Duke University

Date:_____
Approved:

_____
Maiken Mikkelsen, Advisor

_____
Tuan Vo-Dinh

_____
Ashutosh Chilkoti

_____
Jennifer West

_____
Roarke Horstmeyer

Dissertation submitted in partial fulfillment of
the requirements for the degree of Doctor
of Philosophy in the Department of
Biomedical Engineering in the Graduate School
of Duke University

2020

ABSTRACT

Enhancement of Fluorescence-Based Immunoassay for Point-of-Care Testing Using the Plasmonic Nanopatch Metasurface

by

Daniela Cruz

Department of Biomedical Engineering
Duke University

Date:_____
Approved:

_____
Maiken Mikkelsen, Advisor

_____
Tuan Vo-Din, Chair

_____
Ashutosh Chilkoti

_____
Jennifer West

_____
Roarke Horstmeyer

An abstract of a dissertation submitted in partial fulfillment of the requirements for the degree of Doctor of Philosophy in the Department of Biomedical Engineering in the Graduate School of Duke University

2020

Abstract

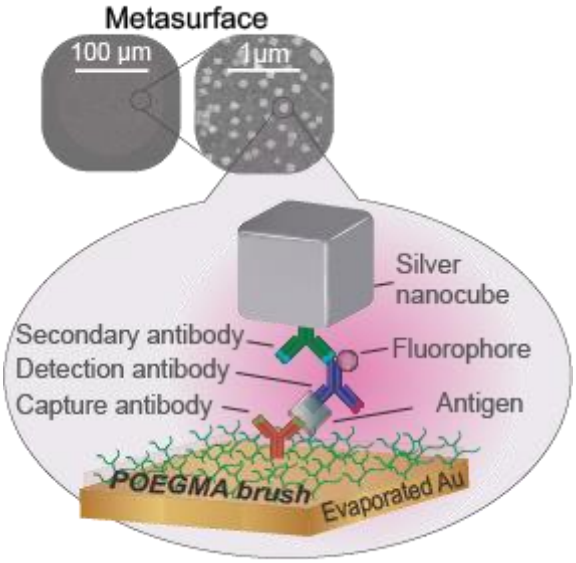

Figure 1: Integration of a plasmonic metasurface with a sandwich immunoassay

Fluorescence-based methodologies have been used extensively for biosensing and to analyze molecular dynamics and interactions. An emerging, promising diagnostic tool are fluorescence-based microarrays due to their high throughput, small sample volume and multiplexing capabilities. However, their low fluorescence output has limited their implementation for in vitro diagnostics applications in a point-of-care (POC) setting. Here, by integration of a sandwich immunoassay microarray within a plasmonic nanogap metasurface, we demonstrate strongly enhanced fluorescence enabling readout by a fluorescence microarray even at low sensitivities. We have named this plasmonic architecture the plasmonically enhanced D4 (PED4) assay. The immunoassay consists of

inkjet-printed capture and fluorescently labeled detection antibodies on a polymer brush which is grown on a gold film. Colloidally synthesized silver nanocubes (SNCs) are placed on top of the brush through a polyelectrolyte layer and interacts with the underlying gold film creating a nanogap plasmonic structure supporting local electromagnetic field enhancements of ~100-fold. By varying the thickness of the brush between 5 and 20 nm, a 151-fold increase in fluorescence and a 14-fold improvement in the limit-of-detection (LOD) is observed for the cardiac biomarker B-type natriuretic peptide (BNP) compared to the unenhanced assay, paving the way for a new generation of point-of-care clinical diagnostics.

To move the PED4 towards a single step point of care test (POCT), SNCs are conjugated with a secondary antibody that attaches specifically to the detection antibody. This allows SNCs to deposit on the surface without the need of a charged polyelectrolyte layer. In addition, multiplexing capabilities are demonstrated in this plasmonic platform where NT-proBNP, Galectin-3, and NGAL are simultaneously detected and fluorescently enhanced. Microfluidics integration and use of a low-cost detector is also demonstrated.

Dedication

To my mom Leonor, whose many sacrifices allowed us to follow our dreams.

Contents

List of Tables

List of Figures

Acknowledgements

Working as a graduate student in the Biomedical Engineering department at Duke has been an incredible learning journey. I am extremely grateful for the opportunity to be part of a scientific community that highly values interdisciplinary collaboration for the advancement of human health.

First and foremost, I would like to thank my advisor Dr. Maiken Mikkelsen for her insightful advice and for giving me the opportunity to be part of her lab to pursue my PhD. Maiken's devotion and dedication to science and engineering are truly inspiring; and I am grateful for all her teachings, the most central which are hard work, integrity, and persistence. I would also like to thank all the members in my committee for their time and expertise. I would like to thank Dr. Tuan Vo-Dinh for his devotion towards the photonics community. I thank Dr. Ashutosh Chilkoti for his immeasurable advice and feedback while collaborating with his group. I thank Dr. Jennifer West for her advice and inspiring commitment towards outreach and minority inclusion in the Pratt School of Engineering. I thank Dr. Roarke Horstmeyer for his mentorship, and I thank Dr. Gabriel López for his advice, encouragement, and guidance during my first two years in graduate school.

In addition, I would like to thank all the members of my lab. I thank Dr. Jiani Huang for being so sweet and patient when introducing me to the procedures in the lab and for her valuable advice. In addition, I thank Dr. Thang Hoang and Dr. Gleb Akselrod for their teachings in optics and experimentation procedures. I thank Jon Stewart for the

insightful academic conversations and his feedback while performing experiments. I would like to thank Dr. Andrew Traverso for his help, advice, and feedback. And I thank Qixin Shen, Wade Wilson, Andrew Boyce, Nathan Wilson, Dr. Tao Cai, and Tamra Nebabu for sharing their knowledge and their friendship inside and outside the lab. Additionally, I would like to thank members in the López lab including Alice Li, Wei Han, Phanindhar Shivapooja, Vrad Levering, Ali Ghoorchian, and Lizzy Szott. Specially I would like to thank Korine Ohiri for the encouragement and for the insightful conversations about life and research; and Wyatt Shields for inspiring me to be a better scientist.

Finally, I would like to thank my family and friends for their support and encouragement. Foremost, I would like to thank my mom Leonor Ordóñez for her love, words of encouragement, and valuable advice. I simply would not have been able to complete my dreams without her. I thank my dad Jorge Cruz for his words of wisdom and insightful conversations. I thank my brother Jorge Cruz for being a role model and for showing me how to work hard and persevere; and my twin sister Pamela Cruz for always being there for me. I also thank my stepdad Harvey Bass for his love, help, and patience. In addition, I would like to thank my partner Michael Herrera for filling my life with music and for teaching me about the important things in life. I thank my good friend Laura Pulido for the laughs and the great memories in grad school. And I thank the Latin-dancing community in Durham for offering a space to unwind.

Chapter 1 Introduction

1.1 Introduction

Fluorescent protein microarrays represent a promising platform for POC testing due to low fabrication cost, straightforward multiplexing, and the need for low sample volumes[1-4]. Significant progress has been made in the fabrication of microarrays, by optimization of their performance through immobilization strategies[5,6], miniaturization[7], and automation[8]. The need for multiple washing and incubation steps, which is incompatible with POCT, has recently been overcome with the D4 assay where the capture and fluorescently labeled detection antibodies are inkjet printed on a stealth protein and cell resistant polymer brush namely poly(oligo(ethylene glycol) methacrylate (POEGMA) that is grafted from the surface of glass through surface initiated atom transfer radical polymerization (SI-ATRP). Incubation of this chip with a drop of biological fluid results in the appearance of discrete fluorescent spots, the intensity of which correlates with analyte concentration[9]. However, the readout of the assay is still severely limited by the fluorescence signal and typically requires the use of expensive and bulky table-top detectors. Attempts at readout using a detector compatible with POCT showed that this resulted in a deterioration of the LOD by ~20-fold[9] underscoring the need for strategies to enhance the assay's fluorescence output. As it will be described in Chapter 2, plasmonics provides a possible solution to this challenge, as plasmonic nanostructures can concentrate light into small volumes and yield high field

enhancements or “hot spots” that can enhance the efficiency of optical excitation and emission processes of emitters[10–12].

In the past, plasmonic platforms have shown enhancements that are high enough to detect single molecules[13] and plasmonic metasurfaces have been used for phase interrogation[14,15], however, their utilization as POCTs is limited as they often are not scalable and need intricate fabrication and functionalization steps[16,17]. For instance, Yesilkoy et al. showed the use of a plasmonic metasurface composed of nanoholes along with large field-of-view interferometric lens-free imaging reader for the phase-sensitive biosensing of proteins (IgG)[14]. However, the limit of detection in their study is significant and impractical for POC testing. Another recent example is the use of a Polydimethylsiloxane (PDMS) stamp for the deposition of nanoparticles on an arbitrary surface, representing a simple "add-on" to an immunoassay[18]. Although the sensitivity and fluorescence enhancement of this system are increased by a factor of 100, it would be difficult to apply to substrates that need multiple readings, such as the case of 96-well plates since the user would have to cut the plasmonic patch and add each patch on each well. This fact would also make the system difficult to incorporate in microfluidics applications and thus POC testing.

This thesis explores the use of the plasmonic nanopatch antenna as a fluorescence enhancer in the D4 assay and it investigates means to translate the system into a point-of-care test for clinical use, a feat that remains challenging in microarray immunoassays.

1.2 Organization

This dissertation is organized as follows. Chapter 2 focuses on fluorescence in biosensing and diagnostic technologies and provides an introduction two main components used in the development of the PED4: 1) the non-fouling polymer surface POEGMA and 2) the plasmonic nanopatch antenna. In Chapter 3, fabrication of the PED4 using a polyelectrolyte layer is introduced and difference in fluorescence enhancement is demonstrated for varying thickness of the polymer brush. In Chapter 4, efforts to move the PED4 towards a POCT are shown such as particle functionalization, detection with inexpensive components, and integration in a microfluidic chip. Chapter 5 further demonstrates the clinical value of the PED4 by adding multiplexing capabilities to the system, where three biomarkers can simultaneously be detected and enhanced. Chapter 6 discusses future directions that can lead to higher enhancements and assay performance in the PED4, as well as ways to translate the system for clinical use.

Chapter 2 Background on protein microarrays fluorescence enhancement through plasmonics

2.1 Overview

The work presented in this thesis amalgamates two state of the art technologies: 1) the D4 assay and 2) the nanopatch antenna metasurface. This chapter provides with an introduction to these technologies and how their individual properties attribute to the overall performance of the plasmonically enhanced D4 assay. First, an introduction to non-fouling surfaces is provided, with a focus on the POEGMA polymer brush. Then, protein microarrays and their advancement towards clinical applications is discussed with a focus on the D4 assay. An introduction to plasmonics is then given, emphasizing on their ability to enhance physical properties of molecules such as fluorophores. Then an overview of plasmonic biosensors is provided by focusing on its two main classes: surface plasmon resonance (SPR) and localized surface plasmon resonance (LSPR). A detailed description of the plasmonic nanopatch antenna is also provided, followed with a discussion on its fluorescence enhancing properties and its use as a plasmonic metasurface. Finally, we discuss a few examples of plasmonic microarray technologies and how the PED4 can outperform in the clinical setting.

2.2 Non-fouling surfaces and the POEGMA polymer brush.

Non-fouling materials have become ubiquitous in the medical field to prevent the non-specific binding of proteins and cells in *in vivo* systems such as drug delivery carriers and implants, and *in vitro* systems such and diagnostic biosensors[19]. *In vivo* non-

fouling materials are beneficial in implantable devices as they resist inflammatory responses such as tissue fibrosis and infection, which can compromise the effectiveness of an implanted device and the patient's outcome[20]. In the case of diagnosis devices, reduction of non-specific protein binding allows for an increase in analytical sensitivity[21]. Poly (ethylene glycol) (PEG) has become the gold standard in materials resisting protein adhesion. However, these are subject to oxidation and present low stability[22]. Other classes of antifouling materials have been investigated, that can be divided into polyhydrophilic (PEG, polysaccharides, and polyamides) and polyzwitterionic materials (polymer with positive and negative charge). The basic mechanism in antifouling surfaces is their minimization of the intermolecular interaction forces between molecules in proteins or cells and the surface[21]. This is done through a tight bond water layer (hydration layer) that creates a physical and energetic barrier to prevent protein adsorption on the surface.

In addition to surface hydration, surface modification and packing play important roles in achieving non-fouling properties of a surface. This can be obtained in self-assembled monolayers (SAMs), "grafted-from-surface" polymers via surface-initiated atom transfer radical polymerization (ATRP), and in "graft-to-surface" polymers via dipping, cross-linking, or reaction of the specific groups of polymers with substrate[23]. Research by Whitesides[24] *et. al* for example, showed that short-chain hydrophilic SAMs are well suitable platforms for protein unbinding due to their high surface density. However, this packed density brings rigidity to the chains, which compromise their flexibility and ability for steric repulsion[25]. Also, SAMs have the propensity to create

imperfections, and therefore they do not have the same degree of robustness as polymers[26,27]. As an alternative, atom transfer radical polymerization (ATRP) can also create high density coatings such as SAMs, but with thicker, and robust polymer films. In addition to surface hydration, these also present chain flexibility. This means that when a protein approaches the surface, the compression of the polymer chains causes steric repulsion to resist protein adsorption[28,29]. In this study, ATRP was used as a method for polymer growth due to the high polymer coverage it produces, its high control over growth kinetics, and because it is easy to perform.

ATRP has been used to grow an oligo(ethylene glycol) $(EG)_n$ – functionalized polymer brush of tunable thickness (5-50nm range) on silicon oxide and gold[30–32]. To perform ATRP of oligo(ethylene glycol) methyl methacrylate (OEGMA) on glass and silicon oxide, slides were first functionalized with the silane initiator (3-Aminopropyl)triethoxysilane, also known as APTES to form an amine-terminated self-assembled monolayer . The slides were then modified to present an ATRP initiator by immersing them in a solution of bromoisobutyryl bromide (1%) and triethylamine (1%) in dichloromethane, which allows the initiator bromoisobutyryl bromide to attach to the amine groups. Finally, slides were submerged in a degassed polymerization solution of Cu(I)Br, bipyridine, and oligo(ethylene glycol) methacrylate (M_n = 300 mg mL^{-1}) under argon to synthesize surface-tethered brushes of POEGMA[33], as seen in **Figure 2**.

Figure 2: SI-ATRP of oligo(ethylene glycol) methyl methacrylate (OEGMA) on glass and silicon oxide. Slides are first functionalized with a silane initiator (1) followed by their modification to present an ATRP initiator (2). Finally, slides were submerged in a degassed polymerization solution under argon to grow the polymer brush (3).

A slightly different approach is taken when polymerizing on a gold surface. In this case, a bifunctional molecule is used as the initiator, where an ATRP initiator is at one end (bromoisobutyrate moiety) and a thiol group on the other end. The same polymerization procedure as that of glass is taken for gold. In the case of the experiments performed for this dissertation, the thiol initiator used was that of Bis[2-(2'-bromoisobutyryloxy)ethyl]disulfide. **Figure 3** shows the polymerization growth for our experiments, where different polymer thicknesses ranging from 3nm-50nm were obtained by increasing the polymerization time. This figure shows a single polymerization run where error bars reflect the standard deviation across five different spots on the sample, showing the high level of thickness control in each slide necessary for the experiments.

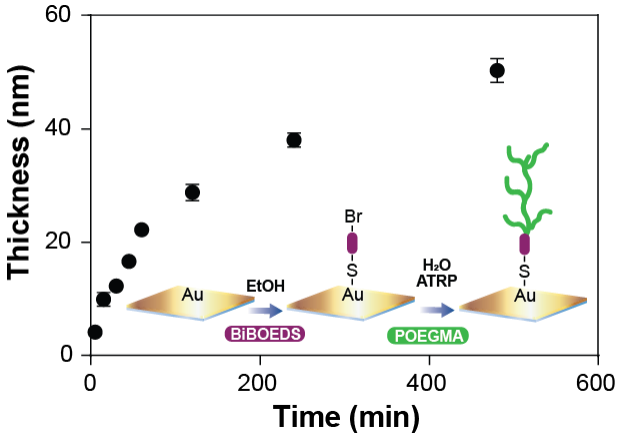

Figure 3: Thickness of POEGMA brush on gold by ATRP as a function of polymerization time. The POEGMA brush thickness was measured by ellipsometry. The schematics in the figure shows the steps of the process, where a dislfide-terminated ATRP initiator Bis[2-(2'-bromoisobutyryloxy)ethyl]disulfide (BiBOEDS) forms a self-assembled monolayer on gold, and subsequent ATRP of the monomer (OEGMA) from the tethered initiator leads to the in situ synthesis of a POEGMA brush on gold.

Polymer POEGMA brushes have shown to have excellent non-fouling behavior against proteins and cells. Initial studies with ATRP OEGMA polymerization showed that small POEGMA thickness (>10 nm) grown on gold resisted protein adhesion from the sticky protein fibronectin and FBS, with a SPR signal below ~1 ng cm^{-2}. A pattered POEGMA gold surface was also used to demonstrate that cells can be attached to the gold film and that this cellular pattern can be retained for 30 days[30].

2.3 Use of polymer brushes in analytical protein microarrays

Protein microarrays have served as excellent diagnostic tools due to their high throughput, low cost, minimal reagent consumption, multiplexing capabilities, fast

kinetics, and functional integration[4,34]. To test the POEGMA's capabilities for microarray integration, POEGMA slides where printed with capture antibodies and a dose response curve was be generated with IL-6 spiked serum. It was demonstrated that the LOD in the POEMGA slide had better performance (~10-fold improvement) when compared to nitrocellulose[33].

In order to move microarrays towards clinical and point-of-care applications, improvements are needed in reproducibility (intra and inter spot variability), sensitivity, analysis time, automation, and compatibility with portable instruments. Specifically, some of these challenges include: i) low reproducibility due to variability in chip substrate, denaturation and immobilization strategy, probe concentration, blocking steps required, and assay design[35,36]; ii) low sensitivity due to low detection of low protein concentration and low affinity to the biorecognition elements; iii) time for reaction kinetics and assay reading due to washing steps, read out, and data analysis; iv) use of large and bulky instrumentation needed for microarray detection; and v) production cost when designing the assay[4]. Addressing these challenges are extremely necessary to translate microarray systems for POC testing and meet the World Health Organization's ASSURED guidelines[37], where POCT devices should be **A**ffordable (for those at risk of infection), **S**ensitive (minimal false negatives), **S**pecific (minimal false positives), **U**ser friendly (minimal steps to carry out test), **R**apid and **R**obust (short turnaround time and no need for refrigerated storage), **E**quipment-free (no complex equipment), and **D**elivered (to end users). Efforts were then made to address these challenges by optimizing the POEGMA protein microarray towards a self-contained and robust chip, known as the D4

assay. The D4 assay obtains its name from the four simple steps that are needed to run it, where a small volume of liquid containing the biomarker is (i) **d**ispensed on the chip, which (ii) **d**issolves the soluble spots of fluorescently labeled dAb. This is followed by their (iii) **d**iffusion and binding to the analyte-bound cAb spots, which generates a (iv) **d**etection signal of fluorescent spots that are imaged by a table-top fluorescence scanner (**Figure 4**). One of the new additions in the D4 assay is the dissolvable detection antibody that is printed on the surface. To make the detection agents soluble and stable during storage, these are mixed with PEG or trehalose.

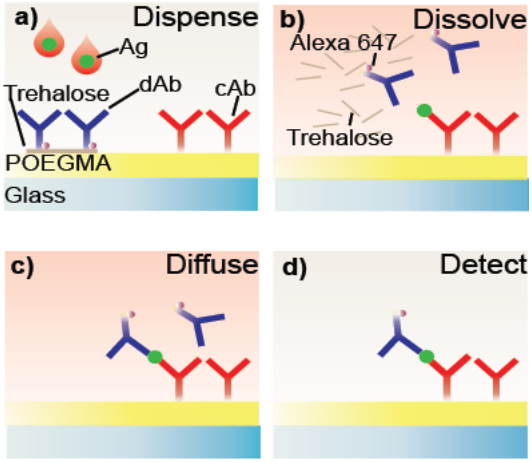

Figure 4: D4 assay steps on POEGMA brushes. a) A drop of blood is dispensed into the chip. b) This causes soluble detection antibodies to dissolve from the surface and diffuse towards the capture spots as seen in c). Finally, this generates a quantifiable fluorescence signal as shown in d)

The D4 assay addresses some of the mentioned challenges in protein microarrays when moving them towards clinical and POC applications. In terms of reproducibility,

the D4 assay presents low intra and inter variability in the assay due to the high level of POEGMA thickness control, which consequently allows for control of antibody immobilization (see Chapter 6) and highly replicable results. Another major concern in microarray technology that can cause irreproducibility is antibody denaturation. The D4 assay tackles this problem as a result of POEGMA's hydrophilic nature, which reduces the chances of proteins' hydrophobic core to contact the surface and therefore fold or denature[38]. It has been shown that the chips can be kept under vacuum and room temperature for several months and still perform the same way as freshly prepared chips[9]. The design of the D4 assay also increases reproducibility from assay to assay due to the simplicity of its workflow. Since chemical activation or blocking steps are not needed and all reagents are self-contained, the assay becomes user friendly and variability due to these steps are eliminated. In terms of sensitivity, the POEGMA's nonfouling nature minimizes nonspecific antibody binding and allows for femtomolar sensitivity. As for time for reaction, the assay can be performed and washed in 90 minutes, scanned in 10 minutes, and analyzed in a few minutes, which is a suitable time rage for POC testing. With regards to cost, fabricating a single chip becomes inexpensive due to the availability of reagents and the miniaturization of the devices, which only requires antibody volumes in the picoliter regime. In addition, the D4 assay does not need to be refrigerated or stored without hydration, making the need for a refrigerator obsolete. As for the use of large and bulky instrumentation, the D4 assay can be tested with portable detectors, however its sensitivity is compromised by about 10-fold[9]. Different strategies can be taken to address this problem, including integration of nanomaterials such as quantum dots, increasing

high density of probes (which can already be achieved with thick polymer brushes), and by enhancing the intensity of the fluorophore. We explore the latter strategy in this dissertation, where a plasmonic structure is used to increase the fluorescence output from the D4 assay.

2.4 Use of plasmonics for biosensing applications

2.4.1 Background

Plasmonics refers to the study of plasmons, or the collective oscillations of conduction electrons in a metal (such as gold, silver, and platinum) which are excitable with specific wavelengths of light. When the electron cloud is displaced relative to its original position due to electromagnetic excitation, a restoring force arises from Coulombic attraction between electrons and nuclei[39]. This force causes the electron cloud to oscillate, and the oscillation frequency is determined by the density of electrons, the effective electron mass, and the size and shape of the charge distribution[40]. **Figure 5** shows this oscillation of electron cloud in a metallic nanoparticle, which according to the Drude model, it oscillates 180 degrees out of phase relative to the driving electric field[41]. The surface charge-density oscillations associated with surface plasmons at the interface between a metal and a dielectric can give rise to strongly enhanced optical near-fields, which are spatially confined near the metal surface. The resulting high field intensity creates an enhanced local density of states, which strongly boosts optical processes such as light absorption and emission at the nanoscale. The next section focuses on the different types of plasmonic modalities that have been used for biosensing, including wavelength shifting and field enhancement.

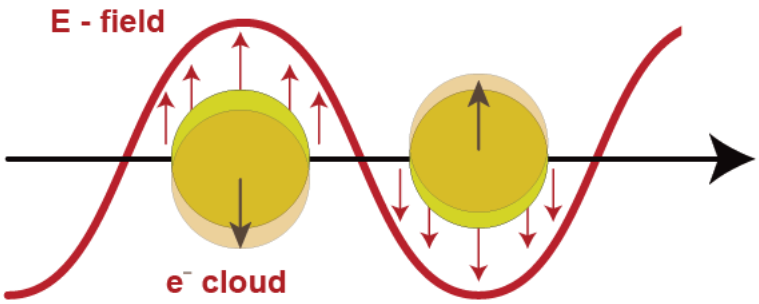

Figure 5: A plasmon refers to the coupled oscillations that rise from the interactions between light and conduction electrons in a metal. This schematic shows plasmon oscillation for a small metal sphere with displacement of the conduction electron charge cloud relative to the nuclei. Adapted from Ref. 40.

2.4.2 SPR and LSPR in plasmonic biosensors

Plasmonic biosensors can roughly be categorized into those that use surface plasmon resonance (SPR) such as metallic films, and those that use localized surface plasmon (LSPR) as in the case of individual nanostructures.[10] SPR has become the most widely used form of biosensing, which relies on a phase or resonance shift when molecules bind to the surface. Here, when a beam of light traveling through a dielectric reaches the surface of a metal, a traveling surface wave is generated at the impinging point of light and it travels along the interface[42]. This wave is referred as the surface plasmon or surface plasmon polariton. When this happens, an evanescent field is generated, which represents how far into the dielectric the surface plasmon wave extends. This surface plasmon acts as an antenna as it can sense the presence of analyte in solutions into the dielectric (up to 1 μm)[43]. **Figure 6a** shows a diagram of the common

Kretschmann configuration, which has become the standard optical configuration in the generation of SPR. It is important to notice that a design consideration for this system it the use of adaptive optics (a prism in this case) so that the momentum of light can be increased and matched to the momentum of plasmons[41]. For its procedure, light is absorbed by the electrons in the middle film of the sensor chip causing them to resonate. This SPR causes a reduction in the intensity of light reflected at a specific angle from the glass side of the sensor surface. As molecules bind to the sensor surface, the refractive index close to the surface changes, altering the angle of minimum reflective intensity[39].

In the case of LSPR (metallic nanoparticles), since the lateral dimension of the interface is much smaller than the plasmon propagation length traveling along the surface, the surface plasmon is localized, which causes an large increase electromagnetic field close to the particle (**Figure 6b**). LSPRs of nanoscale objects can be tuned by varying the size, shape, composition and surrounding environment[44,45]. Some typical examples include single nanoparticle sensors, where change in the color of the scattering nanoparticle (LSPR wavelength), can be used to determine to know if a biomolecule has attached to the surface[46,47]. For instance, a gold nanoparticle can be functionalized with an antibody, giving a particular resonance wavelength. When the antigen binds to the antibody, a change in the index of refraction is created, which can be sensed through a red shift in the resonance wavelength[48]. Other forms of LSPR consist of a high density of plasmon resonant nanostructures immobilized on a substrate, which provides an easier and more robust option to interrogate large number of nanoparticles at a time[49]. Other examples include island-like structures, and structures formed by patterning[10].

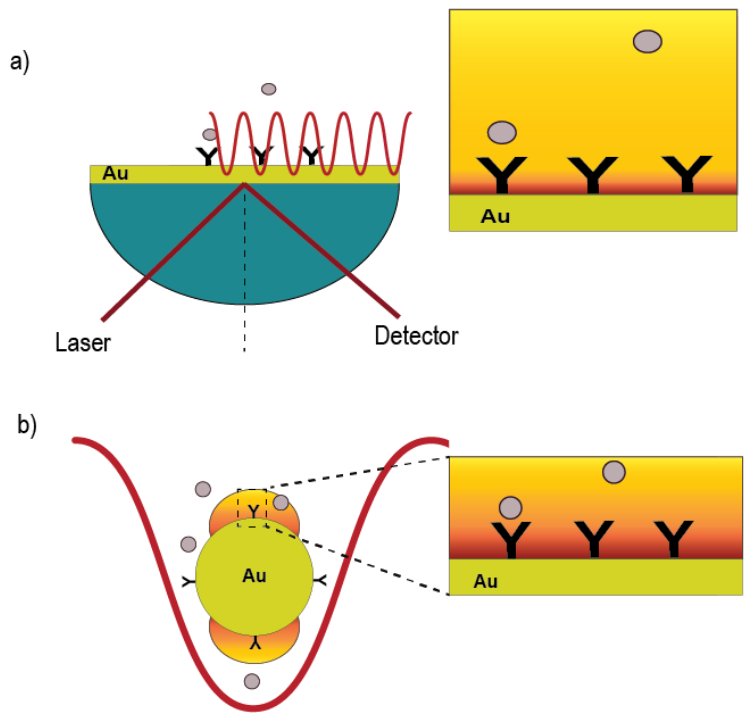

Figure 6: Division in plasmonic biosensors. a) Metallic films that produce a surface polariton and b) individual nanostructures that produce localized surface plasmons (LSP). Adapted from Ref. 43.

LSPR enjoys inherent advantages over SPR in biosensing. One restriction in SPR is that its long field decay length into the dielectric causes a marginal bulk effect. As a consequence, biomolecules that are not attached to the surface become detectable, causing false positive reading[50]. Another disadvantage of SPR sensing is that it needs adaptive optics and thermal controls to function properly[41], making it difficult to incorporate into microfluidics or other point of care devices. On the other hand, LSPR sensing platforms do not have a marginal bulk effect since LSPRs only extend tens of nanometers into the surrounding medium, localizing their sensor information.

Furthermore, these are more amenable to miniaturization since the LSPR signal is created from nanoscale objects which can then be incorporated in small chips for point of care testing [10].

In addition to metallic films that create SPRs and individual nanoparticles that create LSPRs, film-coupled nanoparticles serve as a platform consisting of both. In this case, nanoparticle localized surface plasmons couple to surface plasmons in the metallic film, where charge distributions induced on the nanoparticle in turn induce image charges within the conducting layer. This can be seen as the nanoparticle having a mirror of itself on the film, where the film creates an image dipole of the nanoparticle separated in space[10,51]. And evident advantage of this system is the high reproducibility of film-coupled nanoparticles that can be created over the surface due to the precise molecular spacers that can be fabricated[52–54].An example of this is a plasmonic ruler fabricated with gold nanoparticles over a gold film, which is able to discern distances on the angstrom scale in a highly precise and accurate manner[52]. Another example of a film-coupled system is the nanopatch antenna, where silver nanocubes are coupled to a metallic film. The resonance in the nanopatch, however is fundamentally different from that of coupled spheres, where the region between the flat faces of the nanocube and the metal film induces a gap-plasmon mode which can propagate parallel to the film. Multiple reflections at the nanocube edges cause the gap-plasmon to undergo a Fabry-Perot like resonance with electric field maxima at the edges[55]. A detailed description of this structure is described in Section 2.4.5.

As seen, LSPR and SPR sensing strongly depends on the refractive index of the surrounding medium, providing the basis for colorimetric plasmonic sensors. As mentioned earlier, incident light on a nanostructure and metallic film also interacts with localized or propagating surface plasmons to create large electromagnetic field enhancements. This local electromagnetic field can influence optical processes such as fluorescence, Raman scattering, and infrared absorption, resulting in plasmon-enhanced fluorescence (PEF), surface enhanced Raman scattering (SERS), and surface-enhanced infrared spectroscopy. The following section will focus on plasmon-enhanced fluorescence (PEF) biosensors, since it has become the mostly spread optical sensing method and it is regularly used for assay readout. This section also illustrates current developments in fluorescence signal amplification and provides with current examples of plasmonic biosensors from the literature.

2.4.3 Fluorescence enhancement in plasmonic biosensors

In plasmonic fluorescence enhancement, interaction between the electromagnetic field and surface plasmons is associated with large enhancement of the field intensity and local optical density of states which provides means to increase excitation rate, quantum yield, and control far angular distribution of fluorescence light emitted by fluorophores and quantum dots[56]. Here, the high field created close to metallic structures can interact with fluorophores at their absorption and emission wavelengths, where the fluorophore's radiative and nonradiative decay rates are modified due to an increased local density of states[56]. It is important to note that for short distances from the metal surface Foster energy transfer between a fluorophore and a metal exists, causing strong quenching of

radiative transmissions. However, as the distance increases, the emission via surface plasmons become dominant, which enhances the decay rate and thus the quantum yield. Another important parameter that can increase the collecting efficiency of fluorescence light is the ability to control the emission angular distribution. This is critical since in most fluorescence detection mechanisms less than a few percent of emitted photon is delivered to a detector[56]. Plasmonic structures offer a solution for this since the emitted radiation intensity can be emitted via surface plasmons, offering high directionality.

Numerous examples of plasmonic structures exist for the fluorescently based sensing of biomolecules. These range from chemically synthesized metallic nanoparticles[57–59], flat continuous metallic films[60–63], metallic islands and nanoclusters[64,65], and metallic nanostructure arrays prepared by lithography[13,66–68]. Some outstanding examples include the use of a “bowtie” nanoantenna prepared by electron beam lithography (EBL), where a 30nm gap between the nanostructures offered and enhancement factor of 1300-fold[13]. As a result of such high intensities, authors were able to detect a single fluorescence molecule. Although this kind of enhancement and sensitivity are desired for biosensing applications, fabrication techniques such as EBL can be difficult and expensive to use, hence limiting the biosensor use as a point-of-care test. Furthermore, this technique also requires nanostructures to create a very small and defined gap region that can be difficult to reproduce and fabricate in large scale, liming its use to a single plasmonic detector element.

Plasmonically enhanced microarray assays have become of interest in the biosensing community due to their fabrication simplicity, reproducibility, multiplexing

capabilities, scalability, miniaturization, and ability to be integrated in microfluidics. For instance, Dai *et. al* reported the use of a plasmonic chip with chemically grown gold nano islands on a glass substrate[17]. These chips created up to 100-fold near-infrared fluorescence enhancement, extending the dynamic range of protein detection by three orders of magnitude. A disadvantage of this plasmonic assay is the need for surface functionalization to generate NHS activated substates. This becomes a disadvantage since this extra functionalization requirement brings intra batch variability to the slides, which is undesired when translating the system towards clinical use. Another example of plasmonically enhanced microarray is a "plasmonic patch" that can be placed on top of an immunoassay[18]. In this modality, plasmonic nanoparticles are attached to a PDMS thin film that can be added to any surface containing an immunoassay. In this case, fluorescence enhancement relies on the proximity of the nanoparticles to the fluorophore on the assay. This distance is modified by the growth of a copolymer layer on the nanoparticle surface, where its optimal thickness is about 3 nm. Some of the disadvantages of the flexible patch is that adding an external substrate with embedded nanostructures can be cumbersome and time consuming as it requires careful drying of the assay to obtain optimal proximity of the nanostructures to the fluorophores. In addition, the patch does not offer permanent binding of the plasmonic structures to the assay, which can bring challenges in reproducibility and when performing measurements.

As an alternative, the nanopatch antenna offers a plasmonic platform that can be easily fabricated, does not require surface functionalization, and is highly reproducible.

The following section introduces the nanopatch antenna and Chapter 3 introduces its use as a biosensing system.

2.4.4 The plasmonic nanopatch antenna

A promising plasmonic structure that can be used for fluorescence enhancement in biosensors is the plasmonic nanopatch antenna[55,69–76]. In this structure, emitters are sandwiched between a polymer layer on a gold surface and a cube nanoparticle, creating an enhanced plasmonic environment of nanometer sized cavities that have shown to exponentially increase spontaneous emission rate and radiative quantum efficiency due to the large field enhancement underneath the particles and the increased density of states, process also known as the Purcell Effect[69]. Specifically, this plasmonic structure consists of a 5-15 nm thick dielectric material with embedded fluorescence emitters sandwiched between single crystal silver nanocubes (60 – 100 nm) and a metal film, as illustrated in **Figure 7**. The dielectric gap consists of the layer by layer deposition of the positively charged polyelectrolyte poly(allylamine hydrochloride), or PAH and the negatively charged polyelectrolyte poly(sodium 4-styrenesulfonate) or PSS. As previously mentioned, the fundamental plasmonic mode in the film-coupled nanocube system is a Fabry-Perot resonance resulting from multiple reflections of the waveguide mode beneath the nanocube that propagates within the gap region, with maximum field enhancement occurring near the nanocube edges and corners[55]. This brings a significant advantage to the system compared to other film-coupled platforms because 1) the resonant wavelength can be tuned by varying the nanocube size and the gap size (as opposed to the film-coupled sphere resonance which can only be tuned by changing the gap thickness), and 2)

the nanopatch couples to incident light predominantly through the magnetic field, making the coupling with external detectors significantly more effective[55]. Due to these properties, it has been shown that the field enhancement is the greatest at the plasmon resonance wavelength, which can be tuned by controlling the nanocube size and the dielectric gap thickness and have resulted in a record-high, 30,000-fold fluorescence enhancement and a 1,000-fold emission rate enhancement[55].

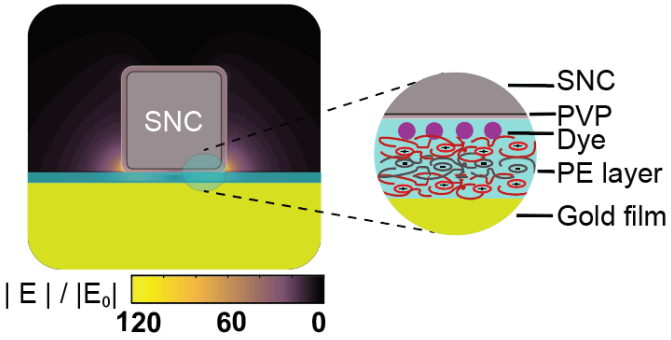

Figure 7: Schematic of the plasmonic nanopatch antenna which consists of a fluorecence molecule sandwiched between a silver nanocube and a metallic film. Color indicates electric field enhancement as obtained from COMSOL simulations.

An important component in the nanopatch antenna system is the dielectric gap thickness, which dictates how far the silver nanocubes are located relative to the gold film. Previous work with Ru-dye as the emitter showed that as the gap thickness increases, two main effects affect the fluorescence enhancement factor: 1) the quantum yield increases due to reduction in quenching, and 2) the excitation rate decreases due to the decreased field enhancement. Combining these two effects, it is seen that the enhancement factor increases as the gap thickness increases and it is the highest at thickness around 10-12 nm before it starts to decrease[69]. Another important aspect of this

plasmonic structure is the single lobe radiation pattern of the antenna at the resonance wavelength, which is normal to the surface. This is an important characteristic of the antenna as it allows for more efficient coupling to external optics. Specifically for the nanopatch, simulation and experimental data showed that the fraction of emitted light collected by an external lens is that of 84%.

The nanopatch antenna can also be implemented over large areas of any shape. This gives rise of a plasmonic metasurface characterized by the homogenous deposition of high density silver nanocubes, which gives rise to a resonant behavior and perfect absorption (up to 99.7%) of light at frequencies that can be modified depending on particle size and gap thickness[77,78]**.** Specifically, it has been demonstrated that light can be absorbed across the visible and infrared range. For this structure, each film-coupled nanocube acts like a magnetic dipole[79], where the resonance of the dipole is determined by the size of the nanocube and the spacer. The collective action of many nanocubes on the surface creates an effective magnetic response. As a result, the impedance of the surface is matched to free space and both reflection and transmission of the surface are eliminated, resulting in complete absorption[54]. The nanopatch metasurface is attractive for biosensing since it offers flexibility in the area and shape of where the fluorescence enhancement can be applied to in a very easy to handle and cost-effective manner without the need of expensive nanofabrication approaches and without changing the original procedures of the exciting sensing techniques.

Chapter 3 The plasmonically enhanced D4 (PED4) assay

3.1 Introduction and sample description

In this work, a protein microarray assay is integrated with a plasmonic metasurface composed of film-coupled nanocube antennas to uniformly enhance the fluorescence from the assay by over 100-fold while maintaining assay performance. As introduced in Chapter 2, the film-coupled nanocube antennas consist of colloidally synthesized silver nanocubes (~100 nm) separated from a metal film by a thin (3-25 nm) dielectric spacer layer[55,69,80] and can be created over large areas to form metasurfaces using simple particle deposition[77,78]. The plasmonically enhanced D4 (PED4) assay is demonstrated in this chapter for the quantification of B-type natriuretic peptide (BNP), which is an important biomarker for the prognosis and long-term monitoring of cardiac disease. The clinically relevant detection limits in BNP for heart failure monitoring are 100-400 pg/mL which in the grey zone and the patient would requires further testing or echocardiogram, and >500 pg/mL which indicates high-risk patients that needs expedited diagnosis and treatment[81–83]. Chapter 5 will demonstrate the feasibility of adding multiplexing capabilities to this system for the simultaneous analysis of three other clinical biomarkers for the diagnosis and prognosis of heart failure.

To enable optimized and uniform fluorescence enhancement, the D4 assay is integrated in the gap region between the silver nanocubes and the metal film, where large electromagnetic field enhancements are created (**Figure 8a**). **Figure 8b** shows the

fabrication steps of the PED4 assay, where a gold film is first deposited on glass, followed by growth of a POEGMA brush by SI-ATRP[30–32], as described in Chapter 2. Two types of microspots are then inkjet-printed on the polymer brush: "stable" spots of capture antibodies (cAb) surrounded by "soluble" spots of fluorescently labeled detection antibodies (dAb- Alexa 647) mixed with an excipient (typically trehalose) that helps dissolve the dAbs upon contact with biological fluid, such as serum, plasma or blood. For this specific assay, capture Abs (monoclonal anti-BNP IgG) were obtained from HyTest and dAbs (polyclonal anti-BNP IgG) were obtained from R&D Systems. The dAbs were directly conjugated to fluorophores by following the antibody suppliers' instructions (Invitrogen, Alexa Fluor 647 Antibody Labeling Kit). The cAbs were spotted onto POEGMA-coated substrates using a Scenion S11 noncontact printer under ambient conditions at 1 mg/mL concentration. Spots of soluble detection reagents were composed of dAbs (1 mg/mL) mixed with excipient (0.25 mg/mL trehalose) and printed in a similar fashion. In the D4 assay (**Figure 8c**), a small volume (~80 µL) of liquid, containing the clinically relevant cardiac biomarker BNP is (i) dispensed on the chip, which (ii) dissolves the soluble spots of fluorescently labeled dAb. This is followed by their (iii) diffusion and binding to the analyte-bound cAb spots, which generates a (iv) detection signal of fluorescent spots that are imaged by a table-top fluorescence scanner.

Finally for the PED4 assay, silver nanocubes are adhered to the surface through a poly(allylamine hydrochloride) (PAH) interfacial layer or by incubating silver nanocubes conjugated to a secondary Ab (S.A), methods that will be discussed in Chapter 4. To generate dose–response curves, D4 chips were incubated in a dilution series of analyte-

spiked calf serum (Clontech) for 90 min. Substrates were then briefly rinsed in 0.1% Tween-20/PBS, and then dried. Arrays were imaged on an Axon Genepix 4400 tabletop scanner (Molecular Devices, LLC). Data from three different samples were averaged and data was fit to a five-parameter logistic (5-PL) fit curve using OriginPro 9.0 (OriginLab Corp.). The limit-of blank (LOB) was estimated from the mean fluorescence intensity (μ) and standard deviation (σ) from three blank samples, defined as LOB = μ_{blank} + $1.645\sigma_{blank}$. LOD was estimated from spiked low concentration samples (LCS) above the LOB, such that LOD = LOB + $1.645\sigma_{LCS}$.

Figure 8d shows representative fluorescence images of the capture spots (i) before and (ii) after adding the silver nanocubes to the gold surface for a 10 nm POEGMA brush. A 216-fold fluorescence enhancement is obtained from comparison of the “pre cubes” and “post cubes” on gold at a BNP concentration of 1.9 ng/mL, as can be seen by the increase in intensity of the capture spots. A 151-fold enhancement is observed when compared to a glass control at the same analyte concentration (**Figure 9**)

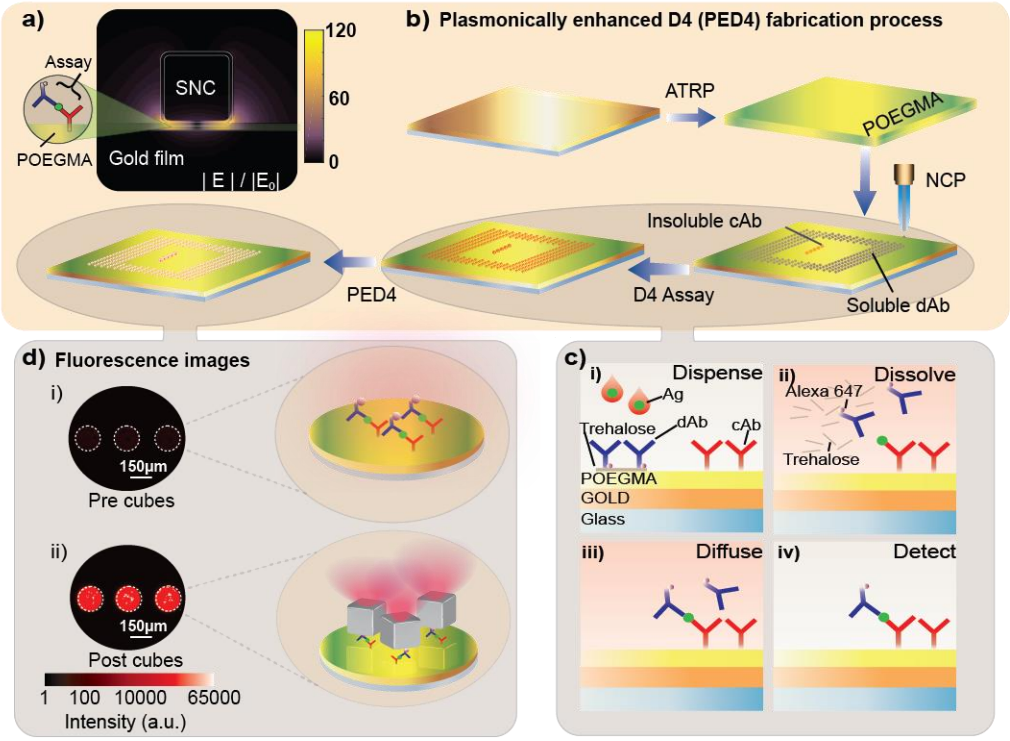

Figure 8: Design and fabrication of the plasmonically enhanced D4 (PED4) assay. a) Schematic of plasmonic nanoantenna with the assay integrated between the gold film and silver nanocube (SNC). Color indicates electric field enhancement as obtained from COMSOL simulations. b) PED4 fabrication starts by evaporating gold on a glass slide, followed by poly(oligo(ethylene glycol) methacrylate (POEGMA) growth by surface initiated atom transfer radical polymerization (SI-ATRP). "Stable" capture antibodies (cAb) and "soluble" detection reagents are spotted onto the surface by noncontact inkjet printing (NCP). c) The D4 assay is performed. d) Finally, silver nanocubes are attached to the surface resulting in 216-fold fluorescence enhancement of the capture spots for a 1.9 ng/mL B-type natriuretic peptide (BNP) concentration and a 151-fold increase when compared to a glass control at the same concentration.

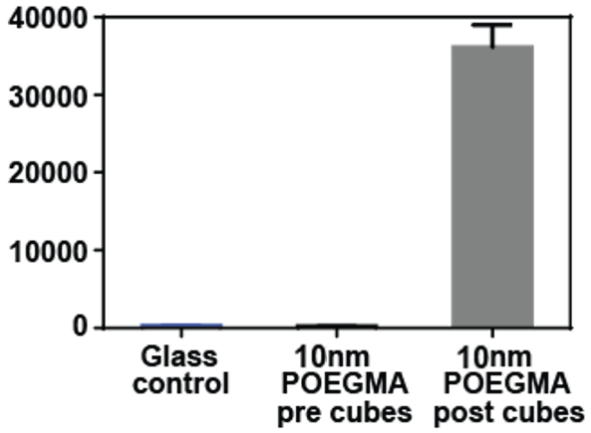

Figure 9: Fluorescence measurements for the three different assays in this study. Glass control, a gold slide with a 10 nm POEGMA brush and no SNCs, and a gold slide with a 10 nm POEGMA brush with SNCs deposited on the surface with a PAH layer.

3.2 Enhancement through particle deposition using an interfacial layer

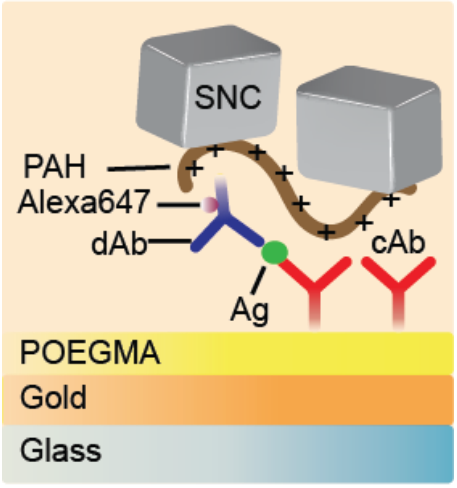

Figure 10: Schematic of PED4 assay obtained by depositing silver nanocubes (SNCs) using an interfacial poly(allylamine hydrochloride) (PAH) layer.

To investigate the fluorescence enhancement of the assay provided by the plasmonic metasurface, first PAH was used to electrostatically adhere the silver nanocubes on the surface (**Figure 10**). For this end, D4 chips printed on a gold film were submerged in a suspension of 3 mM Poly(allylamine hydrochloride) (PAH) and 1 M NaCl for 5 mins after completion of a D4 assay followed by rinsing and drying. A silver nanocube solution (1 mg/mL) was pipetted on top of a large coverslip spacer and placed on top of the D4 chips to ensure uniform thickness of the solution over the whole sample and the D4 assay slides were placed face down on top of the coverslip. The slides were kept in a refrigerator for 60 min to reduce evaporation, after which they were rinsed with DI water and dried with N_2. The plasmonic metasurface characterized by the homogenous deposition of the silver nanocubes on the capture spots is seen in the photograph in **Figure 11a,** the dark field image in **Figure 11b** and the scanning electron microscopy (SEM) image in **Figure 11c and 11d**. From these figures, is interesting to notice that the silver nanocubes only deposit in the location of the antibody capture spots, offering a reduction of noise around the surface background. It is also worth highlighting the that the uniformity and density of the nanocubes on the surface is like those of the metasurfaces introduced in chapter 2, which gives rise to an absorber at the plasmon resonance of the structure.

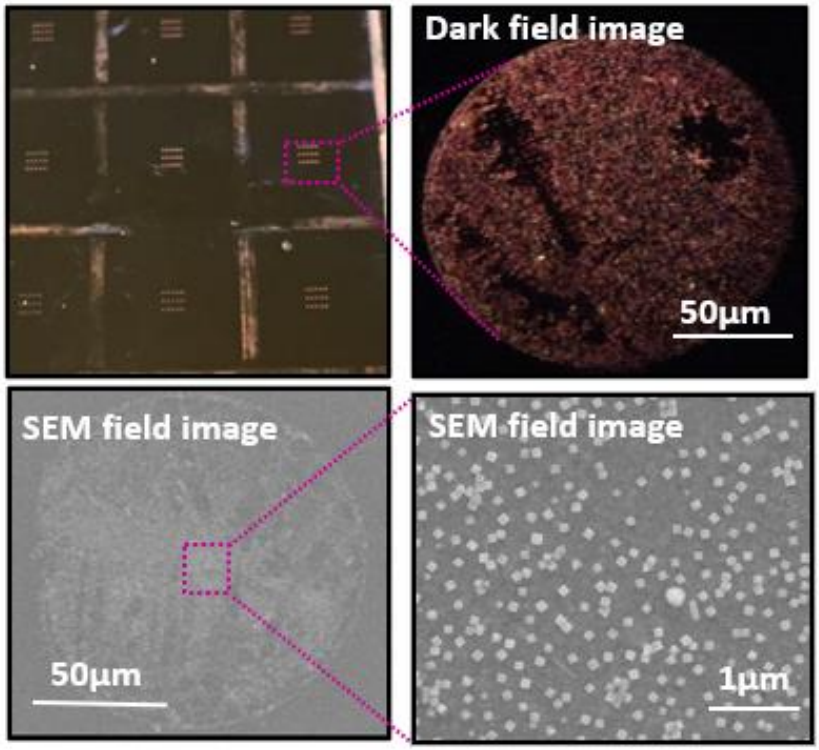

Figure 11: a) Photograph of capture spots show silver nanocubes attach specifically to printed spots. b) Dark-field and c-d) SEM images show uniformity of the nanostructures constituting a large area metasurface.

As it was introduced in chapter 2, a perfect absorber metasurface can be used to absorb light at certain frequency of light depending on the thickness or particle size in the nanopatch antenna. This was also investigated with the PED4 where the thickness of the POEGMA was grown to 5 nm, 10 nm, 15 nm, and 20 nm while maintaining the particle size constant. Nanocubes of 100 nm in sized where then placed on the surface to determine the resonant behavior of the structure. To obtain the resonant behavior, white light reflectance measurements at near normal incidence were performed using a custom-built confocal microscope with a 20× objective and detected by a spectrometer with an

attached charge coupled device (CCD). As seen from the reflectivity measurements in **Figure 12**, as the thickness of the polymer is increased, there is a blue shift in the resonance of the metasurface, as was seen earlier in chapter 2.

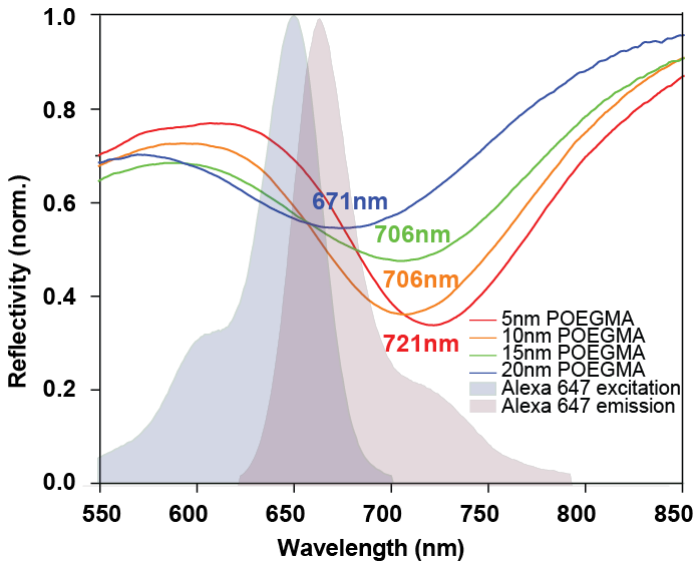

Figure 12: Plasmon resonance in PED4 for different POEGMA thickness. Resonance blue shifted 50 nm from 721 nm to 671 nm when increasing the POEGMA thickness from 5 nm to 20 nm.

3.3 POEGMA thickness dependence on fluorescence enhancement

Next, we systematically probed the role of the POEGMA thickness on the dose-response curves for BNP, as this thickness varies the critical distance between the silver nanocubes and the gold film of the metasurface. Because POEGMA is grown *in situ* from the gold or glass surface by SI-ATRP, the ATRP provides highly controlled growth kinetics of the polymer for thicknesses between 5 and 50 nm as seen in Chapter 2 (see **Figure 3**). Before performing detailed measurements of dose-response curves, the effect

of the gain setting on the photomultiplier (PMT) detector was characterized for an assay on a 70 nm POEGMA brush on glass as well as when embedded in the plasmonic metasurface to determine its effects on the enhancement and LOD, as it will be discussed in detail in the next section. A gain of 400 was chosen for the following experiments, as it provided the highest fluorescence enhancement without saturation of the detector and a low LOD. Before adding the silver nanocubes, slides were measured to determine their response on the gold film as seen in the purple curves in **Figure 17a** for POEGMA thicknesses of 5, 10, 15 and 20 nm. The fluorescence intensity for the 5 nm and 10 nm POEGMA brushes on gold was similar to the D4 assay on glass, while it was slightly higher for the 15 nm and 20 nm brushes. This is likely due to a small plasmonic fluorescence enhancement from the gold film alone of approximately 2-fold (for a 20 nm brush and a gain of 400) which is less pronounced at very close proximity to the surface due to fluorescence quenching effects. Embedding the assay in the plasmonic metasurface resulted in two orders of magnitude fluorescence enhancement (red curves) when compared to both the glass control (black curves) and the samples before silver nanocube deposition. It is also important to note that adding the silver nanocubes to the D4 assay on glass did not appreciably alter the fluorescence intensity (**Figure 13b**), demonstrating that the fluorescence enhancement is caused by the formation of the film-coupled nanocube antennas constituting the plasmonic metasurface, and not from the simple addition of silver nanoparticles.

The fluorescence enhancements from the dose-response curves were calculated by two separate methods: 1) a linear enhancement extracted from the linear component of

the sigmoidal curve, and 2) a maximum enhancement extracted from the BNP concentration providing the largest enhancement, both compared to a control consisting of 70 nm POEGMA on glass **(Figure 13c)**. The linear enhancement (LR Enh) was obtained by averaging the enhancement across all concentrations in the linear regime (fitted using linear fit with R-squared value > 95%) from the control calibration curve, and error bars represent the standard error of the three replicates.

From this, we note larger enhancements for assays with thinner (5 -10 nm) POEGMA brushes, with linear and maximum enhancement levels of 74-fold and 105-fold, respectively. These values are reduced for assays with thicker (20 nm) POEGMA brushes, with linear and maximum enhancement levels of 40-fold and 53-fold, respectively. Larger enhancements for smaller POEGMA thicknesses can be attributed to film-coupled nanocube antennas with smaller mode volumes and, in turn, larger local electromagnetic fields. Although the fluorescence enhancement is greater for smaller POEGMA thicknesses, the intensity variation between slides is larger as seen by the error bars in the dose-response curves, which likely can be attributed to diminished immobilization of the cAb on thinner POEGMA brushes.

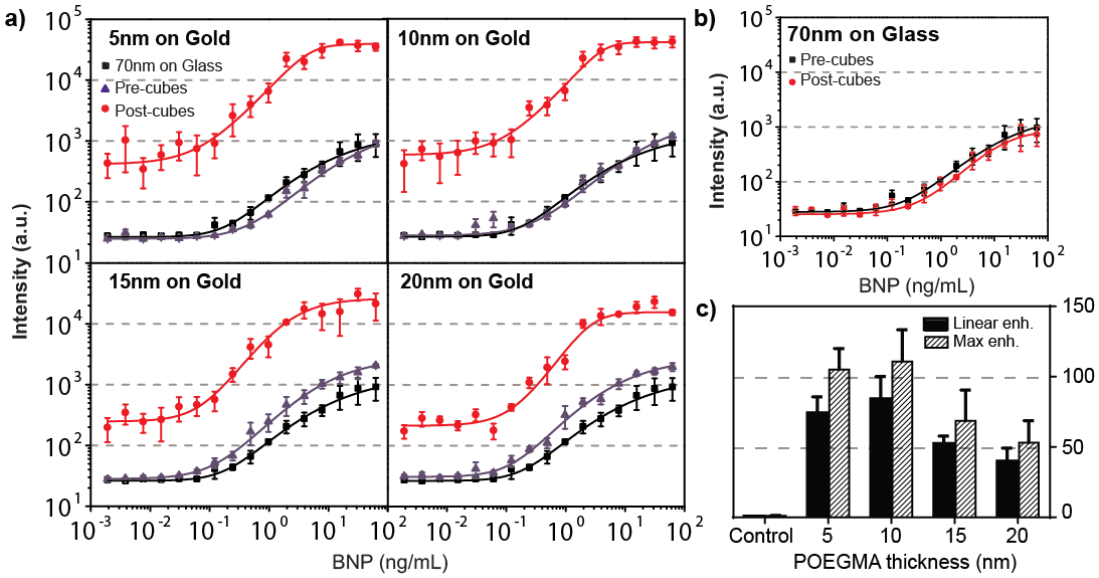

Figure 13: Dependence on brush thickness. a) Evaluation of the plasmonically enhanced assay for 5, 10, 15, and 20 nm POEGMA brushes for a PMT gain of 400. Experimental data is shown for the assay before (purple) and after (red) nanocube deposition as well as for a control on glass with a 70 nm POEGMA brush (black). Solid lines show fits to the data. b) Additional control experiment where the fluorescence intensity of a 70 nm POEGMA brush on glass is observed to not be enhanced by the addition of silver nanocubes. c) Linear and maximum enhancement summary for plasmonic metasurfaces with different POEGMA thicknesses along with the glass control. Error bars in all panels are based on three independent replicates of each experiment. Enhancement was deemed statistically significant when compared to control but not among each other. Bars with the same letter are statistically significant.

3.4 Gain dependence on fluorescence enhancement and limit of detection

The effect of the gain setting on the photomultiplier (PMT) detector was also characterized for an assay on a 70 nm POEGMA brush on glass as well as when embedded in the plasmonic metasurface, as seen below, where error bars in the dose-

response curves represent the standard error from three replicates that were performed on different days.

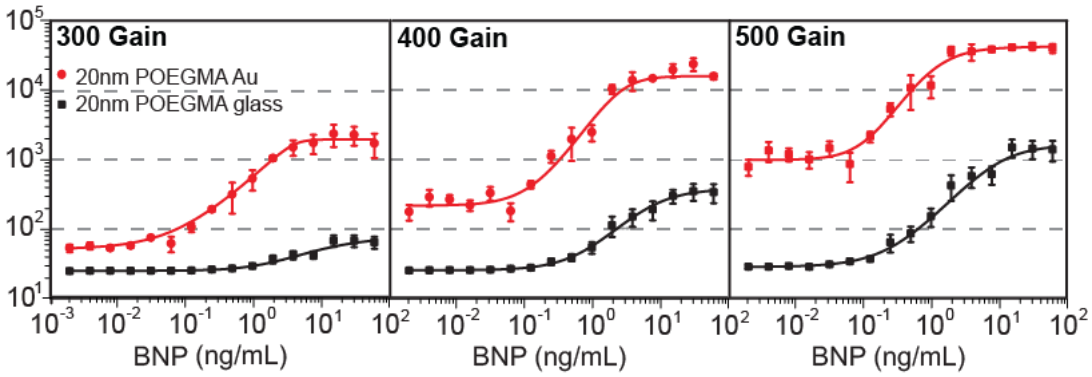

Figure 14: Dose-response curve for different PMT gains for 20 nm POEGMA on glass and on gold embedded in the plasmonic metasurface (PED4).

As seen in **Figure 14**, for the lowest PMT gain of 300, the limit of detection (LOD) decreases by approximately 14-fold from 0.56 to 0.04 ng/mL when compared to the glass control and is accompanied by a 27-fold maximum fluorescence enhancement provided by the plasmonic metasurface. Reducing the photomultiplier gain allows us to demonstrate how the PED4 can be used to compensate for the loss of sensitivity during detection, as we were able to obtain a low LOD of 0.04 ng/mL at 300 gain with the PED4, which even surpasses the LOD of 0.07 ng/mL from the control at higher sensitivities of 500 gain. This serves as a demonstration on how the PED4 can potentially be used with less sensitive and inexpensive detectors that can be used in limited resource settings and it is critical for POCT applications. Larger fluorescence enhancements are

observed for gains of 400, which show a linear enhancement of 40-fold and maximum enhancement of 53-fold. Large enhancements were also observed for 500 gain, but they were lower than 400 gain due to saturation of the PED4 sigmoidal curves at the line. In these cases, the change in LODs is not significant from 0.26 to 0.16 ng/mL for a gain of 400 and from 0.07 to 0.15 for a gain of 500. Albeit clinically irrelevant, this small increase in the LOD for higher gains, which is greater than for the glass control, is likely arising due to noise associated with non-specific binding of the silver nanocubes to the assay. After the addition of the silver nanocubes, an increase in the average noise is observed which is likely caused by scattering from the cubes that is collected more effectively at higher gains. **Figure 15** presents a summary of enhancements obtained with all thicknesses and gains used in experiments, and **Table 1** presents this data in a summarized form. **Figure 16** presents 3D plots for better visualization for both linear (**Figure 16b**) and maximum (**Figure 16c**) enhancement.

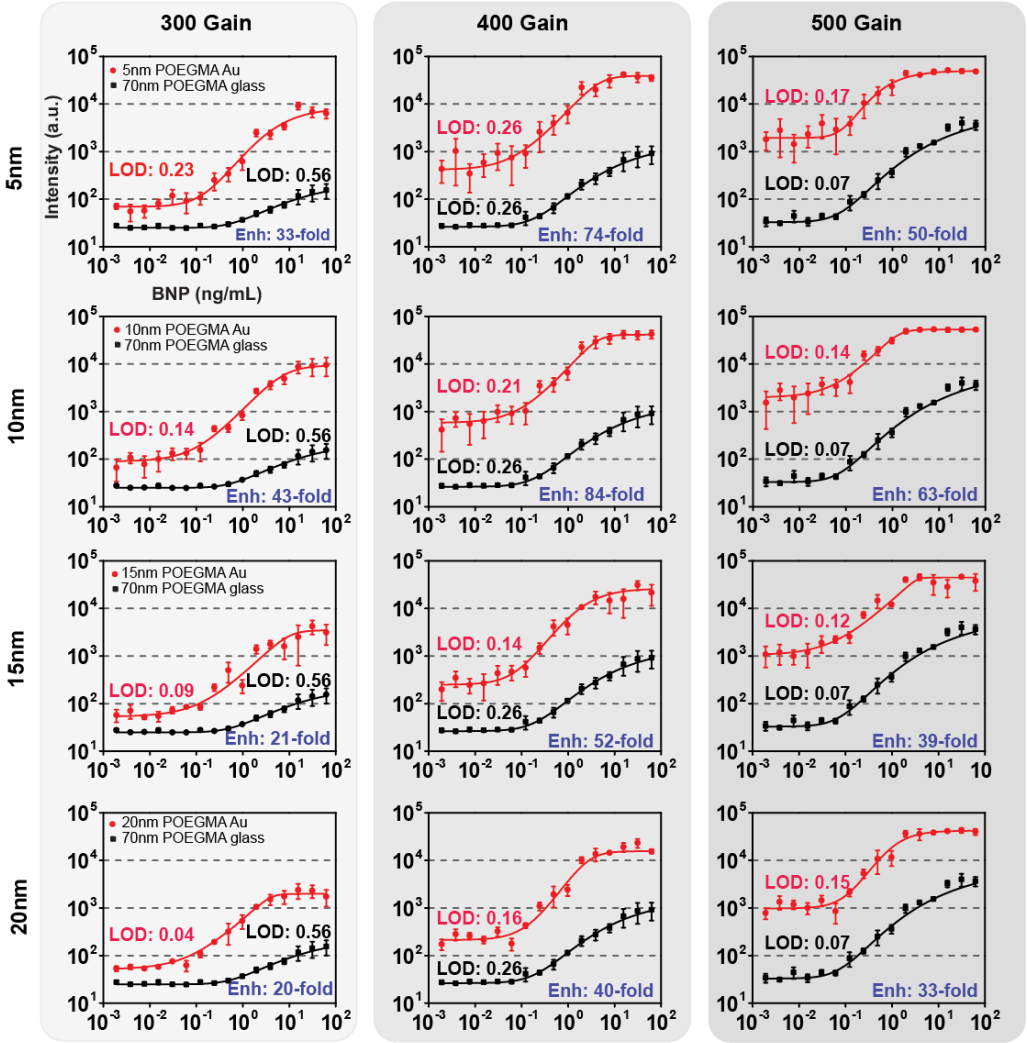

Figure 15: Fluorescence intensity for photomultiplier gains of 300, 400, and 500 and assay performance for polymer thickness of 5, 10, 15, and 20 nm POEGMA. LODs were calculated for the PED4 and glass control.

Table 1 Summary of linear and maximum fluorescence enhancement for unconjugated case

Fluorescence Enhancement						
	300 gain		400 gain		500 gain	
	LR Enh	Max Enh	LR Enh	Max Enh	LR Enh	Max Enh
5 nm Post-cubes Au	33 ± 1	88 ± 14	74 ± 11	105 ± 15	50 ± 13	77 ± 39
10 nm Post-cubes Au	43 ± 5	78 ± 4	84 ± 16	110 ± 23	63 ± 16	132 ± 42
15 nm Post-cubes Au	21 ± 5	42 ± 23	52 ± 5	69 ± 22	39 ± 8	62 ± 14
20 nm Post-cubes Au	20 ± 6	27 ± 7	40 ± 9	53 ± 9	33 ± 6	39 ± 19

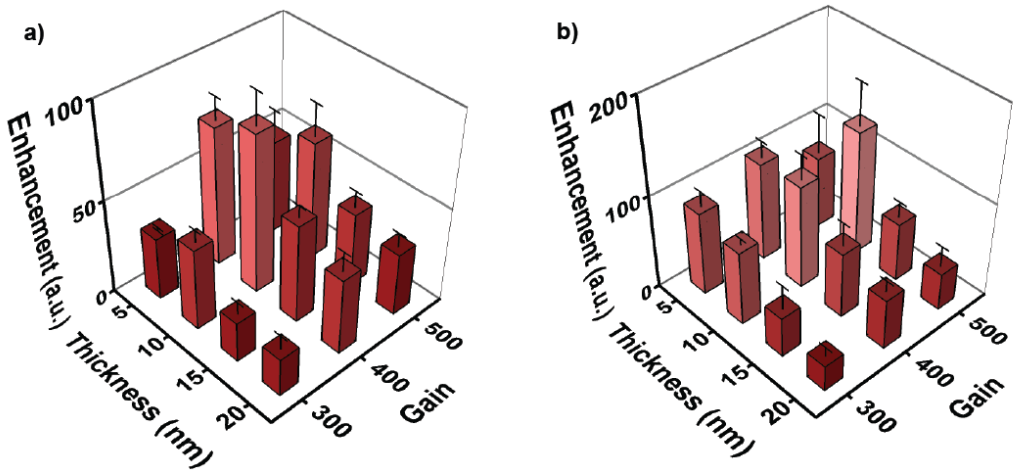

Figure 16: Summary of the results in Figure 19 of the effect of photomultiplier gain and POEGMA thickness on fluorescence enhancement. These are plotted as 3D bar graphs in a) and b), respectively.

The LOD was also characterized for all cases, summarized in the **Table2** and 3D plot in **Figure 17**. In the case of the glass control, it is seen that as the gain increases the LOD decreases due to the increase in sensitivity in the detector. However, this is not the case for the PED4, where increasing the gain from 300 to 400 leads to an increase in LOD due to the increase in the intrinsic fluorescence variability as discussed earlier. The

decrease in LOD from 400 to 500 gain is due to the saturation of the detector, which leads to an inaccurate fit of the dose response curves at this gain. When focusing on 300 and 400 gains where saturation is avoided, it is seen that as the POEGMA thickness increases, the LOD decreases because of the smaller variability at this polymer thickness. Most importantly, comparing the LOD of the thicker (20 nm) POEGMA brush in the PED4 to that of the glass control reveals a 14-fold improvement in the LOD for the 300 gain case and it maintains a similar LOD for 400 gain.

Table 2: Summary of LODs for unconjugated case

Limit of Detection			
	300 gain	400 gain	500 gain
	LOD [ng/mL]	LOD [ng/mL]	LOD [ng/mL]
70 nm POEGMA glass	0.56	0.26	0.07
5 nm Post-cubes Au	0.23	0.26	0.17
10 nm Post-cubes Au	0.14	0.21	0.14
15 nm Post-cubes Au	0.09	0.14	0.12
20 nm Post-cubes Au	0.04	0.16	0.15

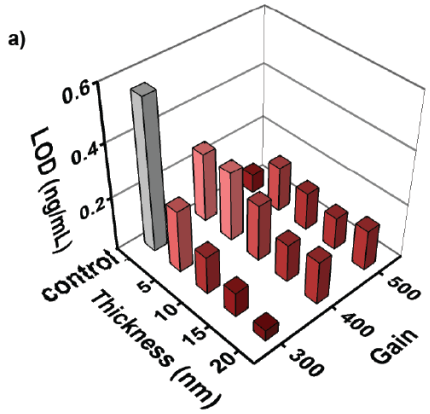

Figure 17: Summary of the results in Figure 8 on the effect of photomultiplier gain and POEGMA thickness on limit of detection (LOD) for deposition of silver nanocubes by PAH layer, plotted as 3D bat graph in a).

By increasing the photomultiplier gain it is seen that there is an increase in the background noise when silver nanocubes are added to gold. To test the origin of this, a PED4 assay with 20 nm thick polymer was run using the PAH silver nanocube deposition, except that fluorophores were not conjugated to the detection antibody. Data was taken on gold before and after placing the particles as seen in **Figure 18**. By adding the silver nanocubes (1mg/mL), there is an increase in the average noise that is inherit from the scattering generated by the cubes and is collected more effectively at higher gains. Error bars represent standard deviation of 5 repeats in a single assay. Silver nanocubes were also added directly to the surface at the concentration of 1mg/mL on glass (**Figure 18d**) and gold (**Figure 18e**) with a single PAH adhesion layer in between, and it was observed that in glass the silver nanocubes do not contribute to the noise significantly even at high gains. Adding nanocubes to the gold surface, however, generated a higher contribution of noise as seen in **Figure 18a-c** that is dependent on the gain. Error bars in this case represent the standard deviation of 10 repeats on a slide.

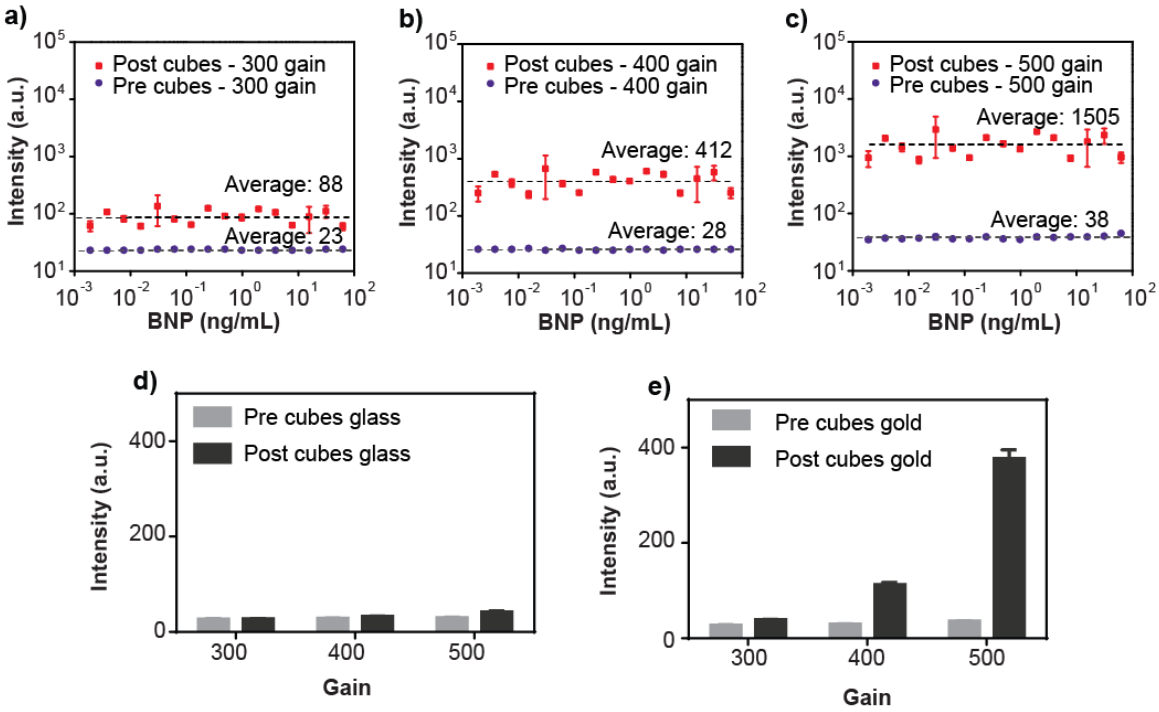

Figure 18. Testing the origin of background noise as function of gain. a-c) 20 nm POEGMA on Au where PED4 assay was performed without the conjugation of Alexa-647 to the detection antibody at three different gains. Purple dots represent the "pre cubes" case and red squares represent the "post cubes" case. Black dotted lines represent the average intensity across all concentrations. Silver nanocubes were also directly deposited on glass d) and gold e) surface through a single PAH layer for three different gains.

3.5 Conclusion

In conclusion, we have integrated plasmonic metasurfaces and immunoassays using a bottom-up, scalable fabrication approach with the targeted deposition of colloidally synthesized silver nanocubes for the detection of the clinically relevant cardiac biomarker BNP. The assay performance was extensively explored as a function of the POEGMA brush thickness as this controls the nanoscale gap between silver nanocubes and the underlying gold film, and in turn, the electromagnetic field

enhancement provided by the metasurface. Fluorescence enhancements of more than 100-fold were observed for the smallest gaps with a 5 or 10 nm POEGMA brush corresponding to the metasurface with the largest electromagnetic field enhancement. Large fluorescence enhancements were observed with brushes of up to 20 nm, which also provided the least variability between assays. Enhancement as a function of the gain was also investigated, where it was observed that as the gain was lowered, the scattering from nanoparticles was also reduced, providing a large difference in LOD between the glass control and PED4. This also tells us that the loss in sensitivity in the glass control due to lower gain can be compensated by PED4, and serve as a proof of concept that the PED4 can be used to compensate for the loss of sensitivity in less expensive detectors, a concept that will be explored in the next chapter. This work demonstrates the promise of utilizing plasmonic metasurfaces for biosensing and could be extended to other biomarkers and fluorescence-based microarrays to enable a new generation of ultra-bright, point-of-care immunoassays and could even be adapted to broader applications where fluorescence enhancement is needed, such as DNA-microarrays.

Chapter 4 The PED4 as a Point of Care Test (POCT)

4.1 Introduction

There is a high demand for low cost, rapid, and sensitive detection methods since the ability to diagnose diseases rapidly is a significant cause of the disparity of deaths resulting from both communicable and non-communicable diseases. Existing diagnostic instrumentation usually requires sophisticated infrastructure, expensive reagents, long assay times, and highly trained personnel. An ideal diagnostic test for a limited-resource setting should be user friendly allowing medical personnel to diagnose disease and start immediate treatment, be robust (no requirement for refrigerated storage), avoid requirements for complex pre-processing of biological samples, be portable, inexpensive, highly sensitive, and have the required specificity[37]. Several creative methods for improving the sensitivity and detection limits of diagnostic tools have been devised, however these methods require extra steps, complex assay preparation, non-traditional data processing, and specialized signal quantification apparatus such as micro-Raman scattering instrumentation[4].

Point-of-care assays have become of great interest in the health sector due to their simple use and rapid availability of results. This is specifically necessary in locations where resources are scarce and cannot afford specialized laboratory equipment. POCTs are also beneficial since they only need small sample volumes and do not require the separation of proteins from blood. As described earlier, the D4 assay can be considered

for point-of-care testing since it can potentially be used with whole blood due to the non-fouling behavior of the polymer surface, and therefore does not require any blood pre-processing. Furthermore, price for this immunoassay test is highly reduced since all reagents are self-contained and it only requires picoliter volumes of capture and detection antibodies. As a result, it does not require any extra mixing or washing steps to perform the assay, reducing the need of specialized personal, which is required for the gold standard ELISA. The addition of the plasmonic components in the D4 assay results in a significant reduction in the cost of the detection mechanism required for protein quantification. For instance, table-top fluorescence microarrays cost about ~$150,000, price that are prohibited in low resource settings or developing countries. In addition, these are bulky and heavy, making them cumbersome to carry to testing facilities in remote areas. To further move the D4 assay as a point-of-care test, its detection mechanism needs to be simplified to be small, easy to carry, and sensitive. In order to achieve this, efforts have been made to reduce the size and complexity of the imaging system to mobile devices, such as cell-phones[84,85]. These devices are inexpensive as they use simple components such as a compact laser diode and the same camera from the cellphone device.

By discarding the need of an expensive fluorescence microarray, the cost for sensitive detection with the PED4 is very small. By using a portable system, the instrumentation requirement could be dropped from $150,000 to less than $1,000. In addition, due to the simple fabrication of the PED4, the chips can be made at a cost on the order of several cents per chip.

As seen in chapter 3, the PED4 can easily be fabricated with the use of an interfacial polyelectrolyte layer to attach the SNCs on the antibody surface. However, to move the system towards a POCT the step of adding extra reagents for particle deposition needs to be simplified or removed. As it will be discussed in the next section, this can be done by directly attaching the SNCs to the assay through physical bonding between a secondary antibody in the nanocube and the detection antibody. As a result, fluorescence enhancement can be achieved with the simple addition of the SNC solution on the assay. This reduces the number of steps needed to run the PED4 assay, making it more user friendly and reproducible. Section 6.2 in the "Future Directions" chapter discusses further plans to reduce the number of steps when performing the PED4 assay by fabricating a silver nanocube conjugate that has the detection antibody directly attached to the SNC along with the fluorophore reporter. This will allow us to further move the system to a single step process where the user only needs to add the fluid to be tested. In addition, this will decrease the thickness of the overall assay and hence produce higher enhancement values. Furthermore, the use of microfluidics is investigated in Section 4.5 to make the PED4 a faster POCT. This will allow the user to place the antigen solution, the SNC solution, and the wash buffer in different chambers and let the assay run without the need of user interface.

4.2 Reducing number of assay steps with conjugated nanoparticles

In order to move the PED4 to a point of care format so that it can be performed in a simple, and fast manner, the structure of the PED4 was modified to avoid the need of an

interfacial layer. To do this, an alternate deposition method was investigated that will also allow to decrease the noise arising from non-specific binding of silver nanocubes. For this, the PED4 chips were instead incubated with 100 nm silver nanocubes conjugated to a secondary Ab that specifically targets the Fc region of the dAb-Alexa 647 conjugate, as seen in the schematic in **Figure 19**.

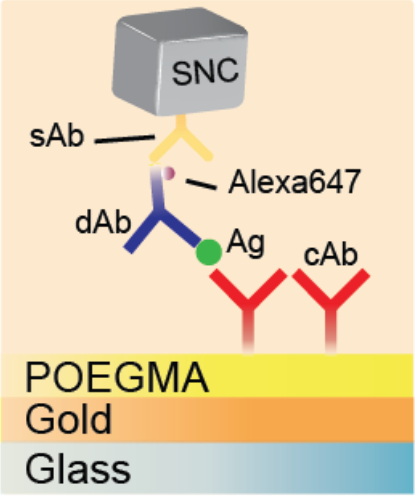

Figure 19: Reduced-step assay with Ab-nanocube functionalization. a) Schematic of the assay where the silver nanocubes are conjugated with a secondary antibody that targets the Fc region in the dAb.

A BNP assay in FBS with analyte-spiked serum was performed using this approach on 5, 10, 15, and 20 nm POEGMA coated gold slides as well as a glass control and measured before and after silver nanocubes were added. **Figure 20a** shows the data for a 20nm POEGMA slide. For this case, is observed that the PED4 assay fabricated with the conjugated silver nanocubes (red curve) has a significantly lower noise than the assay fabricated with the interfacial PAH layer, in particular at the low BNP-

concentration tail of the dose-response curve (see Chapter 3). This results in a reduced LOD from 0.16 ng/mL for the glass control to 0.02 ng/mL for the conjugated nanocubes for a 20 nm POEGMA brush embedded in the plasmonic metasurfaces. This represents the lowest LOD obtained in the study, which was even measured for a high gain of 500. This improved LOD is observed while maintaining fluorescence enhancements of over 10-fold in the clinically relevant linear regime of the assay (0.1 – 0.5 ng/mL)[86] and maximum enhancements of ~19-fold **(Figure 20b)**. A summary comparing results for the conjugated and nonconjugated cases is presented in **Table 3**. In contrast to many traditional assays, here the signal-to-noise ratio can be improved as the non-specific binding is reduced by the simultaneous use of two techniques. The first is the integration of the non-fouling polymer brush POEGMA to avoid non-specific binding of proteins on the surface [31,33,87], and the second is the conjugation of the nanocubes to increase their specificity to the assay and reduce the noise at low BNP values. Furthermore, the use of the non-fouling POEGMA reduces the likehood of the secondary antibodies in the conjugated nanocubes to attach nonspecifically to the surface.

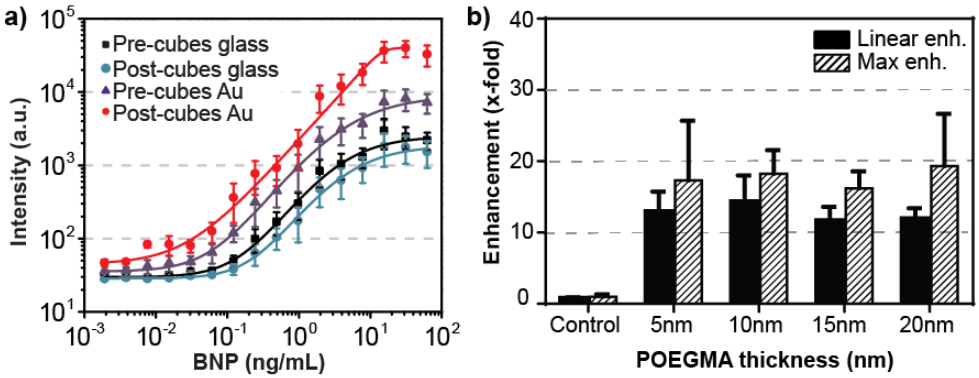

Figure 20: Fluorescence enhancement with conjugated nanocubes. a) Dose-response curve for 20 nm POEGMA before (purple) and after (red) adding silver nanocubes to the assay on gold as well as control on glass before (black) and after (blue) adding nanocubes. A 19-fold fluorescence enhancement is observed and approximately 8-fold improvement in the LOD after adding the silver nanocubes to the assay on gold. b) Linear and maximum enhancement summary for plasmonic metasurfaces with different POEGMA thicknesses along with the glass control. Error bars in all panels are based on three independent replicates of each experiment.

As in the case of PAH deposition method visited in Chapter 3, the dose-response curve was also investigated for 5, 10, 15, and 20nm POEGMA (**Figure 24**), with enhancement summarized in **Table 3.** As previously observed, the enhancement was largest for thinner POEGMA slides, giving up to 13-fold enhancement in the linear regime and up to 18-fold maximum enhancement. Furthermore, similarly to the 20nm POEGMA case, assay performance was better for the upper POEGMA thicknesses.

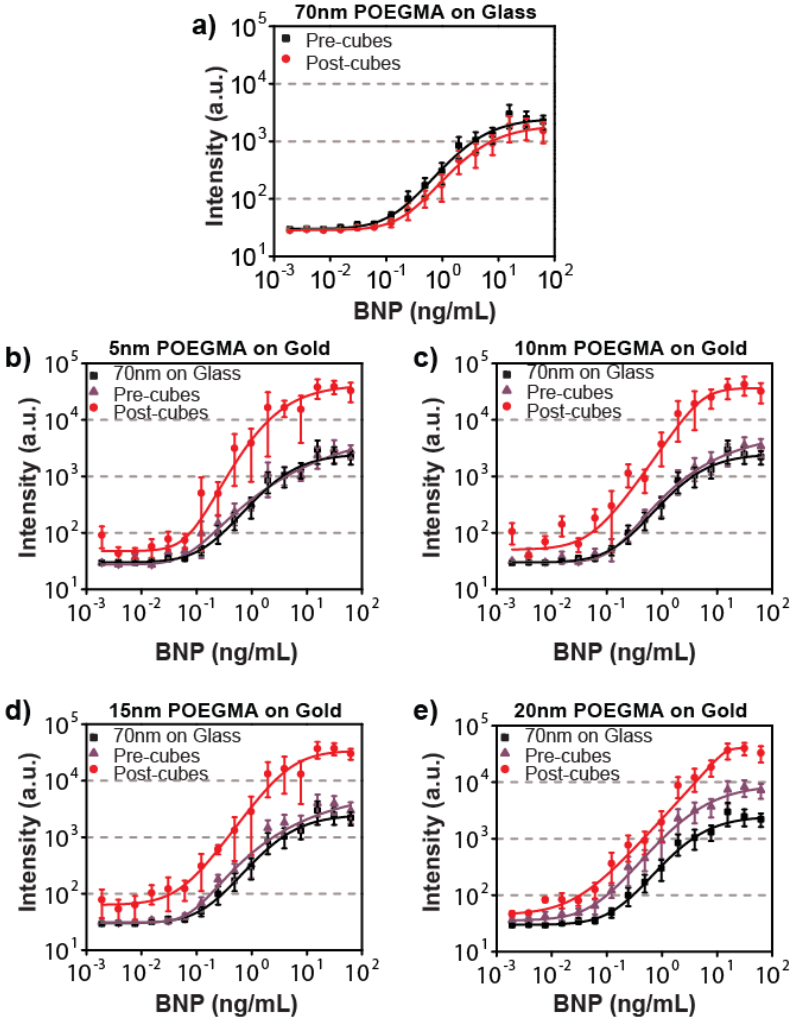

Figure 21: shows additional data for different thicknesses of the POEGMA brush using the conjugated silver nanocubes. Data was obtained from three replicates and the error bars represent the standard error.

Table 3: Summary of unconjugated and conjugated particle deposition method

	Unconjugated (PAH) – 400gain			Conjugated (S.A) – 500gain		
	LOD [ng/mL]	LR Enh	Max Enh	LOD [ng/mL]	LR Enh	Max Enh
POEGMA(control)	0.26	-	-	0.16	-	-
Gold 5 nm post-cubes	0.26	74 ± 1	105 ± 15	0.39	13 ± 3	17 ± 8
Gold 10 nm post-cubes	0.21	84 ± 16	110 ± 23	0.16	14 ± 4	18 ± 3
Gold 15 nm post-cubes	0.14	52 ± 5	69 ± 22	0.08	12 ± 2	16 ± 2
Gold 20 nm post-cubes	0.16	40 ± 9	53 ± 9	0.02	12 ± 2	19 ± 7

The loss in enhancement in comparison to the conjugated case can be attributed to the decrease in non-specific binding of the nanocubes to the surface. Although this is desirable at lower concentrations for noise reduction purposes, the decrease in the density of cubes also affects the enhancement at the linear and upper BNP concentrations. SEM images (**Figure 22a**) show that the cube concentration is lower than that of the conjugated case as seen in chapter 3 for the same BNP concentration (62.5 ng/mL). White light reflection measurements were also taken to obtain the resonance behavior of the structure for different POEGMA thicknesses. As seen in **Figure 22b**, a blue shift of resonance occurs as the POEGMA thickness increases from 5nm to 20nm thick. However, the reflectivity measurements show that the absorption of light at the resonant frequency is low (less than 10%) in comparison to the nonconjugated nanoparticle deposition case, which is due to the low particle density on the surface.

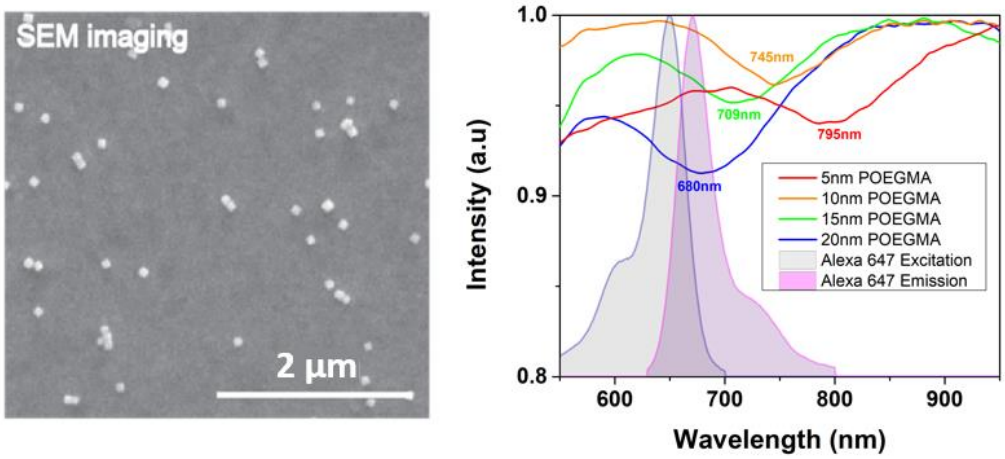

Figure 22: Optical response in conjugated nanocube deposition. a) SEM image of a cAb spot after assay has been performed (62.5 ng/mL BNP concentration) with conjugated silver nanocubes. b) Plasmonic resonance response for 5, 10, 15, and 20nm POEGMA obtained with reflectivity measurements.

4.3 Use of low-cost sensing components with the PED4

We tested the compatibility of the PED4 assay with a simple detection system, consisting of a low-cost detector, which is critical for future POCT applications. An inexpensive, 4.5 mW, 635 nm laser diode was used as the excitation source and an inexpensive and widely available black and white camera was used as the fluorescence detector. **Figure 23** shows the optical set up used for these experiments. The laser diode first goes through a 635 bandpass filter to remove any noise the diode might have. The laser beam then goes through a defocusing lens to increase the spot size of the laser (excitation size), which then enters a 50:50 beam splitter. The laser then goes through a 20x objective microscope and excites the fluorophore from the assay. The emission from the fluorophore is then redirected through the beam splitter and sent through a lens that

will focus the image to the camera. Before entering the camera, the emitted signal also goes through a 676/37 nm bandpass filter (Semrock) to block any leaked signal from the laser and to select the fluorescence emission from the Alexa647 fluorophore. The camera used is an ELP HD 1.3 Megapixel USB camera (Ailipu Technology Co. Ltd module 960P AR0130) .The image obtained by the camera was then processed in MATLAB to process the image.

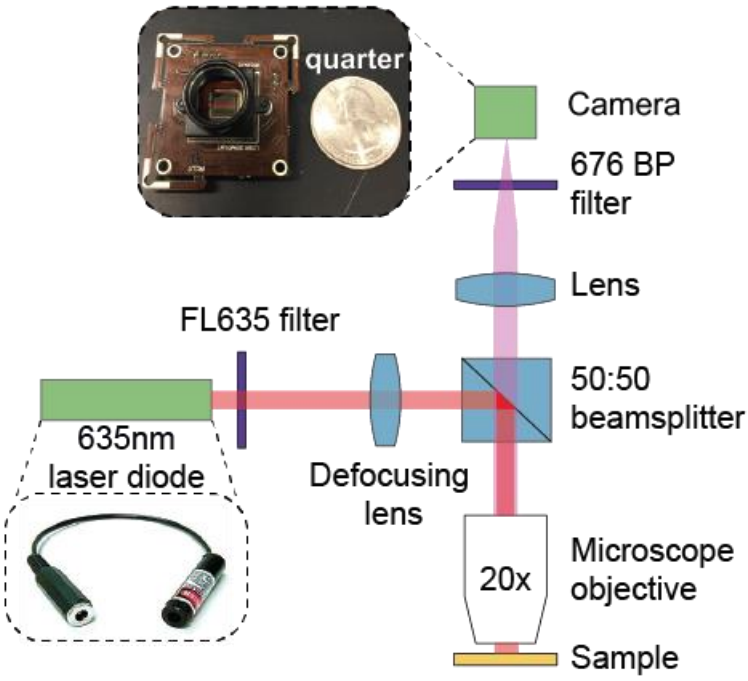

Figure 23: Portable excitation and detection scheme for POCT. a) Schematic of setup for fluorescence measurements using an inexpensive camera and laser diode for an assay made using the PAH particle deposition method.

As a side note, it is important to point out that a 20nm POEGMA glass control was used when performing experiments with the low-cost detector as opposed to the 70 nm glass control used in previous studies. This was done to keep the polymer thickness

consistent between the gold and glass surface. Unfortunately, further tests revealed that the 20 nm POEGMA thickness on glass was smaller than the measured value in the ellipsometer, and hence the fluorescence value was relatively smaller than current tests. Although this affects the fluorescence enhancement obtained, the experiments still serve as a preliminary demonstration of how low-cost detectors can be used to detect the PED4. **Figure 24a** shows the fluorescence images of the microspots for a PED4 assay obtained with the PAH particle deposition method on a 20 nm POEGMA brush on gold at different BNP concentrations down to 0.9 ng/ml. On a control sample, also consisting of the same assay but on 20 nm POEGMA coated glass, the spots are not visible even for the highest BNP concentration of 62.5 ng/ml. **Figure 24b** shows the dose-response behavior of the PED4 assay on gold and glass. It can be seen that the PED4 assay on gold exhibit a detectable fluorescence signal that is directly related to the spiked analyte concentration, while no fluorescence signal can be detected from the traditional D4 assay, independent of the analyte concentration used. This underscores the need to amplify the fluorescence signal to enable its readout by a low-cost detector.

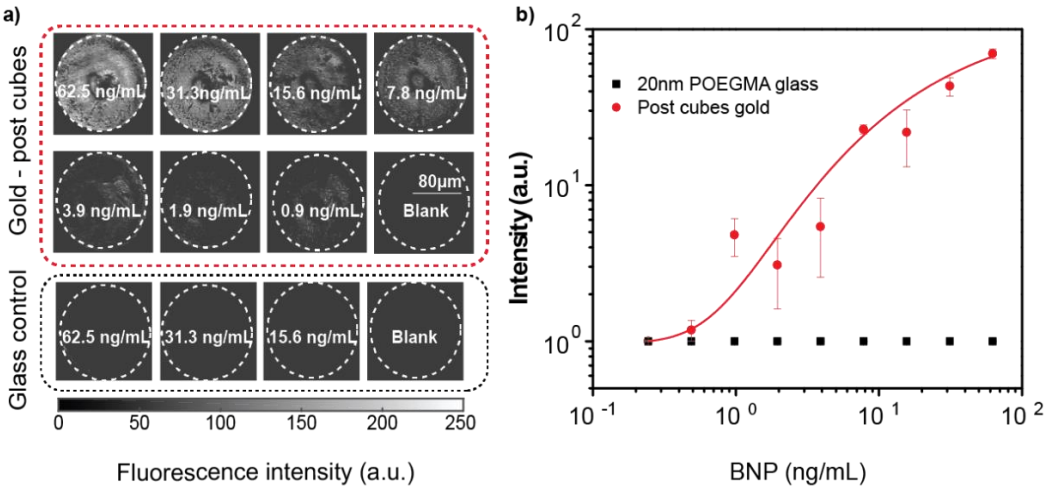

Figure 24: Portable excitation and detection scheme for POCT. a) Fluorescence images of PED4 (using PAH particle deposition method) and glass control samples (obtained using a 20× objective) for a range of BNP concentrations. Dashed white lines show the area for which the intensity was measured over. b) Average value obtained by repeating the measurements shown in a) for five different capture antibodies (cAb) spots for each concentration and the error bars indicate the standard deviation.

We also tested the feasibility of using the PED4 fabricated with conjugated nanocubes as seen in **Figure 25**. In this case, it was observed that the intensity captured by the camera is much lower than in **Figure 24** for the PAH deposition method. For instance, the largest concentration of BNP in **Figure 24b** reached intensity levels of about 80, as opposed to only an intensity of 2 as seen in **Figure 25b**. As previously seen, this is due to the low particle concentration in the conjugated case, which reduces the intensity values at upper concentrations and the linear regime of the assay. Although the fluorescence values are low for this assay, it still exciting to see that the simple set up can

detect the capture spots. Future work will consist in finding more optimal ways to deposit conjugated nanoparticles.

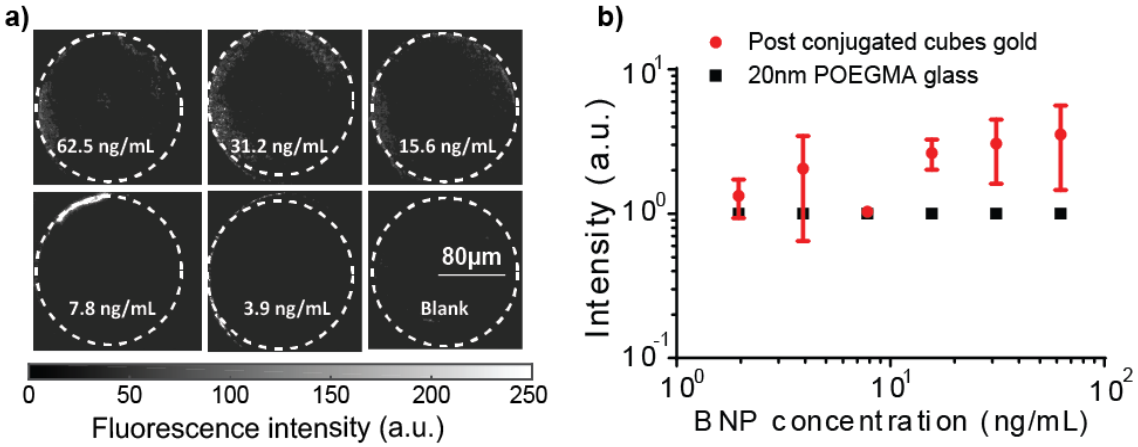

Figure 25: a) Fluorescence images of PED4 (using conjugated nanoparticles) for a range of BNP concentrations. Dashed white lines show the area for which the intensity was measured over. b) Average value obtained by repeating the measurements shown in a) for five different capture antibodies (cAb) spots for each concentration and the error bars indicate the standard deviation.

4.4 Integration of the PED4 with microfluidics

The use of microfluidics in POCT is important as they provide means for ease of automation, low cost, disposability, and small sample and reagent volume requirements[88]. Specifically, for capillary microfluidics, they are critical for POCT since they afford no real-time control over flow (and therefore they are referred as "passive") as opposed to "active devices" that require an external driving force, such as a pump[89]. Here we describe the fabrication and methods used for a proof of concept integration of plasmonic diagnostics and autonomous microfluidics capillary system. For this device, we make use

silicon-based technology due to the robustness and control it offers in creating small flow geometries. Some of the parameters that are considered in this section include channel geometry, hydrophilicity of the substrate, and hydrophilicity of the covering "lid". Design of the channel geometry and the surface chemistry of its solid support are important as they interplay with surface tension to provide with the necessary capillary force for autonomous liquid flow[90]. Capillary pressure arises at the liquid-air interface in a microchannel as a result of surface tension of the liquid and the curvature imposed by the fixed contact angles, which for wettable channels gives rise to a negative sucking pressure[91]. We made use of a rectangular channel geometry in this case, as it simple to fabricate and it is widely used.

In order to make the system robust and decrease the variability from sample to sample, the chips were made using photolithographic techniques taken from previous work[92]. The fabrication process is as follows: first, a clean silicon wafer was spin coated with the positive photoresist AZ 9260 at a speed of 1,800 rpm, a ramp of 1,000 rpm/sec, and a spin time of 60 sec. The wafer was then transferred to a hot plate at 110 ºC for 180 sec. The photomask was then loaded into the holder of a mask aligner and was run with an energy dosage of 1,400 mJ/cm^2 (e.g., for an output intensity of 13.5 mW/cm^2 a time exposure of 103.7 secs was used). The silicon wafer with the features was then placed in AZ 400K developer for 5 minutes and under constant shaking. The wafer was then removed from the developer and washed with steady stream of deionized water and dried with N_2 gas. As a result, the wafer would have a 10 µm thick layer of photoresist with the channels chemically removed.

In order to obtain a microfluidic channel that has a depth equal to the wafer thickness, the channels were further etched using deep reaction ion etcher (DRIE) for 350 cycles. To remove excess photoresist from the wafer, a large beaker with a solution of 1165 Photoresist Remover was placed on a hot plate at 65 ºC and the wafer was submerged for 1h. The wafer was then removed from the beaker and rinsed with alternating streams of acetone, isopropyl alcohol, and dried with N_2 gas. The wafer was then cut into the desired pieces (typically smaller size of a glass slide) using a scribe tool. In order for silicon wafer to bond to the glass slide, the surface has to be completely clean and free of organics. To obtain this, the wafers were submerged in a piranha solution (adding 30 wt.% H_2O_2 to 95% H_2SO_4 in a 1:3 ratio) and left overnight. The wafers were then carefully rinsed with deionized water, followed by a stream of acetone, methanol, and dried with N_2 gas.

A clean glass slide served as the supporting substrate of the microfluidic chip. A process known as anodic bonding was used to permanently bind the Si segment and the glass together. In this process, high pressure, high voltage, and high temperature are needed to facilitate ion drifting between glass and the silicon wafer[93]. Anodic bonding was performed the following way: with polished Si segment facing up, the glass was carefully placed on top of the Si segment and flipped while maintaining their position. Since the glass segment is larger than the Si segment, the two segments were secured with double-sided polyimide cleanroom tape, where half of the tape secures the vertical edges of the Si segment and the other half of the tape secures the overhanging glass. The segments were then flipped again such that the glass segment is on top the Si segment

and the Si wafer is placed on the surface of a metal slab on a hot plate. A second metal slab (at least 5 kg) was then carefully added directly on top of the assembled glass and Si segments. It is important to carefully check that the two metal slabs do not touch each other, otherwise a short circuit could be created. Using a high voltage power supply, one electrical lead (power) was connected to the metallic slab on top of the assembled glass and Si segments and the other lead (ground) to the bottom metallic slab. The power supply was then turned on to a voltage of 1,000 V and the hot plate was then turned on and left at 450 ºC for 2 hours to allow the glass to anodically bond to the Si substrate. After 2 hours, the hot plate was turned off and the leads were removed from the metal slabs. The metal slabs were left to cool down overnight and the top slap was then carefully removed from the top of the chips. **Figure 26** shows a picture of the silicon wafer chips with the microfluidic design bonded to the glass slide that will serve as the hydrophilic substrate.

Figure 26: Photograph of microfluidic chip in silicon after it has been bonded to glass using anodic bonding.

After the Si and glass segments had been permanently bonded, the chips were thoroughly cleaned with streams of acetone, followed by isopropyl alcohol, and methanol. After drying with N_2, the slides were then placed on a hot plate for 2 min at 95 ºC. Once completely dried, the slides were then placed in a dome for thermal evaporation with the glass substrate facing the dome and the open microfluidic features facing up, so that the evaporated metal can penetrate the chip and deposit on the glass underneath the features. During evaporation, Cr (5 nm) was used as adhesion layer, and Au (75 nm) as the metal substrate. Slides were then submerged in a thiol initiator overnight followed by polymerization of POEGMA via ARTP reaction as described in Chapter 2. **Figure 27a** shows a schematic of the overall procedure taken for the microfluidic chip fabrication. **Figure 27b** shows the chip before (left) and after (right) gold deposition and polymerization. **Figure 27c** shows a preliminary test to determine whether 20nm POEGMA is hydrophilic enough for liquid flow, where the left image shows the solution placed on one side of the microfluidics chip at t= 0 and the right side shows how the liquid moves to a waste chamber after 4 mins.

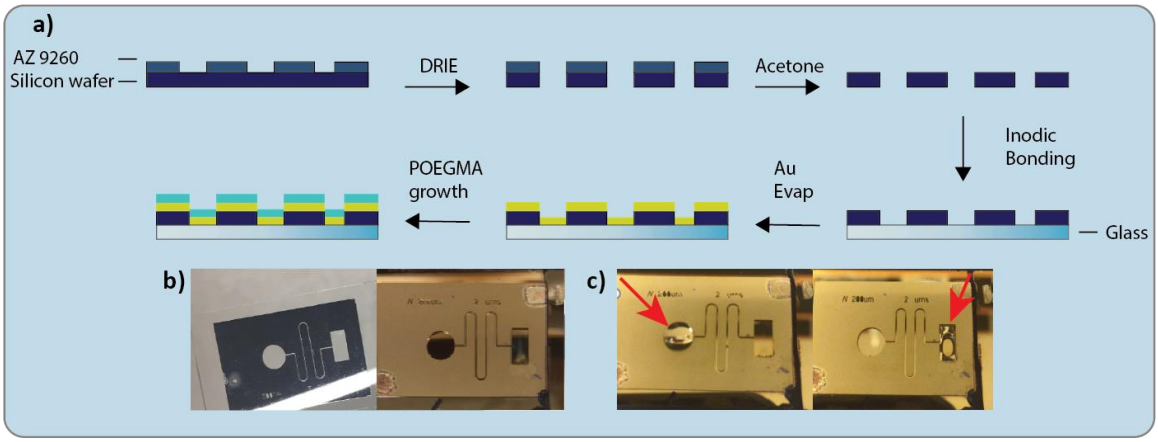

Figure 27: Mircofluidic fabrication using photolithography on a silicon wafer. a) Schematic showing photolithography procedure for the fabrication and integration of plasmonic diagnostics and autonomous microfluidics capillary system. Fabrication starts with photolithography performed on a silicon wafer covered with a positive photoresist, followed by deep reactive ion etching (DRIE), substrate cleaning, anodic bonding, gold evaporation on surface, and POEGMA growth. b) Chip after permanently bonding glass and silicon wafer through anodic bonding (left) and after evaporating gold and polymerizing substrate (right). c) Testing liquid flow after POEGMA polymerization (20nm thick) where red arrows show the location of liquid at t=0 (left) and t= 4 mins (right).

After testing the liquid flow in the chip, the microfluidic design was finalized by adding a hydrophilic microfluidic film on the surface of the chip to facilitate liquid flow and decrease the risk of creating bubbles. The new design consists of various components that allow for a complete system to work autonomously. These components are seen in **Figure 28** and include: a) the reaction chamber that will hold the printed antibodies (cAb, dAb) and will hold the solution for antigen incubation, b) the flow resistor (microfluidic channels) that are used to increase or decrease the flow rate depending on the channel dimensions, c) a waste reservoir which will hold the solution the liquid from away from the reaction chamber, d) a vent that is used to release air that accumulates in

the waste reservoir as it is pushed away from the channels, e) a filter with slow flow rate that will collect the waste as the waste reservoir gets full, and f) a hydrophilic cover film with 25µm double sided tape that is used to cover the chip. The hydrophilic top was fabricated by first laser cutting the features that will make contact with the liquid away from the double sided tape, which was then carefully taped to a hydrophilic film that has the reaction chamber and waste reservoir cut out, as seen in inset in **Figure 28.**

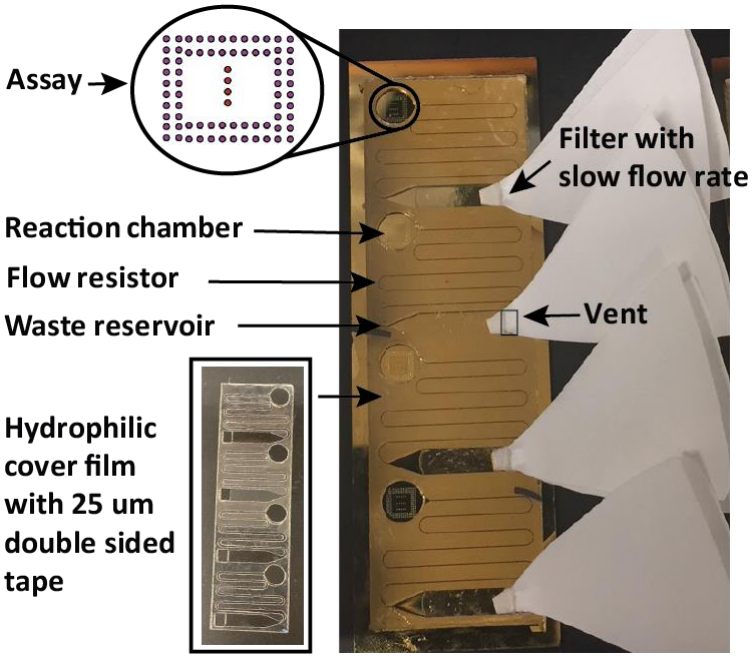

Figure 28: Microfluidic chip design with its main components.

After completing the design and fabrication procedures for the chip, we determined the antigen incubation time necessary to obtain a low limit of detection within the clinical regime of BNP when performing the assay. This was done by testing different assay times ranging from 1 minute to 90 minutes. **Figure 29** shows the calibration curves

obtained for these times with their corresponding LODs listed in the table. As seen in the table, the lowest incubation time necessary to obtain an LOD that is in the clinically relevant for BNP is 15 minutes, which gives an LOD of 0.28 ng/mL.

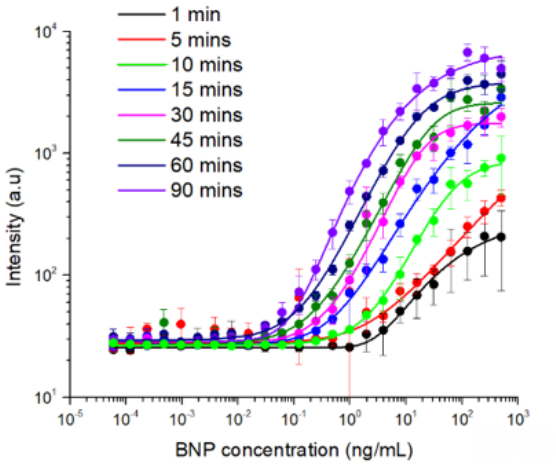

Incubation time	LOD (ng/mL)
1 min	4.50
5 mins	2.70
10 mins	0.61
15 mins	0.28
30 mins	0.14
45 mins	0.10
60 mins	0.04
90 mins	0.04

Figure 29: Calibration curves for different incubation times for BNP and a table summarizing the LODs obtained for the different incubation times.

The microfluidic chips were then designed to reach this targeted time of 15 mins by optimizing the length and the width of the channel. The prototype in **Figure 28** was then used to test three different BNP concentrations (500.00 ng/mL, 7.81 ng/mL, 0.48ng/mL and blank) and the ability to increase its fluorescence by attaching the silver nanocubes on the assay. To do this, three different chips were used to produce three repeats, where each chip had four channels for each concentration. For the prototype chip used, the length was 7mm, the width was 100µm, and the thickness was 500 µm. The chips were then tested by first placing 80 µL of FBS solution with the antigen in the

reaction chamber. After 15 minutes, 80µl of PAH solution was placed in the reaction chamber, and the same was done for SNC solution and washing buffer. **Figure 30a** shows the results of the microfluidic chip performance before and after adding the SNCs on the surface. It can be observed that the points before adding the SNCs (black dots) closely correspond to the fluorescence intensity values determined in **Figure 29**. Although a fluorescence increase of up to 2-fold was achieved after adding the SNCs, this was not comparable to the high fluorescence achieved in Chapter 3 or 4. By looking at SEM images (**Figure 30b),** it was determined that the low fluorescence enhancement most likely occurred due to the poor particle deposition while incubating the SNCs with the microfluidic chip. We believe this was due to the drying of the particle solution in the open reaction chamber. Future work will consist in designing a microfluidic chip that will have a closed reaction chamber that will allow for a more controlled environment for particle deposition. In addition a microfluidic chip that has double liquid chambers will be used to simultaneously hold the analyte and washing buffer, which will result in a single step microfluidic control of the assay without the need of washing steps.

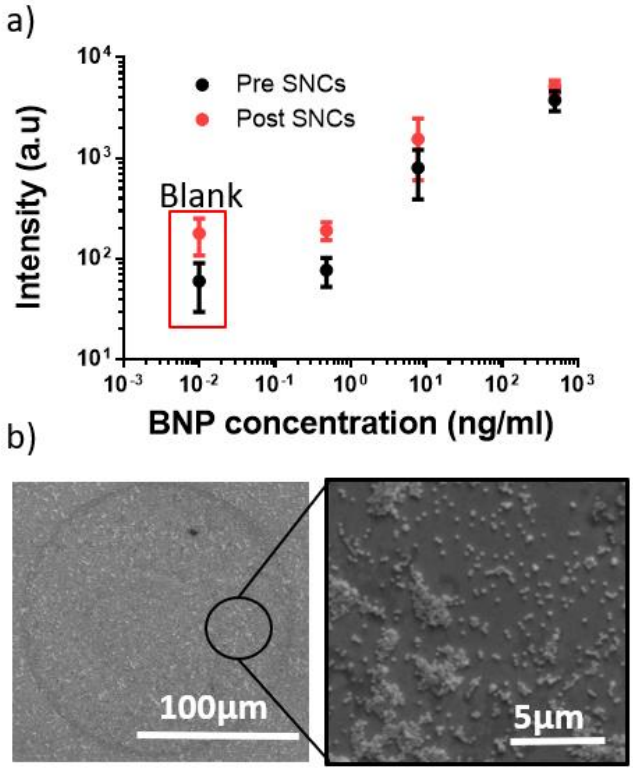

Figure 30: a) Microfluidic chip assay performance for four different BNP concentrations: 500 ng/mL, 7.81 ng/mL, 0.48ng/mL and blank. Error bars correspond to three repeats in three different chips. Fluorescence intensity was increased to ~2-fold. b) SEM images show ununiform particle deposition and aggregation due to drying of the particle solution.

4.5 Conclusion

This chapter has explored ways in which the PED4 can be translated into a single step POCT by simplifying methods to deposit the plasmonic components for fluorescence enhancement. It was demonstrated that conjugating the SNCs with a secondary antibody that targets the Fc region of the dAb allows us to reduce the number of steps needed in the PED4 assay. In addition, by controlling the concentration of SNCs on the assay, we

were able to reduce the noise introduced by the SNCs at low BNP concentrations, reducing the LOD from the control to ~8-fold.

It was also demonstrated that the PED4 can be detected with very inexpensive components consisting of a webcam and a laser diode (~$250 cost for both components) whereas the unenhanced D4 assay on glass could not be detected even for higher concentrations. This shows that the PED4 can serve as an inexpensive method to compensate for the loss of sensitivity when using inexpensive and less sensitive detectors.

To further move the PED4 towards a POCT, a microfluidic chip was fabricated using photolithography and reactive ion etching techniques to generate robust and highly replicable results. Preliminary results show that our chip can generate a dose-response curve with fluorescence intensity values corresponding to that of normal incubation. A 2-fold enhancement was observed when adding the SNCs on the assay with the microfluidic chip. We believe this enhancement can easily be increased by modifying the microfluidic design with a covered reaction chamber so that particle drying and aggregation can be avoided, which will be investigated in future work.

Chapter 5 Multiplexing capabilities with the PED4 for the prognosis of heart failure

5.1 Introduction

Heart failure is a chronic, progressive condition in which the heart muscle is unable to pump enough blood through the heart to meet the body's needs for blood and oxygen[94]. It is caused by structural and functional defects in myocardium, resulting in impairment of ventricular filling or the ejection of blood [95]. There are a wide variety of medical conditions that can contribute to heart failure, including atrial fibrillation, myocardial ischemia, being overweight, smoking, and physical inactivity[94].

Heart failure is a growing public health problem as it remains the leading cause of death in the US and worldwide, with survival rates worse than those for bowel, breast, and prostate cancer [83]. According to the 2019 update on the heart disease and stroke statistics, an estimated 6.2 million Americans (20 years or older) had heart failure between 2013 and 2016 [96]. Furthermore, projections show that heart failure will increase 46% from 2012 – 2030, causing significant burden on health care systems across the globe. Specifically, it has cost the US an estimated $30.7 billion in 2012, covering for health care services, medicine, and missed days of work[97].

One of the main challenges with heart failure is that its diagnosis and prognosis can be difficult, as many of the symptoms of heart failure are non-discriminating and of limited diagnostic value [98]. Furthermore, symptoms and signs may be particularly difficult to identify and interpret in obese individuals, in the elderly, and in patients with

chronic lung disease[99,100]. Therefore, demonstration of an underlying cause is central to the diagnosis of heart failure. For this, the echocardiogram and electrocardiogram can be useful tests. However, because the signs and symptoms of heart failure are so non-specific, many patients with suspected heart failure referred for echocardiography are not found to have an important cardiac abnormality [98]. This becomes a problem in the health sector as poor risk stratification brings unnecessary healthcare costs, delays in accurate diagnosis, and poor managing of patients who could be at higher risk. As an alternative approach, biomarkers provide a low cost, low risk, and quick turnaround method to confirm or exclude a heart failure diagnosis, help to establish prognosis in the diagnosis, and may provide information on the complex pathophysiology of heart failure [101].

Since heart failure is a complex syndrome involving diverse pathways and pathological processes, testing blood concentrations of biomarkers has become important, with natriuretic peptides leading the way as a diagnostic and prognostic tool for the diagnosis and management of this disease[100]. Although these peptides have become the gold standard for heart failure diagnosis, more recent evidence suggests that natriuretic peptides along with the next generation of biomarkers may provide added value to medical management, which could potentially lower risk of mortality, readmissions, and related costs [102]. **Figure 31** shows the various pathways contributing to the development and progression of heart failure and biomarkers representative of the various pathways.

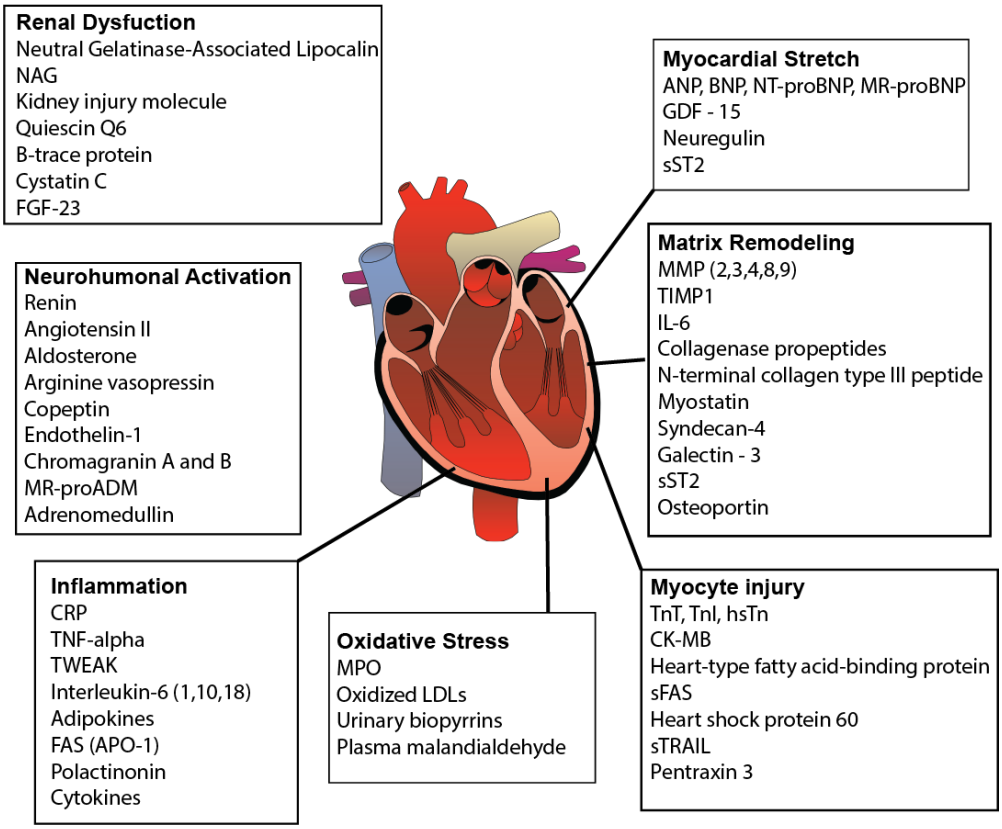

Figure 31: **Pathophysiologic pathways contributing to the development and progression of heart failure with a representation of the release of various biomarkers. Monitoring of biomarker activity can be used to understand these pathophysiological processes in patients. This chapter will focus on NT-proBNP: Amino Terminal Natriuretic Peptide; Galectin-3; cTnI and cTnT: troponin I and troponin T; CRP: C-reactive protein; and NGAL: Neutrophil gelatinase associated lipocalin.**

5.2 Candidate biomarkers for multiplexing in the PED4

In this chapter we will consider several heart failure biomarkers based on the various pathophysiologic pathways they represent, and they will be tested in the D4 assay in a multiplex format. Doing these tests in the D4 will allow us to 1) quickly identify the biomarkers that can be tested together without cross-reactivity issues and 2) assess the

sensitivity in these selected biomarkers. The biomarkers that will be tested include: N-terminal-proBNP, cardiac troponin I and T (cTnI, cTnT), C-reactive protein (CRP), galectin-3, and neutrophil gelatinase-associated lipocalin (NGAL).

5.2.1 Markers of myocyte strain

N-terminal-pro-B-type natriuretic peptide (NT-proBNP, 8.5 kDa): The natriuretic peptides are family of circulating peptides that play a critical role in the regulation of cardiovascular homeostasis[103]. The most validated of these as cardiovascular biomarkers are b-type natriuretic peptide (BNP) and its amino-terminal fragment (NT-proBNP). BNP and NT-proBNP are released by the cardiac myocytes in response to increased wall stress due to heart failure and myocardial dysfunction, which can counteract the stress by inducing vasodilation [104] . Results from the Val-HeFT study (Valsartan Heart Failure Trial) reported by Masson *et al* demonstrated that BNP and NT-proBNP were the strongest predictors of mortality and hospitalization for heart failure [105], and BNP and NT-proBNP have become the gold standard for its diagnosis and prognosis. Furthermore, in some studies, NT-proBNP has been shown to be superior over other natriuretic peptides[106]. BNP, NT-proBNP, and proBNP levels at hospital admission and discharge in patients with acute decompensated heart failure (ADHF) were compared for their predictive value of cardiac death and all-cause mortality within 90 days post discharge. NT-proBNP had superior prognostic power for all-cause mortality when compared with BNP and proBNP, suggesting that discharge values of NT-proBNP have the greatest diagnostic and prognostic potential of all natriuretic peptides [106] . Furthermore, in the PRIDE study (the N-terminal Pro-BNP investigation of dyspnea in the emergency

department) [107] patients with ADHF had significantly higher NT-proBNP concentrations compared with patients without heart failure (median, 4054 pg/mL versus 131 pg/mL). In addition, rising NT-proBNP concentrations correlated well with increasing severity of heart failure and was the strongest predictor of ADHF diagnosis.

5.2.2 Markers of myocyte injury

Cardiac troponin: Cardiac troponin (cTn) is the core biomarker for the diagnosis of a myocardial infarct (MI) and is caused by myocyte injury[108]. While troponin level elevation is not diagnostic of acute heart failure, there is evidence demonstrating increased morbidity and mortality rates in patients presenting with acute heart failure and elevated cTn levels [109]. For instance, in the EFECT (Enhanced Feedback for Effective Cardiac Treatment) study involving 2,025 patients, a peak cTnI > 0.5 ng/mL measure in the first 48 hours of hospitalization was an independent predictor of all-cause mortality at 1 year. Like cTnI, elevated levels of cTnT in patients with acute heart failure have demonstrated increased rates of adverse events. An elevated cTnT level (> 0.1 ng/mL) on admission has been associated with increased risks of heart failure readmission and mortality [109].

5.2.3 Inflammatory markers in heart failure

C-reactive protein (CRP): C-reactive protein (CRP) is a circulating biomarker that reflects systemic inflammatory state and has been associated with presence of heart failure and cardiovascular risk [110,111]. For instance, a large study by Engtrom et al. found that those with a CRP ≥ 3 µg/mL were twice as likely to be hospitalized with heart failure over a mean following up of 13 years [112].

5.2.4 Markers of myocyte remodeling

Galectin-3 (26 kDa) Inflammatory and fibrotic processes are central to cardiac remodeling and the development of heart failure[113]. Galectin-3, which is secreted by macrophages, causes cardiac fibrosis via proliferation of cardiac fibroblasts and cross-linking of collagen I [104]. Recent clinical and prognosis value has been given to galectin-3 in context of heart failure. For instance, in the COACH trial, it was shown that doubling of galectin-3 was associated with twice the risk of death or rehospitalization over a mean follow-up period of 18 months[114]. In another study galectin-3 had shown strong prognostic value in the prediction of death and recurrent heart failure within 60 days, with median concentrations of Gal-3 significantly higher in subjects dying by 60 days of follow-up (12.9 ng/mL) than in those surviving (9.0 ng/mL) [115].

5.2.5 Markers in comorbidities associated with heart failure

Neutrophil gelatinase-associated lipocalin (NGAL, 25 kDa) NGAL is a protein involved in response to injury of epithelial cells, such as those in the kidneys and is a marker of kidney injury and kidney disease[116]. Chronic heart failure patients have been found to have significantly higher levels of both serum and urine NGAL when compared with control subjects. In a recent GALLANT study [117] it was demonstrated the prognostic utility of plasma NGAL along with BNP in 186 patients with acutely decompensated heart failure, where it was shown that patients with higher NGAL levels had significantly more heart failure-related adverse outcomes in 30-days than those with lower levels (134 vs. 84 ng/mL). Future research can benefit by further exploring the role of NGAL in combination with NPs in order to reduce diuretic overuse and timely discharge patients

with acute and chronic HF. In another study, higher plasma NGAL than the median of 85 (60-123) ng/mL were independently associated win an increased risk of all-cause mortality in patients with and without chronic kidney disease[118]. It has also been suggested that using both NGAL and BNP can serve in the risk stratification of those with acute heart failure[104].

Currently, cardiovascular biomarkers are mostly tested in a central hospital laboratory, and options for point of care testing (POCT) are limited. Some of the testing techniques available in the clinical setting include i-STAT (Abbott), Meritas (Trinity Biotech) and Triage (Alere), however these assays are far too expensive, cumbersome, and engineered for the detection of individual biomarkers. Hence their use is limited when trying to understand the main pathophysiological stages involved in heart failure, and when testing multi-biomarkers outside of the hospital setting with appropriate analytical precision. In order to circumvent these limitations, we propose the use of the PED4 assay for multiplex testing of cardiac biomarkers with less sensitive detectors, such as cellphones, that will allow self-testing and monitoring of biomarker concentrations. This will reduce the number of visits to the clinic, expedite diagnosis, prognostication and clinical decision making, as well as reduce the general cost that clinical testing brings.

5.3 Multiplex testing of biomarkers in the D4 and PED4 assay

Glass slides with a 50 nm POEGMA polymer brush were used to test the multiplexing behavior of our assay before moving to a plasmonic cavity. Sets of different capture and detection antibodies were printed simultaneously on the surface of

POEGMA. For this, an inkjet-printer was used to spatially immobilize distinct cAbs at a concentration of 1 mg/mL. To print the detection antibodies, a solution of 10% trehalose was first printed around the cAbs and let dry for three minutes (named “trehalose pads”), then a mixture of all dAbs (at a concentration of 0.03 mg/mL in PBS) was printed on top of the trehalose pads, which allows dAbs to better dissolve from the surface. As seen in **Figure 32a**, the spatial distribution of the cAbs allows for the detection of multiple targets in a single chip with the same fluorescence reporter [9]. Here, cAbs for NT-proBNP, galectin-3, and NGAL are printed in three distinct rows, and a solution of all three dAbs (in 10% trehalose) for NT-proBNP, galectin-3, and NGAL are printed around these spots. **Figure 32b** shows the basic mechanism of monoplex and multiplex detection using this printed configuration. If the sample solution has the NT-proBNP antigen present and no other biomarker, only the first row will produce a fluorescence signal. Similarly, if the only antigen in the solution is Galectin-3, the second row will be detected; and if only NGAL antigen is present, only the third row will fluoresce. Finally, in the case where all antigens are present, all three rows will produce a signal.

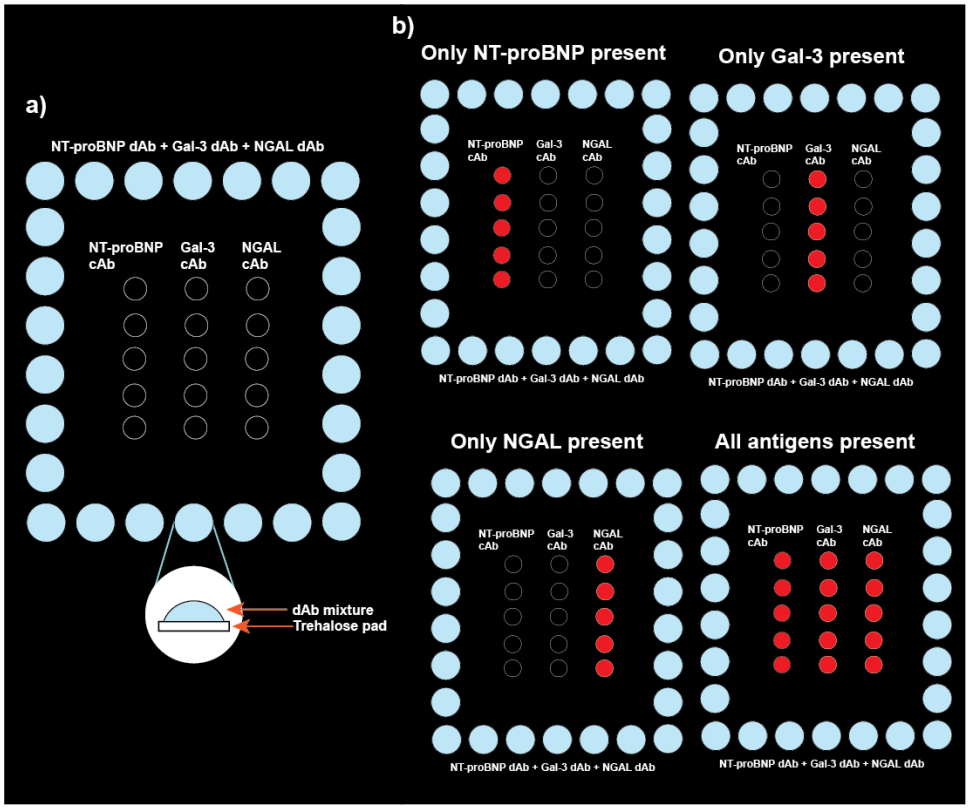

Figure 32: Multiplex detection using the D4 assay. a) Detection antibodies are printed in distinct rows while capture antibodies are mixed and printed on a trehalose pad composed of 10% trehalose drops. b) Fluorescence signal is observed in cAb spots that correspond to the antigen present. All spots fluoresce when all antigens are added.

To test the performance of the multiplex assay and assess whether the limit of detection for each of the antigens of interest are in the clinically relevant regime for prognosis of heart failure, we first tested the assay in 50nm thick POEGMA glass slides. This allowed us to rapidly optimize antibody pair selection and look out for cross-reactivity between antibodies. The first set of antigens tested together were those of NT-proBNP, CRP, and cTnT, as seen in **Figure 33**. For this, all cAbs and dAbs were printed on the surface of a 50 nm POEGMA glass slide. When testing this set of antigens, it was

seen that NT-proBNP had a good performance when tested in a monoplex format as seen in **Figure 33a**. However, when the monoplex assay for cTnT antigen was tested, a dose response curve was not generated, which could be attributed to the high background created in the assay due to cross-reactivity between the cTnT detection antibody and FBS. This was further explored when testing cTnI (see below). In the case of CRP, a cross-reactivity free dose-response curve was also generated. Unfortunately, the dose-response curve saturates at the high concentrations of CRP, which are of interest for heart failure (≥ 3 µg/mL). Different optimization procedures were performed to increase the dynamic range of the dose response curve and capture the higher concentrations, such as decreasing the dAb and cAb concentrations, and decreasing the photodetector gain. However, the dose response would still saturate at he needed concentrations. It was then decided to test different antigens that would be within the dynamic range of the D4 assay and do not cross-react with other antibodies or our testing serum FBS.

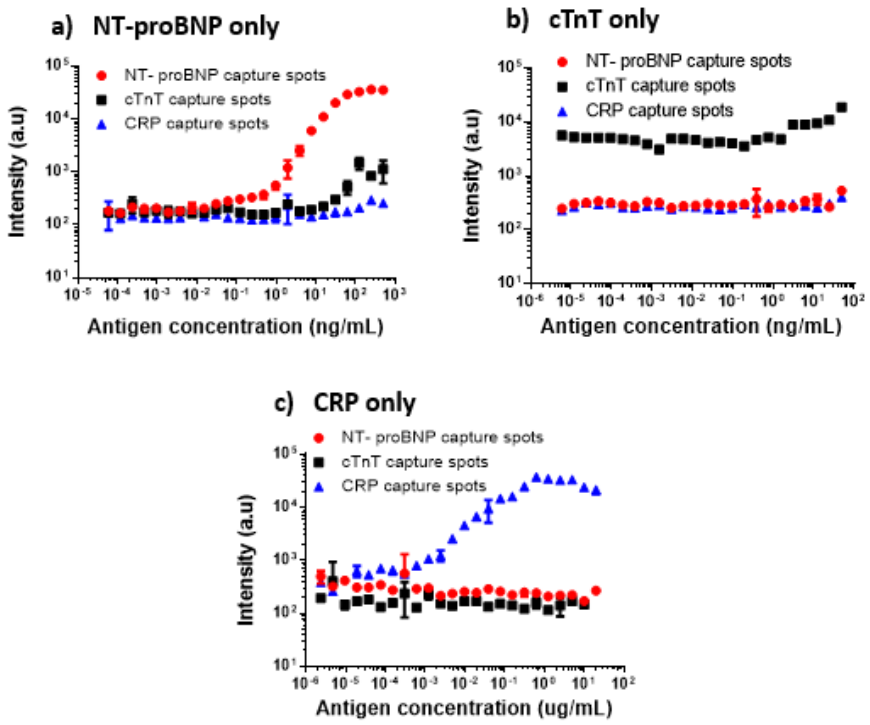

Figure 33: **First multiplex biomarker test consisted of NT-proBNP, cTnT, and CRP. a) shows the monoplex assay when only NT-proBNP was added to the D4 assay, b) when only cTnT was added, and c) when only CRP was present. Background noise in the dose-response curve of cTnT is due to cross-reactivity of FBS serum and cTnT cAb.**

The next antigen tested was Galectin-3 since its clinical values for heart failure fall well within the dynamic range of the D4 assay (17.8 – 94.8 ng/mL). This new antigen was first tested as a duplex assay with NT-proBNP since it had shown promise in our previous tests. As before, this assay was tested by printing both capture antibodies for NT-proBNP and Galecting-3 and a mixture of both detection antibodies for NT-proBNP and Galectin-3 in the same slides. **Figure 34a** shows the monoplex assay for NT-proBNP with no signs of cross-reactivity between the antibodies or antigens. Similarly, the

monoplex assay for Galectin-3 (**Figure 34b**) did not present cross-reactivity issues. When adding the two antigens together in a duplex format (**Figure 34c**) two dose response curves were generated as expected. Finally, to test the possibility of fluorescence enhancement with the PED4 in a duplex format, the assay was tested on gold slides followed by the deposition of silver nanocubes using a PAH interfacial layer (**Figure 34d**). When compared to glass control, results produced an average enhancement of 30-fold and a maximum enhancement of 65-fold.

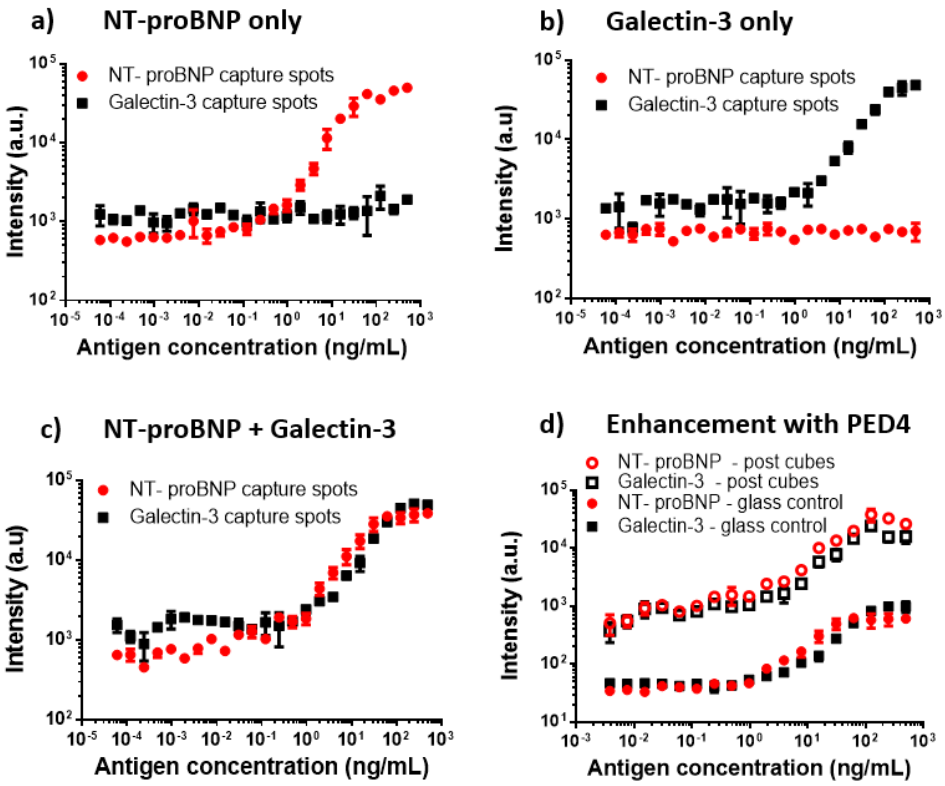

Figure 34: Duplex assay test for NT-proBNP and galectin-3. a) shows the monoplex assay when only NT-proBNP was added to the D4 assay, b) when only galectin-3 was added, and c) when both NT-proBNP and galectin-3 were present. d) Preliminary test of duplex assay with PED4, which gives an average enhancement of 30-fold in the linear regime of the dose-response curve.

After determining that NT-proBNP and galectin-3 assays work well together, cTnI was tested due to its known prognostic value in heart failure and MI. Unfortunately, when testing this assay with the two other antigens (**Figure 35a**), a high background level was observed for cTnI, giving an LOD that was higher (1.45 ng/mL) than the cTnI clinical values needed for the prognosis of heart failure (0.5 ng/mL). Further tests revealed that when testing cTnI by printing cTnI dAbs only on the slide, the dAbs cross-reacted with the cAbs for NT-proBNP and Galectin-3, specially at higher concentrations (**Figure 35b**, red and blue curve) while maintaining high background (black line). To determine whether the high background level in the cTnI dose-response curve comes from cross-reactivity with the diluting serum FBS, an assay was tested by printing cTnI dAb only as in **Figure 35b**, except that PBS + 1% BSA was used instead of FBS. From this, it was observed that the background in the dose-response curve was significantly lowered as seen in the black curve in **Figure 35c**. As expected, cross-reactivity with the other detection antibodies was still observed under these conditions. The background noise in cTnI could be reduced by using cTnI depleted serums. However, since the purpose of this study is to develop a robust POCT that works with complex fluids, a different cardiac biomarker was tested.

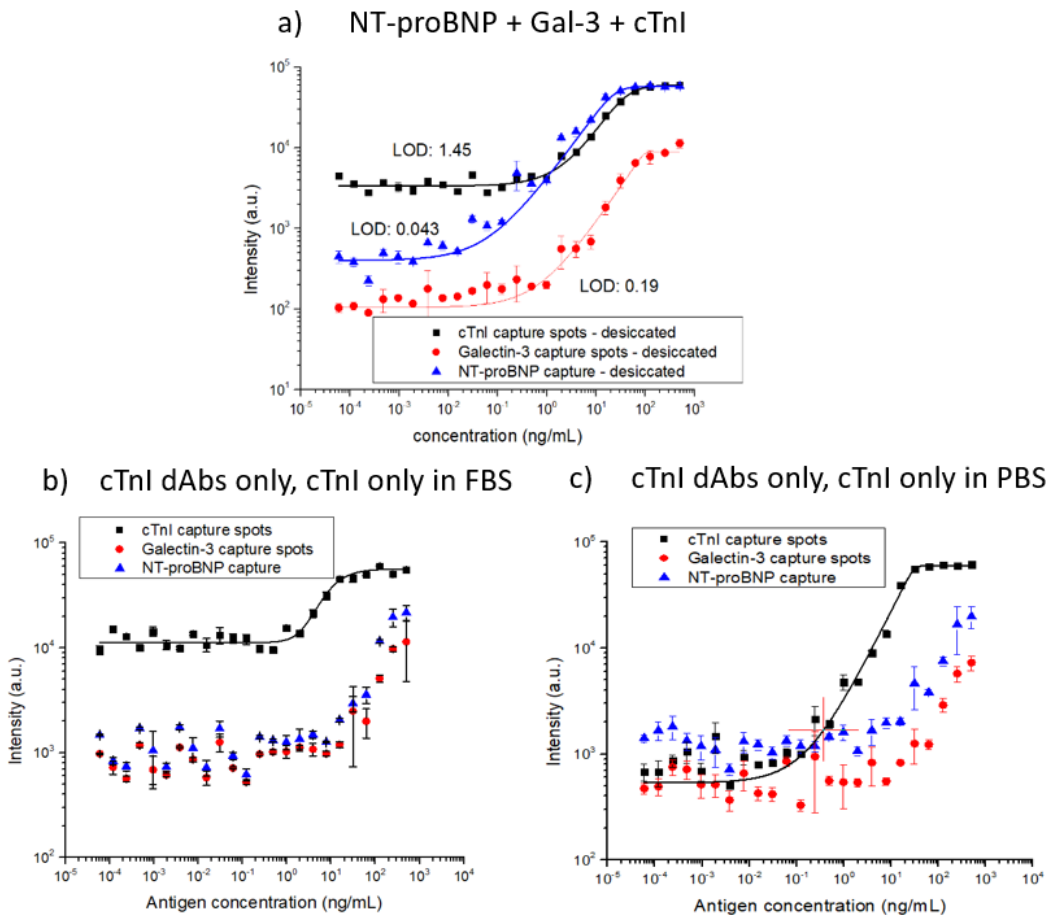

Figure 35: Multiplex assay test for NT-proBNP, Galectin-3, and cTnI. a) shows the multiplex assay for the three antigens. NT-proBNP and Galectin-3 had LODs and dynamic ranges needed for diagnosis and prognosis of heart failure. However LOD of cTnI was high due to background noise b) Running cTnI assay with only cTnI dAbs revealed cross-reactivity between cAb spots from other antigens and cTnI dAb c) Background noise from cTnI assay was reduced when running assay in PBS+1%BSA instead of FBS. However, cross-reactivity with cTnI dAb was still present.

Another good candidate for our multiplex assay is NGAL since prognostic values for heart failure fall within the dynamic range of the D4 assay. When testing this antigen along with NT-proBNP and galectin-3, no cross-reactivity issues were observed, and the

clinical values were maintained in the linear regime of the assays. **Figure 36** shows the curves created for both monoplex and multiplex assays where the tested slides had been printed with all cAbs and dAbs. **Figure 36a** shows the dose-response curve for NGAL when tested independently, with a LOD of 0.10 ng/mL (prognostic value > 85 ng/mL), **Figure 36b** shows the monplex assay for NT-proBNP, giving an LOD of 0.03 ng/mL (diagnostic value 0.30 – 1.80 ng/mL), **Figure 36c** shows the monoplex assay of Galectin-3 with an LOD of 0.56 ng/mL (prognostic value 17.80 – 94.80 ng/mL), and **Figure 36d** shows the multiplex test of all three biomarkers, giving an LOD of 0.04 ng/mL, 0.02 ng/mL, and 0.34 ng/mL for NGAL, NT-proBNP, and Galectin-3 correspondingly. There was no sign of cross-reactivity in the assays with nonspecific antibodies or FBS.

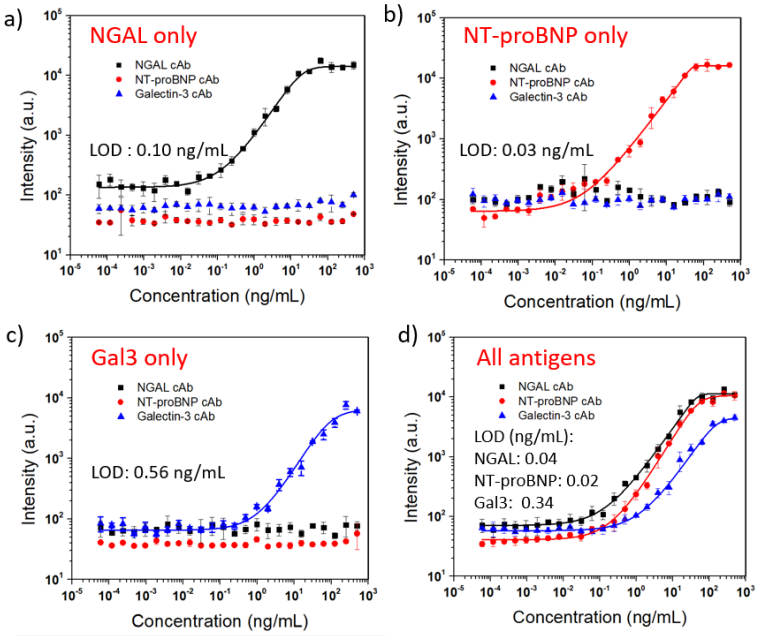

Figure 36: Multiplex assay for NT-proBNP, Gal-3, and NGAL. a) Monoplex assay when only NGAL is present b) when only NT-proBNP is present c) when only Gal-3 is present, and d) when a mixture of all antigens are added to the assay. No cross-reactivity was observed and LODs for all antigens were within the clinical values needed for the diagnosis and prognosis of heart failure.

Table 4: Limit of detection obtained for NT-proBNP, Galectin-3 and NGAL

	Clinical Range (ng/mL)	**Monoplex assay (ng/mL)**	**Multiplex assay (ng/mL)**
NT-proBNP	0.30 – 1.80	0.03	0.02
Galectin-3	> 9.0	0.56	0.34
NGAL	> 50	0.10	0.04

5.4 Enhancement of multiplex assay with silver nanoparticles

After performing cross-reactivity tests in the multiplex assay, the fluorescence signal from the three cAb spots was enhanced by printing the D4 assay on gold evaporated glass slides and by attaching silver nanocubes through a PAH layer, as described in Chapter 3. When scanning the assay with a photodetector gain of 350, the linear enhancement obtained when compared to glass control was that of 14-fold for NT-proBNP, 16-fold for Galectin-3, and 19-fold for NGAL as seen in **Figure 37**. We believe that the lower enhancement obtained when compared to previous results for the same POEGMA thickness (~40-fold) comes from the variability in the different cAbs.

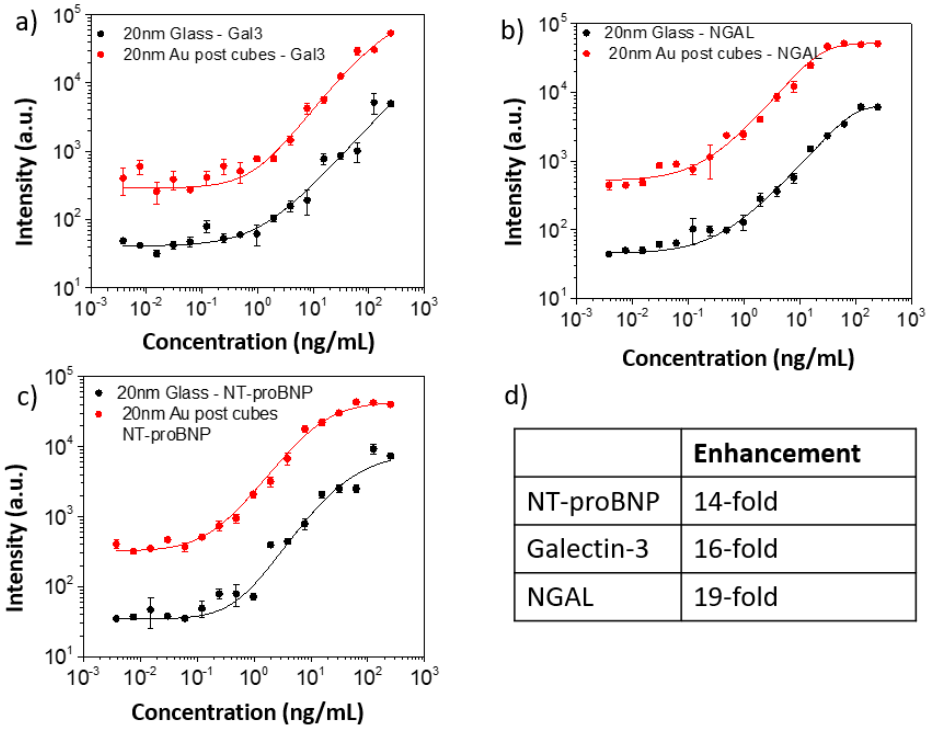

	Enhancement
NT-proBNP	14-fold
Galectin-3	16-fold
NGAL	19-fold

Figure 37: Fluorescence enhancement for multiplexed assay. Black lines represent glass control and red lines assay for the PED4. a) Enhancement for Galectin-3, b) enhancement for NGAL and c) enhancement for NT-proBNP.

Printing different antibodies on the same surface also allows us to study the impact of the polymer surface on the plasmonic behavior of the structure. To further explore the effect of antibody immobilization on the surface, SEM and AFM images were taken from the NT-proBNP, Galectin-3, and NGAL cAb spots (**Figure 38**). Since the antibodies are immobilized on a gold evaporated substrate (therefore minimizing charging effects when imaging in the SEM), we have the opportunity to directly observe the behavior of the antibody under different conditions, such as different antibody types, different polymer brush thickness, and when additives are added to the antibodies. This

is the first time that the D4 assay has been observed and characterized in such detail, opening ways to better understand cAb immobilization and device strategies to obtain uniform and thin antibody thickness on the POEGMA surface for fluorescence enhancement.

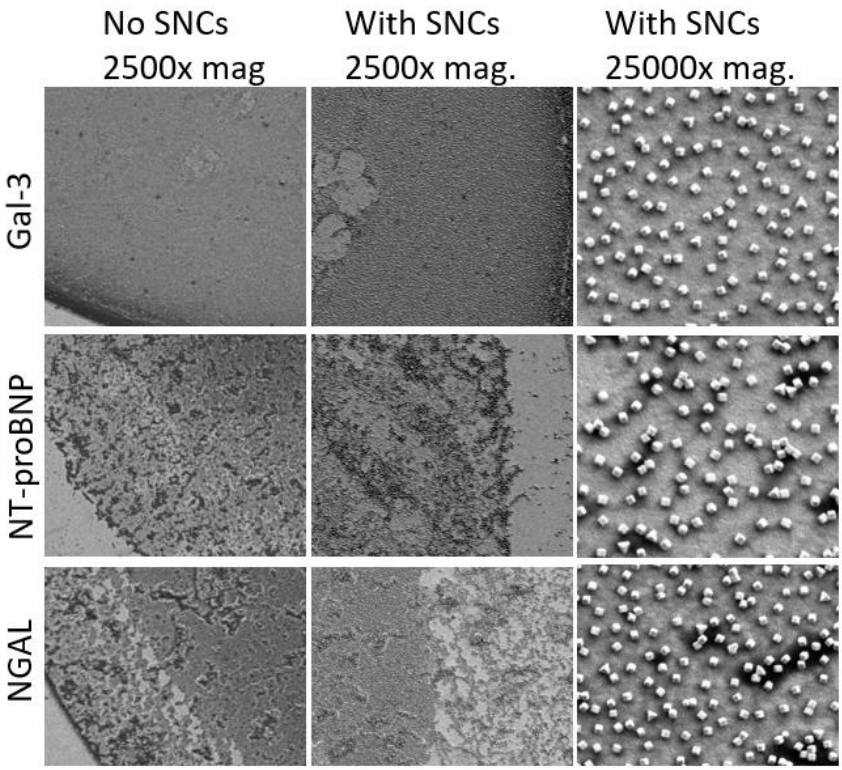

Figure 38: shows SEM images of cAb for Galectin-3, NT-proBNP, and NGAL when printed on a 20nm POEGMA gold slide. As seen from the first row, galectin-3 has a uniform distribution of antibody on the surface, with a good distribution of SNCs as seen at 2500x magnification and 25000x magnification. In the case of NT-proBNP and NGAL (second and third row, respectively) it is evident that the cAb spots present high levels of aggregation as seen by the darker spots. Although the SNC distribution is similar as in the case of galectin-3, high variation of antibody uniformity and thickness can lead a shift in plasmonic resonance away from the fluorophore emission and excitation, as well as drop in the fluorescence enhancement.

Absorption measurements from the PED4 were obtained for the three different antibody spots as seen in **Figure 39**. It is observed from here that the resonance for galectin-3 is 655 nm and is close to the fluorophore absorption and emission. This is consistent with our previous result with BNP (Chapter 3) due to the small (<10 nm) thickness of the sandwich assay. However, the plasmonic resonance for NT-proBNP and NGAL is highly shifted to 542 nm due to the higher average thickness caused by antibody aggregation. This blue resonance is consistent to previous studies performed in SNC metasurfaces [77,78], where it was shown that increasing the dielectric gap causes blue-shift in resonance.

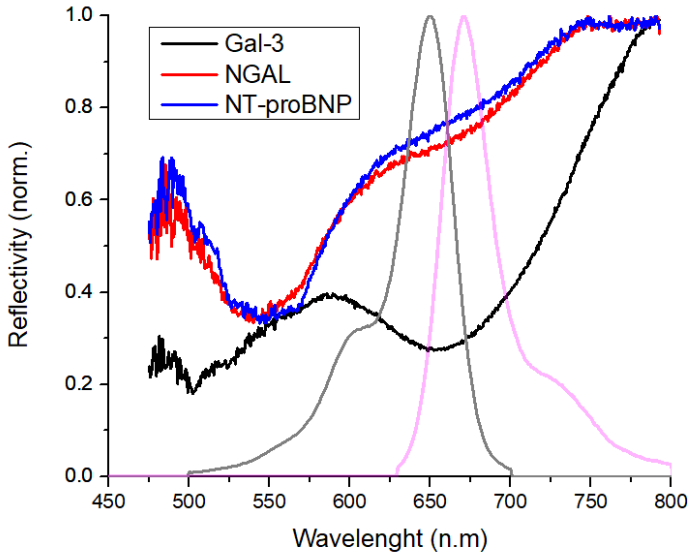

Figure 39: Plasmon resonance in PED4 for NT-proBNP. Resonance blue shifted 50nm from 721nm to 671nm when increasing the POEGMA thickness from 5nm to 20nm.

AFM measurements were also performed on the sandwich immunoassay to determine its total thickness and surface roughness. **Figures 40-43** show AFM images of Galectin-3, NT-proBNP, and NGAL. For all three figures, image a) shows a representative SEM image of the capture spots after the assay has been performed. Image b) is an AFM image of the same spot, with c) showing a 1 µm x 1 µm AFM image of the same spot used to calculate the surface roughness of the assay, and d) shows the phase information from image c). From **Figure 40**, it can be observed that Galectin-3 had the best antibody immobilization since it has a thin assay thickness of about 7 nm and mean roughness (Rq value) of 5 nm. It is also interesting to note that the phase contrast gives information about the physical properties of the surface, in this case the contrast between a soft, more elastic material of the antibody, and that of the polymer surface, as seen by **Figure 40d**.

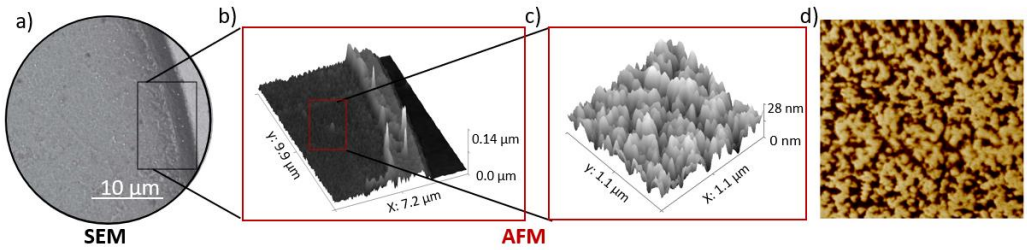

Figure 40: SEM and AFM analysis for Galectin-3. a) SEM image of spot to be analyzed in AFM, that can be also be used to determine antibody uniformity. b) AFM of antibody edge used to determine thickness (10 µm X 10 µm image), this image gives an average thickness of 7 nm across a rectangular section c) 1 µm X 1 µm AFM image used to extract surface roughness (R_q value of 5 nm), with d) showing its phase information.

In the case of NGAL, the total assay thickness was larger than that of Galectin-3 due to antibody aggregation and crystallization while drying, which was not observed in Galectin-3. NGAL assay had more variability in thickness with average thickness of 15 nm, and individual aggregates that went up to 84 nm in height for a given image. Roughness was also higher in comparison to Galectin-3, where NGAL had a of about 12 nm for a 1 µm x 1 µm image. It is also interesting to see how the variability in antibody aggregation can be seen in the phase information, where compared to Galectin-3, as NGAL presents much larger aggregates.

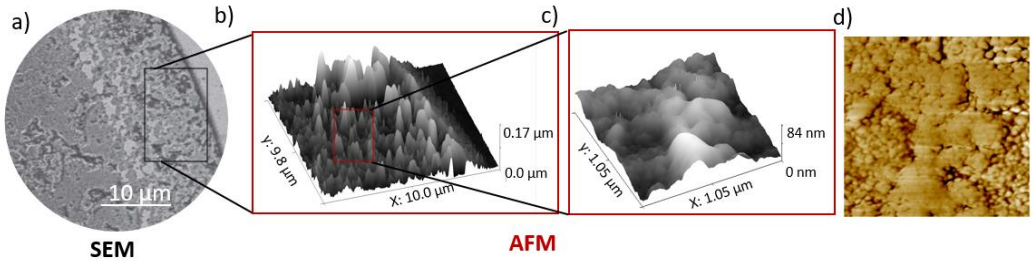

Figure 41: SEM and AFM analysis for NGAL. a) SEM image of spot to be analyzed in AFM, that can be also be used to determine antibody uniformity. b) AFM of antibody edge used to determine thickness (10 µm X 10 µm image), this image gives an average thickness of 15 nm across a rectangular section c) 1 µm X 1 µm AFM image used to extract surface roughness (R_q value of 12 nm), with d) showing its phase information.

NT-proBNP also presented more aggregated antibodies (**Figure 42**), with thickness that averaged 18 nm and with individual aggregates that reached ~63 nm. Future work will involve the investigation of methods to increase antibody uniformity on

the surface such as additive selection, polymer brush thickness, and humidity control while printing, all of which will be discussed further in Chapter 6.

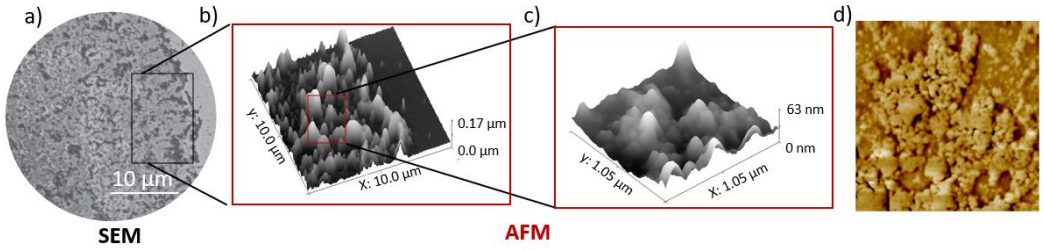

Figure 42: SEM and AFM analysis for NT-proBNP. a) SEM image of spot to be analyzed in AFM, that can be also be used to determine antibody uniformity. b) AFM of antibody edge used to determine thickness (10 µm X 10 µm image), this image gives an average thickness of 18 nm across a rectangular section c) 1 µm X 1 µm AFM image used to extract surface roughness (R_q value of 13 nm), with d) showing its phase information.

5.5 Conclusion

In conclusion, this chapter focused on the use of multiplexity capabilities of the D4 and PED4 assay to simultaneously detect multiple biomarkers with a single fluorescence reporter. A few cardiac biomarkers were tested with each other to determine the right combination of antibody pairs that would generate dose-response curves without cross-reactivity. The three biomarkers that were successfully tested in a multiplex format were galectin-3, NT-proBNP, and NGAL. We believe that troponin biomarkers such as cTnI and cTnT can also be added to our assay by optimization of the antigen carrier fluid. This can be done by selecting a cTn depleted fluid, option that will be investigated in future studies. Fluorescence intensity of the multiplexed D4 assay was increased by 14-fold for NT-proBNP, 16-fold for Galectin-3, and 19-fold for NGAL with

the addition of silver nanocubes on a gold evaporated surface and 20nm POEGMA polymer brush. Optical absorption measurements of the PED4 assays revealed that antibody uniformity and thickness have a significant effect on the resonance behavior of the plasmonic structure, which can reduce fluorescence enhancement due to the lack of resonance overlap with the fluorophore's absorption and emission wavelengths. Future work will include the use of additives and humidity while printing cAb spots to reduce antibody aggregation (see Chapter 6).

Fluorescence enhancement of a multiplex assay targeted for the simultaneous detection of several cardiac biomarkers could enable the POC testing for the diagnosis and prognosis of heart failure. Specifically, this miniaturized test will could allow patients for self-test their biomarker levels with the use of less expensive and sensitive detectors such as cellphones.

Chapter 6: Future directions

6.1 Introduction

Since the work presented in this dissertation represents the first time the nanopatch antenna metasurface is used for a biosensing purpose, there exists several strategies that can be implemented to further optimize the system. For instance, immobilization of cAb is critical for optimal assay behavior and attachment of SNCs, and a reduction in the assay thickness can bring higher levels of fluorescence enhancement. As discussed in the next section, this can be obtained by optimizing printing conditions of the antibodies as well as introducing humidity in the printing chamber. This chapter will also investigate options to further move the PED4 towards a POCT, such as fabricating a SNC-dAb-fluorophore conjugate that will serve as the reporter in the PED4, as well as developing a mobile device that uses inexpensive components that can potentially replace table-top fluorescence imaging systems. Finally, strategies to move the PED4 for clinical testing will be discussed such as testing the assay with human blood.

6.2 Increasing fluorescence enhancement through antibody immobilization.

6.2.1 Antibody immobilization on POEGMA brushes with different thicknesses

Results in Chapter 3 show that higher enhancements are achieved in smaller POEGMA thicknesses. However, smaller thicknesses make the assay less uniform, which

is attributed to the cAb irregularity on the surface. To study the immobilization of cAb on the POEGMA brush, fluorescently labeled cAbs were printed on 5, 10, 15, and 20 nm POEGMA brushes followed by fluorescence measurements of the cAb spots. The slides were then incubated with FBS for 90 minutes, washed with DI water, and scanned again to determine the reduction in fluorescence post incubation. **Figure 43** shows the percent fluorescence relative to the initial fluorescence intensity for each POEGMA thickness, which is indicative of the amount of antibody immobilized on the surface. From this graph, it is observed that the fluorescence from the 5 nm POEGMA brush is only 8.6% of its initial fluorescence value, as opposed to the thicker brushes which reach 18.6, 14.1, and 29.9% for 10, 15, and 20 nm brushes, respectively. This shows that thinner polymer brushes do not retain antibody as well as thicker brushes and that the 20 nm brush retained the most antibody. Representative SEM images of cAb spots for each POEGMA thickness further validates this observation as it is observed that the antibody is poorly immobilized on the 5 nm brush whereas better uniformity and retention is observed for the 20 nm brush (**Figure 43b**).

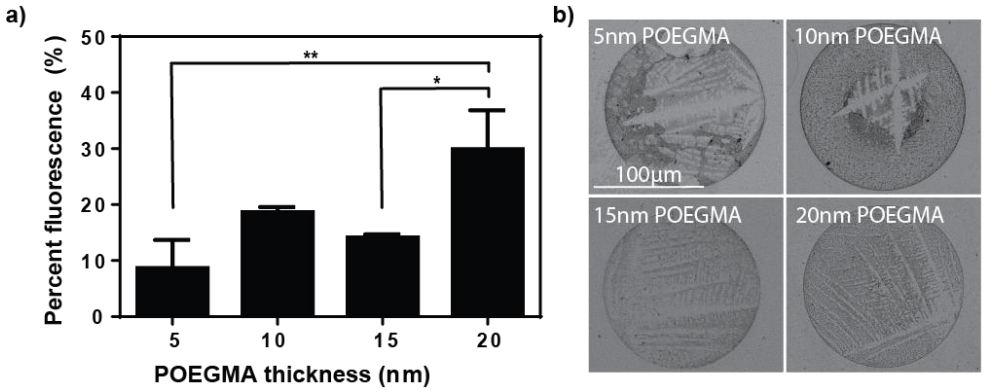

Figure 43: Antibody immobilization on 5, 10, 15, and 20 nm POEGMA brushes. a) Percent fluorescence relative to the initial fluorescence intensity for each POEGMA thickness obtained after incubation in FBS for 90 minutes and washing with DI water. The fluorescence intensity is an indication of the amount of antibody immobilized on the surface. Error bars represent the standard deviation from three slides after averaging 60 cAb spots for each slide. ANOVA analysis shows that the fluorescence intensity for the 20 nm POEGMA brush is statistically significant ($P < 0.05$) compared to the 5 nm and 15 nm POEGMA brushes, providing the highest antibody immobilization and assay performance overall. b) Representative SEM images of cAb spot morphology and antibody immobilization on different thicknesses of POEGMA brushes.

Although the antibody morphology is better as the thickness increases, it would be ideal to maintain a good antibody immobilization in thinner POEGMA brushes for optimal fluorescence enhancement. Furthermore, finding a controllable way to increase antibody morphology can help with antibody aggregation, which increases the average antibody thickness as seen in NT-proBNP and NGAL AFM images (see Chapter 5). For this, we started studying ways to obtain better antibody deposition by looking at parameters such as humidity and additives for printing antibodies, which has been shown to control evaporation [38,119].

6.2.2 Increasing antibody morphology

When performing assays, it has been observed that sport morphology and drying plays an essential role in particle deposition reproducibility. We have been able to obtain excellent spot morphology for BNP such as the one seen in **Figure 44**, where the thickness of the dried antibody is consistent throughout the surface (~10nm) and no antibody aggregation is present, as demonstrated by the SEM images and the AFM images. This also allows to obtain a small surface roughness ($R_q < 5$ nm) , which is beneficial for consistent particle deposition.

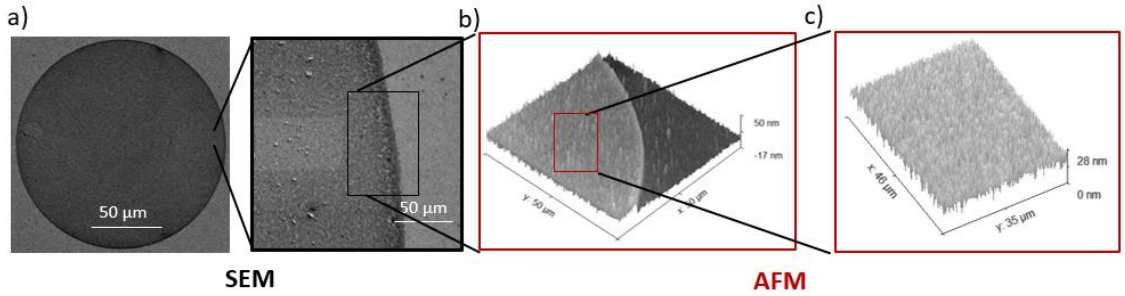

Figure 44: SEM and AFM analysis for ideal BNP cAb spots. a) SEM image of spot to be analyzed in AFM. b) AFM of antibody edge used to determine thickness (50 µm X 50 µm image). c) Smaller AFM image from b).

Figure 45a shows the benefits of obtaining a uniform antibody immobilization. As seen by the SEM image, the nanoparticle deposition is very uniform across the whole surface of the antibody, which brings consistent enhancement throughout all antigen concentrations when performing the PED4 assay. **Figure 45b**, on the other hand, is an example of the effects of nonideal antibody immobilization, which affects the

morphology of the antibody on the surface as seen by the dark aggregates in the SEM image. As a result, silver nanocubes tend to aggregate on the antibody, causing an unequal distribution of the nanocubes on the surface. This results in a decrease in the fluorescence uniformity across the assay as seen in **Fig 45b**, where the enhancement is unequal for all antigen concentrations. For this reason, it is important to develop a protocol where a good drop morphology can reproducibly and consistently be printed.

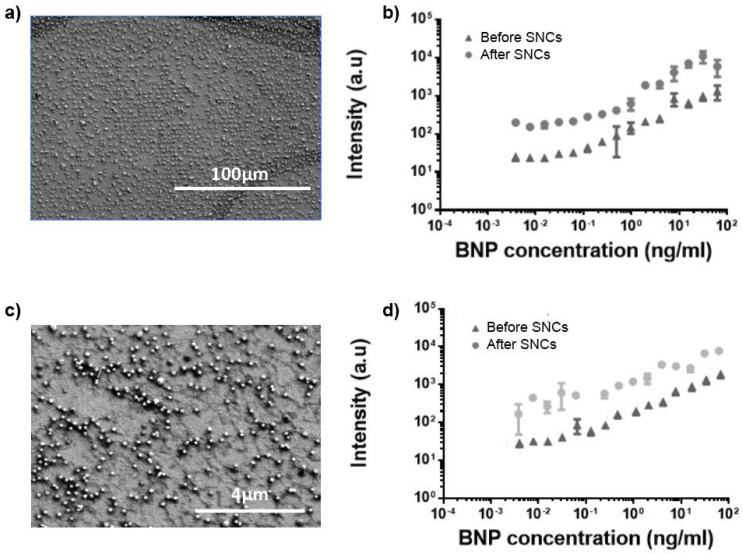

Figure 45: Effects of a good and bad antibody immobilization. a) SEM image of the cAb spots in Figure 48 show excellent particle deposition after silver nanocubes (SNCs) have been placed on the surface. b) Fluorescence measurements for assay spots from a) before (triangles) and after (circles) adding silver nanocubes. Measurements show a good enhancement reproducibility across all antibody concentrations. c) SEM image of an assay where cAbs have aggregated on the surface. d) Fluorescence measurements from c) before (triangles) and after (circles) SNCs are added. The irregular deposition of the antibody on the surface brings non-uniform distribution of the cubes and high variability of the fluorescence enhancement across all concentrations.

It is known that one drawback of using small antibody volumes for spotting is that evaporation can compromise the quality and the reproducibility of the spots and overall assay performance[120]. In our experiments, we have observed that drying of the protein carrier fluid can compromise spot morphology and protein binding to the surface due to the quick crystallization of the carrier fluid or PBS. **Figure 46** shows examples of how drying of NT-proBNP and troponin T capture antibodies can affect the drop morphology. As it can be seen in the "before assay" figures and in their magnifications, PBS crystallization and drying plays an important role in determining the way the antibody binds to the surface and its degree of aggregation. After running the assay, spots where crystallization occurs is seen to create gaps in the antibody immobilization and uneven distribution of the antibody on the surface, as seen by the "after assay" SEM images in **Figure 50**.

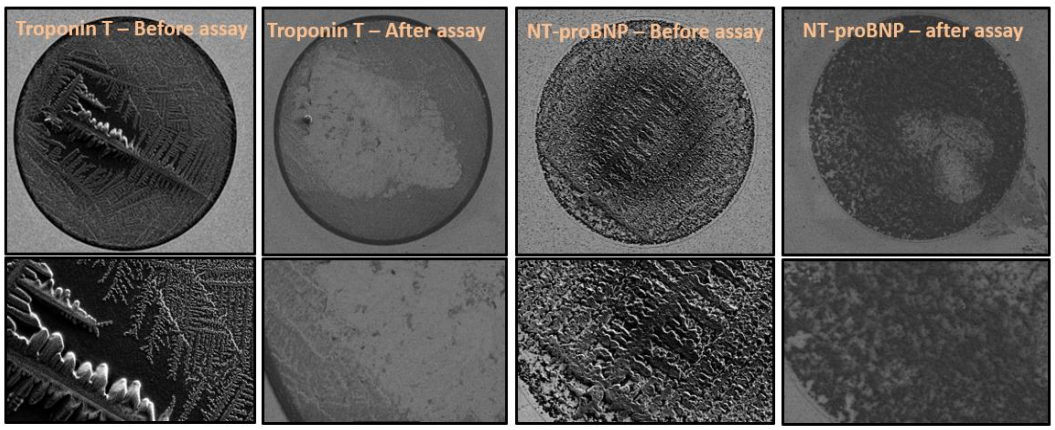

Figure 46: Capture antibody drying for Troponin T and NT-proBNP. Crystallization of antibody excipient (PBS) causes antibody to detach from surface and to aggregate as seen in the "after assay" figures.

In the literature, it has been shown that additives such as glycerol and Tween-20 are good candidates to suppress evaporation and increase the reproducibility of the assays due to their gygroscopic properties to attract and hold moisture[119]. Similarly, the relative humidity in the printing chamber can be increased up to 70% to mitigate evaporation[17]. We tested these parameters to determine the behavior of the antibody morphology and deposition on the POEGMA surface. Specifically, we increased the humidity to 65% added 0.01% Tween-20, 0.1% glycerol, or a combination of both. **Figure 47** shows the behavior of NT-proBNP antibody under these conditions. From this, it is observed that addition of an additive alone did not significantly help with antibody immobilization, drop morphology, or aggregation. We then printed antibodies with the same conditions (with additives) and using 65% humidity. As seen in **Figure 47**, the cAb spots still presented crystallization and aggregation. Antibodies were then printed with the same excipients with 65% humidity and the printed slides were left in high humidity for two hours to slow down the drying process. As observed in the last column of **Figure 74**, the antibody distribution on the surface became much better with this last condition, and the contribution of the different additives became more evident. For the case where no additives were added to the excipient, but the slides were left for two hours in high humidity, the antibody became more compact and uniform. However, aggregation was still present. The best results were obtained when adding 0.01% Tween-20 to the excipient, where a good distribution of the antibody is observed with less aggregation and smaller antibody thickness as seen in the SEM image. Adding 0.1% glycerol also allowed better organization of the antibody, but it did not help with aggregation. Finally,

a combination of 0.1% glycerol and 0.01% Tween-20 was tested, as reported by others[17], giving results that were similar to the 0.01% Tween-20 case. Future work consists in studying the behavior of other additives and printing buffers, as well as their effect on particle distribution and fluorescence enhancement, on smaller POEGMA brushes. Other parameters will also be tested such as cAb concentration and spot diameter to obtain thin antibody immobilization on the surface.

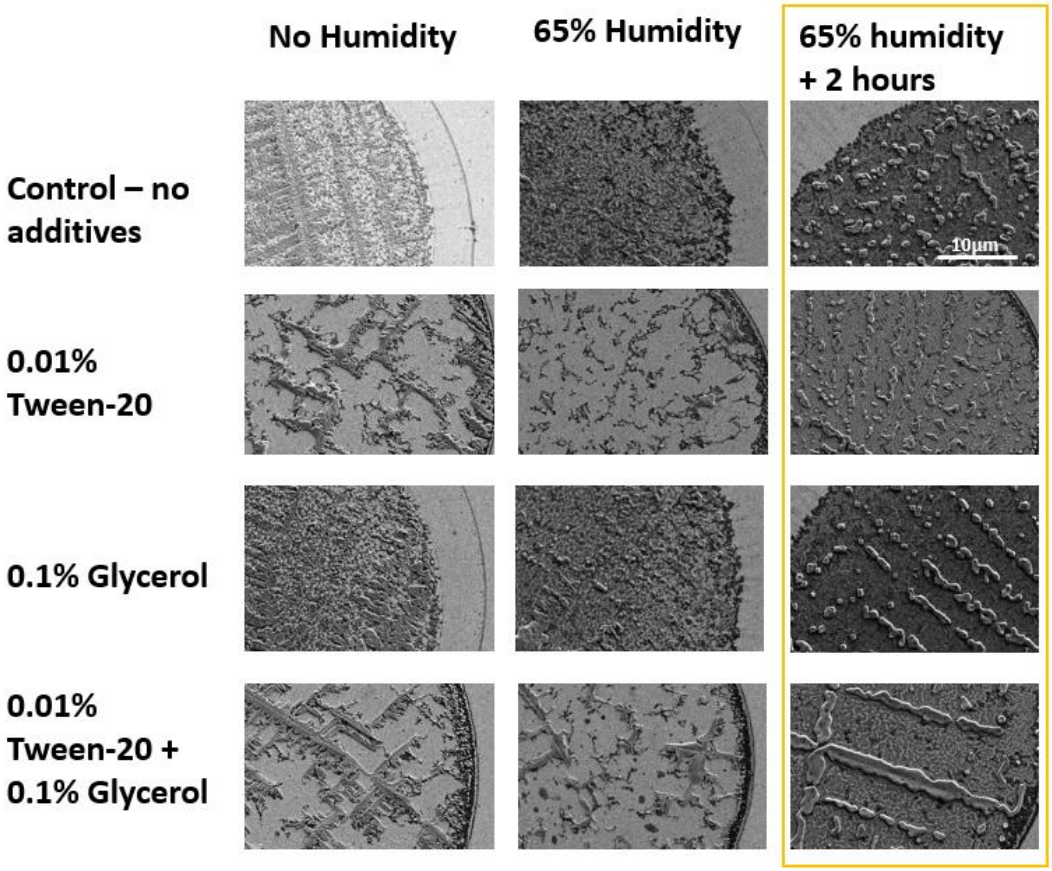

Figure 47: Effect of additives and humidity on cAb drop morphology. SEM images allow us to directly observe the behavior of antibodies on the POEGMA surface under different conditions. Best results are obtained when printing antibodies under 65% humidity and by leaving slides under high humidity for 2-hours. Addition of 0.01% Tween-20 improved antibody distribution and aggregation.

6.3 Synthesis of SNC-dAb-Alexa647 conjugate reagent.

To date, we have shown that a plasmonic cavity can be created by adding a final step where a third Ab (termed sAb; see **Figure 19** in Chapter 4) that is conjugated to a SNC can be introduced into the assay as the final incubation step. The sAb-SNC conjugate binds to the dAb in the microarray spots and creates a plasmonic cavity that leads to a ~13x fluorescence enhancement but also lowers the LOD by ~8x. However, this approach is not fully compatible with a point-of-care test format as it requires an additional incubation step. To eliminate this step and simplify the assay, we will synthesize a new plasmonic conjugate, where the dAbs will be conjugated to a SNC and to a fluorophore to create the plasmonic cavity in a single step **Figure 48**. To complete this goal, we will attach the dAb's to SNCs by replacing the nanoparticle's capping agent with a carboxy-PEG-thiol group. Next, the carboxylic acid will be activated for NHS-ester chemistry to target the free amines in the dAb scaffold. AlexaFluor 647 will next be conjugated to the SNC-dAb complex by targeting the remaining free amines in the Ab scaffold. This last reaction will be followed by the inactivation of unconjugated free dye, with high molarity Tris buffer and centrifugation to purify the SNC-dAb-Alexa647 plasmonic conjugate. This new conjugate reagent mixed with trehalose will then be printed on the surface of POEGMA in the same fashion dAbs were printed surrounding the cAbs (**Figure 48b**), serving as the reporter in our system.

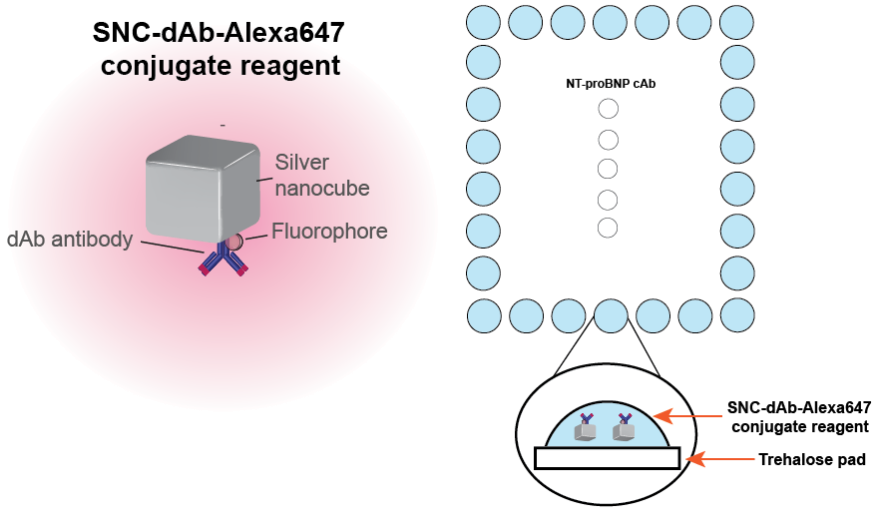

Figure 48: Schematic of conjugate reagent composed detection antibody directly attached to SNC and fluorophore attached to detection antibody. This reagent will be printed on trehalose pads and will serve as the fluorescence reporter.

In order to have a better control of the size and functionalization of our SNC-dAb-Alexa647 conjugate reagent (CR), we started in-house synthesis of the SNCs in our laboratory (**Figure 49**). This will allow us to easily tune parameters such as length of capping agent, antibody surface density on the SNC, and particle edge length. For this, silver nanocubes were fabricated using polyol synthesis [121,122]. Briefly, 1.3 mM solution of hydrosulfide (NaSH), 20 mg/mL of poly-vinylpyrrolidone (PVP), and 3 mM of hydrochloric acid (HCl) solution were first prepared separately in Ethylene Glycol (EG) as the solvent. A solution of trifluoroacetate ($AgC_2F_3O_2$) was also prepared by dissolving 0.1 g in 0.8 mL of EG. A heating bath was prepared by placing a Pyrex container with silicone fluid on top of a stirring hotplate at 150 °C and with a steering speed of 260 rpm. A round-bottom flask (RBF) containing 5 mL of EG and a small magnetic stirring bar

was dipped into the heating bath. Then 60 µL of NaSH was placed into the RBF and let to incubate for 2 minutes. 500 µL of the HCl solution and 1.25 mL of the PVP solution were put into the RBF for 2 more minutes. Finally, 400 µL of $AgC_2F_3O_2$ was placed in the RBF. After 2.5 hrs. the RBF was raised from the oil bath and the cap was removed. After letting the RBF to cool off for 20 minutes, 5 mL of acetone was placed into the RBF and vortexed. A pipette was then used to transfer the solution to 1.5 mL Eppendorf tubes. These were centrifuged at a speed of 5150x g for 5 minutes and the supernatant was removed. The particles were then washed with DI water two times before resuspending in DI water. **Figure 49b** shows SEM images of the in-house synthesized nanocubes, showing high monodispersity (75nm ± 6.3 nm) and stability.

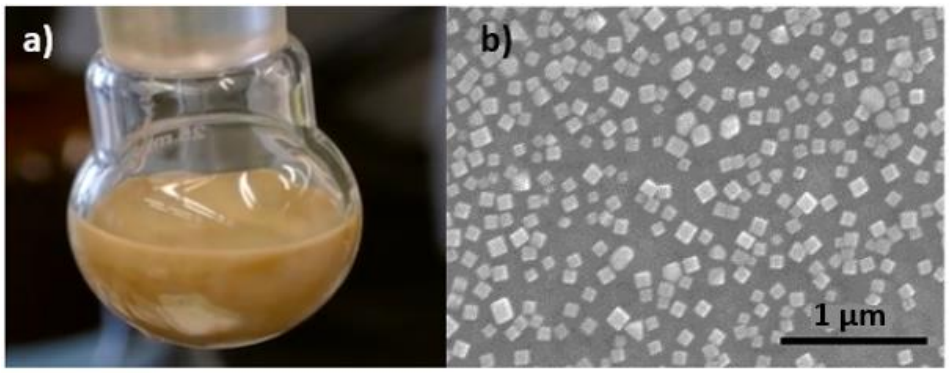

Figure 49: In-house particle synthesis of 75 nm SNCs using polyol synthesis. a) shows a photograph of particle solution after 2.5 hrs. of reagent mixing. b) SEM image of 75nm cubes after washing.

The particles were then functionalized by first replacing the PVP layer surrounding the nanoparticle with the thiol PEG acid SH-PEG-COOH followed by

protein conjugation through EDC/NHS crosslinking of carboxylates with primary amines. **Figure 50** shows a schematic of the steps taken to substitute the capping agent in the SNCs with a protein. **Figure 51** shows UV-absorption measurements taken when replacing the PVP coating with SH-PEG-COOH (blue line). We can identify when the molecule is being replaced by looking at a small shift in the nanoparticle resonance. Broadening of the absorption peak also helped us determine the thiol PEG acid concentrations at which particles started to aggregate. After replacing the PVP, the particles were conjugated with the protein model BA (green line). We chose this protein to create a general protocol for protein conjugation due to its availability and transability. Further tests need to be done to optimize protein conjugation on the nanocubes. Some of the parameters that will be considered are the molar ratio of the HS-PEG-COOH and mPEG-SH, as many groups have reported better particle stability and protein binding performance when these two molecules are used[123–125].

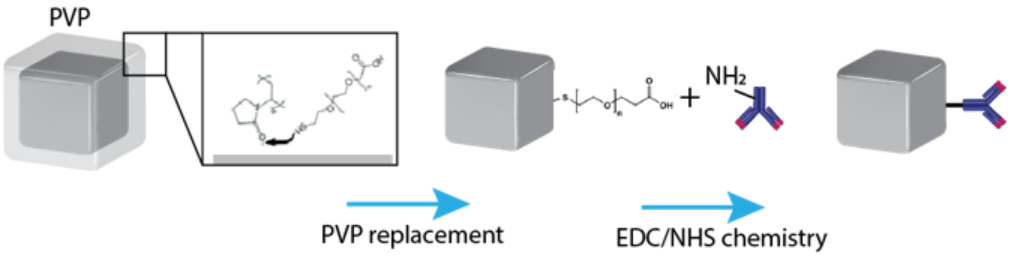

Figure 50: Replacement of PVP with SH-PEG-COOH and protein conjugation through EDC/NHS crosslinking of carboxylates with protein's primary amines.

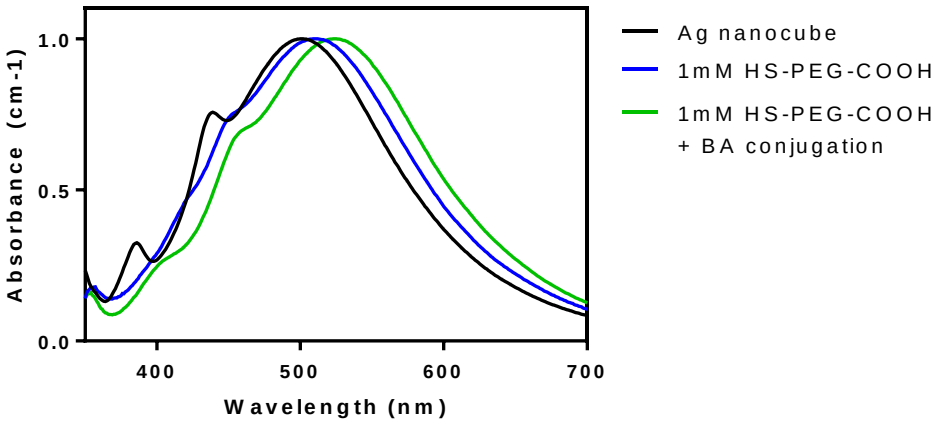

Figure 51: UV-vis measurements shows that PVP in SNCs have been replaced by HS-PEG-COOH due to the shift in the particle resonance. A further shift was observed when performing EDC/NHS chemistry to conjugate BSA protein to the nanoparticle.

This study shows that SNCs can reproducibly be synthesized in our laboratory and their capping agent can be replaced to attach proteins of our choice through EDC/NHS chemistry. In the future, BNP dAbs will be attached to the nanocubes and they will be tested in a D4 assay on a performed on a gold substrate to determine the binding of the nanocubes through cAb and dAb interaction. After this, fluorophores will be attached to the free amines in the SNCs and the fluorescence enhancement will be compared to that of initial results with a secondary antibody as described in Section 4.3.

6.4 Using handheld-based detector for PED4 testing

In order to detect fluorescence from the PED4 using a small and inexpensive detector, the fluorescence system demonstrated in Section 4.3 will be modified and compressed into a handheld format. To do this, the beam splitter could be replaced with a less inexpensive dichroic mirror, which will be used to direct the incident light at a 90º towards the substrate while simultaneously serve as a filter to select the fluorophore's emission wavelength. Another option will be to modify the set up so that it the laser illuminates the gold substrate in an angle instead of front incidence, which will allow us to eliminate the use of a beam splitter. In addition, the microscope objective can be replaced by a much cheaper plastic aspheric lens, and the lens placed before the CCD webcamera can replaced by the lens that is already incorporated in small cameras. Although Section 4.3 uses a laser diode with a well characterized spot shape and collimation, less costly options of laser diodes are available that can go as low as $5 (Digi-Key Part 1528-1391-ND, for 5mW laser power). The detector camera and the computer needed to run the data analysis software can be replaced with the ubiquitous cellphone. With these changes in mind the total cost for the detector could drop from $800 (as in the case of detector used in Section 4.3) to less than $150. Once the mobile phone detector is optimized, we will compare our results on gold and glass slides to those obtained in the commercial microarray scanner. It is expected that the PED4-POCT scanned by the phone detector will have similar or better performance than that of the regular D4 glass slide using the high-priced scanner.

6.5 Other design considerations – modifying components in platform to increase fluorescence

Changing particle concentration: Increasing the nanocube fill fraction increases the resonance strength at a particular wavelength, which is seen by a higher absorption in the spectrum as the particle density increases. Specifically, the highest packing density that can be achieved is 20% fill fraction, giving 99.7% absorption[77]. Increasing the fill fraction leads to higher fluorescence enhancement because of the higher absorption of light and the higher probability of fluorophores to interact with the edges and corners of the nanocubes, where the field and excitation enhancement are the largest.

Changing particle size and gap thickness**:** As previously mentioned, a remarkable aspect about this plasmonic architecture is the ability to modulate the plasmon resonance from the visible to near infrared side of the spectrum by simply modifying the particle size or the gap thickness. This ability to change the plasmon resonance is beneficial for fluorescence enhancement since by overlapping the plasmon resonance with the excitation or emission spectrum of the fluorophore we can obtain larger enhancement factors. It has been seen that while keeping the gap size fixed and changing the particle size, nanopatches providing the largest enhancement had resonances close to the excitation wavelength, due to enhanced absorption in the embedded fluorophores[55]. In future studies we will investigate the use of different particle sizes and their effect on plasmonic resonance as well as fluorescence enhancement. To do this, we will determine the conditions necessary to obtain similar fill fractions between the different particle sizes such as incubation time and concentration.

Fluorophore selection: There are several characteristics in a fluorophore that need to be considered for maximum sensitivity and fluorescence enhancement. First of all, the fluorophore used needs to be a probe with high fluorescence quantum yield and high photostability to allow detection of low concentrations with greater sensitivity. Also, since it is planned to test the platform with blood, the fluorophore of choice will ideally have a far-red location in the spectrum to avoid the excitation of spectral features of strongly absorbing naturally occurring biological chromophores such as hemoglobin, which can lead improved sensitivity to target analyte. Furthermore, the spectral location of its excitation and emission (but most importantly its excitation) profile must be in the range where the nanopatch antenna resonates, which for our system is located between the 400-900nm wavelength region. Ideally, the fluorophore's absorption maximum should coincide with the nanopatch resonance absorption maximum.

6.6 Assay validation of the PED4 in a clinical setting

We will use the final detector prototype and chip design to create dose-response curves in FBS, whole chicken blood (WCB), and human serum (HS). Once we have assessed the figures of merit (such as LOD and dynamic range) for each target analyte in the different complex fluids, we will test our diagnostic system with archival samples available through the Duke Medical Center. These samples of known cardiac patients with distinct levels of the target biomarkers will be tested with the PED4-POCT and commercially available gold standard ELISAs. To test the blood sample using the PED4, 80 µl of blood will be placed in one of the chambers of the microfluidic chip followed by the addition of washing buffer on the secondary chamber. After the PED4 has been

washed with the buffer, it will be imaged in the handheld detector to determine the analyte concentration based on the fluorescence values. It is important to point out that preprocessing is not needed when testing the PED4 and it can be directly tested with undiluted whole blood due to the non-fouling nature of the POEGMA surface, as it was demonstrated in previous clinical studies involving Leptin testing[9]. In the case of ELISA testing, blood sample will be centrifuged, and the resulting serum will be aliquoted into cryovials and stored at -80 ^{o}C until needed. For ELISA testing, 100x dilution with assay diluent buffer is usually required for all specimens. We anticipate that our measure with the PED4 will be able to reach an interclass correlation value of >0.8 with confidence interval bounds of approximately ±0.1 when compared to the ELISA results. The primary goal of the clinical validation study will be to evaluate the PED4 in a spectrum of relevant patients with cardiovascular disease, where testing of the candidate markers would typically be indicated in clinical practice. We will evaluate the accuracy and precision of the PED4 with relevant cardiac conditions (e.g, chest pain, myocardial infarction, heart failure, or need for cardiovascular risk assessment) who are being treated in either the inpatient or ambulatory setting at Duke University Hospital (DUH).

Clinical Setting and Study Procedures: In order to validate the PED4 across the relevant clinical values, we will plan to enroll patients in a broad diagnostic category where these biomarkers play a central role in medical decision making. This includes patients with acute chest pain or myocardial infarction, patients with acute or chronic heart failure, and patients for acute coronary syndromes. We will include a representative mix of patients in terms of age, sex, race, and ethnicity. Enrolled patients will have

venous phlebotomy performed by appropriately trained personnel and samples sent to the Duke Clinical laboratory for measurement of the 3 biomarkers of interest (NT-proBNP, galectin-3, and NGAL) using commercially available ELISA tests. Whole blood from the same venipuncture will be used for simultaneous testing of the POCT prototype. Trained research personnel will perform the POC analysis and data will be collected and recorded in an appropriate research database and stored for analysis. Results of laboratory testing will not be shared with study participants unless performed for clinical indications.

6.7 Conclusion

In this chapter we explored optimization techniques that can be used to further increase the PED4 assay performance and enhancement. It was demonstrated that the POEGMA thickness plays a role in cAb retention and immobilization, where thinner brushes (5, 10 nm) retain less antibody than thicker (20nm) brushes. This irregular immobilization of the antibody in thinner brushes reduces reproducibility between assays and decreases their performance. To further explore way in which antibody immobilization can be enhanced, cAb printing conditions were optimized by changing printing parameters. It was demonstrated that the evaporation rate of cAb spots can be decreased with the use of humidity when printing the antibodies, and that adding 0.01% of Tween-20 to the excipient can reduce aggregation and increase the antibody distribution on the POEGMA surface. Future work consists in changing printing conditions on smaller POEGMA brushes and testing other parameters such as cAb concentration and spot diameter to obtain thin antibody immobilization on the surface. This chapter also presented preliminary work on the synthesis of a reporter consisting of

fluorescently labeled dAbs attached to SNCs. This reporter will allow us to further move the system towards a POCT where the extra SNC incubation step will no longer be needed. Preliminary work shows that we can synthesize SNCs in-house and proteins can be attached to their surface through EDC/NHS crosslinking. Finally, future work will consist of building a cellphone-based detector that can be used with the PED4.

Chapter 7 Conclusion

This dissertation has explored the integration of the nanopatch antenna metasurface as a plasmonic biosensor for the fluorescence enhancement of planar immunoassays, and it has further explored its use as a POCT for the detection of cardiac biomarkers used in the prognosis of heart failure. The bottom-up, and scalable fabrication approach used here simply consists of attaching high density (~12% fill fraction) of SNCs on the surface of the ran immunoassay. In Chapter 3, we demonstrated that fluorescence enhancement values of over 100-fold can be achieved by depositing SNCs through a PAH layer (positively charged polyelectrolyte) and that an LOD enhancement of 14-fold can be achieved when using low photomultiplier sensitivities (or low PMT gain). This serves an indication that the PED4 can be used to compensate for the loss in sensitivity in less sensitive detectors such as mobile devices, a concept that was further explored in Chapter 4. We also studied the plasmonic behavior of the PED4 where it was shown that decreasing the POEGMA thickness (and thus the gap between the gold surface and the SNCs) increases the plasmonic enhancement obtained. In addition, this decrease in thickness causes a shift in resonance in the plasmonic structure, which has been observed in previous studies.

The use of the PED4 as a POCT was studied in Chapter 4, where it was demonstrated that the extra incubation of the PAH layer can be eliminated by conjugating SNCs with a secondary antibody that attaches directly to the Fc region of the detection antibody in the assay. Doing so was beneficial in two ways: 1) the number of steps were reduced to achieved fluorescence enhancement, and 2) since the number of SNCs on the

surface are now dependent on the dAb concentration, the SNC associated noise was reduced at low BNP concentrations, enhancing the LOD performance by ~8-fold even at high PMT gains. In addition, to further demonstrate the value of the PED4 as a POCT, it was shown that the plasmonic assay can be detected with inexpensive components, whereas the unenhanced assay could not be detected. A microfluidic chip was also fabricated on a silicon wafer using photolithography and reactive ion etching to run the PED4 with minimal user interference. This prototype that was able to generate a dose-response curve with fluorescence intensity values corresponding to normal incubation. Although only a 2-fold enhancement was obtained due to particle aggregation and drying when flowing the SNCs, future work will explore ways in which the incubation chamber can be designed to avoid this problem.

One of the main promises of the PED4 assay is its utility as a POCT that can be used outside the clinic or hospital. Having an immunoassay that can be tested in a microfluidic chip and with a mobile detector can significantly decrease the need of human interface. Hence, allowing for fast clinical use or even for self-testing. The health sector can benefit from such a device for the diagnosis and prognosis of heart disease and specifically for heart failure, as it remains the number one cause of the death in the U.S. Reducing the number of unnecessary visits to the clinic or rehospitalization can increase risk stratification of the disease and decrease the economic burden that it brings, which lies in the billions of dollars per year. Assessment of multiple cardiac biomarkers have been shown to increase the diagnostic and prognostic value of the disease, and provide

added value to medical management, which could potentially lower risk of mortality, readmissions, and related costs.

In Chapter 5, it was demonstrated that fluorescence from the detection of multiple biomarkers could simultaneously be enhanced with the PED4. For this, various biomarkers were assessed in a monoplex, duplex, and multiplex format to test for cross-reactivity in the D4 assay. It was concluded that the biomarkers for NT-proBNP, Galectin-3, and NGAL can simultaneously be tested together without cross-reactivity issues. CRP was also tested, but the dynamic range needed for this biomarker was not compatible with the D4 assay. Troponin biomarkers such as cTnI and cTnT cross-reacted with the carrier fluid FBS, but we believe that this can be avoided by using other carrier fluids such as troponin depleted serum. After translating the multiplex assay into the PED4, we observed a 17-fold enhancement in NGAL, 15-fold in NT-proBNP, and 13-fold in Galectin-3. The placement of different types of cAbs on the same POEGMA surface also allowed us to gain better understanding of the importance of antibody immobilization. Specifically, it was observed through SEM and AFM images that Galectin-3 antibody had the best immobilization, and as a result it provided with the most ideal plasmonic resonance. This further encouraged us to investigate better antibody immobilization strategies such as addition of additives and humidity, as it is described in Chapter 6. Where it has been shown that printing antibodies under high humidity and adding 0.01% Tween-20 can reduce antibody aggregation and increase its uniformity on the surface.

Further work will also consist in translating the PED4 assay into a single step POCT where a detection conjugate reagent will be synthesized. This will consist of a SNC directly conjugated to a detection antibody and a fluorophore, which will allow us to reduce the number of antibodies needed to run the PED4 as well as the number of steps.

References

1. Ohba, Y., Fujioka, Y., Nakada, S. & Tsuda, M. *Fluorescent protein-based biosensors and their clinical applications*. *Progress in Molecular Biology and Translational Science* **113,** (Elsevier Inc., 2013).

2. Darwish, I. A. Immunoassay Methods and their Applications in Pharmaceutical Analysis: Basic Methodology and Recent Advances. *Int. J. Biomed. Sci.* **2,** 217–35 (2006).

3. Chen, Z., Dodig-Crnković, T., Schwenk, J. M. & Tao, S. C. Current applications of antibody microarrays. *Clin. Proteomics* **15,** 1–15 (2018).

4. Sauer, U. Analytical protein microarrays: Advancements towards clinical applications. *Sensors (Switzerland)* **17,** (2017).

5. Walter, J. G. *et al.* Protein microarrays: Reduced autofluorescence and improved LOD. *Eng. Life Sci.* **10,** 103–108 (2010).

6. Nath, N. *et al.* Improving protein array performance: Focus on washing and storage conditions. *J. Proteome Res.* **7,** 4475–4482 (2008).

7. Buchegger, P., Sauer, U., Toth-Székély, H. & Preininger, C. Miniaturized protein microarray with internal calibration as point-of-care device for diagnosis of neonatal sepsis. *Sensors* **12,** 1494–1508 (2012).

8. Kemmler, M. *et al.* Compact point-of-care system for clinical diagnostics. *Sensors Actuators, B Chem.* **139,** 44–51 (2009).

9. Joh, D. Y. *et al.* Inkjet-printed point-of-care immunoassay on a nanoscale polymer brush enables subpicomolar detection of analytes in blood. *Proc. Natl. Acad. Sci.* 201703200 (2017). doi:10.1073/pnas.1703200114

10. Hill, R. T. Plasmonic biosensors. *Wiley Interdisciplinary Reviews: Nanomedicine and Nanobiotechnology* **7,** 152–168 (2015).

11. Giannini, V., Fernández-Domínguez, A. I., Heck, S. C. & Maier, S. A. Plasmonic nanoantennas: Fundamentals and their use in controlling the radiative properties of nanoemitters. *Chemical Reviews* **111,** 3888–3912 (2011).

12. Baumberg, J. J., Aizpurua, J., Mikkelsen, M. H. & Smith, D. R. Extreme nanophotonics from ultrathin metallic gaps. *Nat. Mater.* **18,** 668–678 (2019).

13. Kinkhabwala, A. *et al.* Large single-molecule fluorescence enhancements produced by a bowtie nanoantenna. *Nat. Photonics* **3,** 654–657 (2009).

14. Yesilkoy, F. *et al.* Phase-sensitive plasmonic biosensor using a portable and large field-of-view interferometric microarray imager. *Light Sci. Appl.* **7,** 17152 (2018).

15. Zeng, S. *et al.* Graphene-Gold Metasurface Architectures for Ultrasensitive Plasmonic Biosensing. *Adv. Mater.* **27,** 6163–6169 (2015).

16. Zhou, L. *et al.* Enhancement of immunoassay's fluorescence and detection sensitivity using three-dimensional plasmonic nano-antenna-dots array. *Anal. Chem.* **84,** 4489–4495 (2012).

17. Tabakman, S. M. *et al.* Plasmonic substrates for multiplexed protein microarrays with femtomolar sensitivity and broad dynamic range. *Nat. Commun.* **2,** (2011).

18. Luan, J. *et al.* Add-on plasmonic patch as a universal fluorescence enhancer. *Light Sci. Appl.* **7,** (2018).

19. Chen, S., Li, L., Zhao, C. & Zheng, J. Surface hydration: Principles and applications toward low-fouling/nonfouling biomaterials. *Polymer (Guildf).* **51,** 5283–5293 (2010).

20. Bridges, A. W. & García, A. J. Anti-inflammatory polymeric coatings for implantable biomaterials and devices. *J. Diabetes Sci. Technol.* **2,** 984–994 (2008).

21. Krishnan, S., Weinman, C. J. & Ober, C. K. Advances in polymers for anti-biofouling surfaces. *J. Mater. Chem.* **18,** 3405–3413 (2008).

22. Liu, Q., Singh, A. & Liu, L. Amino acid-based zwitterionic poly(serine methacrylate) as an antifouling material. *Biomacromolecules* **14,** 226–231 (2013).

23. Hoa, X. D., Kirk, A. G. & Tabrizian, M. Towards integrated and sensitive surface plasmon resonance biosensors: A review of recent progress. *Biosens. Bioelectron.* **23,** 151–160 (2007).

24. Prime, K. L. & Whitesides, G. M. Adsorption of Proteins onto Surfaces Containing End-Attached Oligo(ethylene oxide): A Model System Using Self-Assembled Monolayers. *J. Am. Chem. Soc.* **115,** 10714–10721 (1993).

25. Zheng, J. *et al.* Strong repulsive forces between protein and oligo (ethylene glycol) self-assembled monolayers: A molecular simulation study. *Biophys. J.* **89,** 158–166 (2005).

26. Kim, Y. & Bard, A. J. Imaging and Etching of Self-Assembled n-Octadecanethiol

Layers on Gold with the Scanning Tunneling Microscope. *Langmuir* **8,** 1096–1102 (1992).

27. Mrksich, M., Dike, L. E., Tien, J., Ingber, D. E. & Whitesides, G. M. Using microcontact printing to pattern the attachment of mammalian cells to self-assembled monolayers of alkanethiolates on transparent films of gold and silver. *Exp. Cell Res.* **235,** 305–313 (1997).

28. Jeon, S. I., Lee, J. H., Andrade, J. D. & De Gennes, P. G. Protein-surface interactions in the presence of polyethylene oxide. I. Simplified theory. *J. Colloid Interface Sci.* **142,** 149–158 (1991).

29. Suginome, H. & Uchida, T. Part II. *J. Chem. Soc. Perkin Trans. 1* **142,** 943 (1980).

30. Ma, B. H., Hyun, J. & Stiller, P. Functionalized Polymer Brushes Synthesized by Surface-Initiated Atom Transfer Radical Polymerization **. 338–341 (2004). doi:10.1002/adma.200305830

31. Ma, H., Li, D., Sheng, X., Zhao, B. & Chilkoti, A. Protein-resistant polymer coatings on silicon oxide by surface-initiated atom transfer radical polymerization. *Langmuir* **22,** 3751–3756 (2006).

32. Ma, H., Wells, M., Beebe, T. P. & Chilkoti, A. Surface-initiated atom transfer radical polymerization of oligo(ethylene glycol) methyl methacrylate from a mixed self-assembled monolayer on gold. *Adv. Funct. Mater.* **16,** 640–648 (2006).

33. Hucknall, A. *et al.* Simple fabrication of antibody microarrays on nonfouling polymer brushes with femtomolar sensitivity for protein analytes in serum and blood. *Adv. Mater.* **21,** 1968–1971 (2009).

34. Liotta, L. A. *et al.* Protein microarrays: Meeting analytical challenges for clinical applications. *Cancer Cell* **3,** 317–325 (2003).

35. Preininger, C. & Sauer, U. Quality control of chip manufacture and chip analysis using epoxy-chips as a model. *Sensors Actuators, B Chem.* **90,** 98–103 (2003).

36. Sauer, U., Preininger, C. & Hany-Schmatzberger, R. Quick and simple: Quality control of microarray data. *Bioinformatics* **21,** 1572–1578 (2005).

37. Andrew St John, C. P. Existing and Emerging Technologies for Point-of-Care Testing. *Clin. Biochem. Rev.* **10,** 133–139 (2014).

38. Wei, Q. *et al.* Protein interactions with polymer coatings and biomaterials. *Angew. Chemie - Int. Ed.* **53,** 8004–8031 (2014).

39. Chau, Y. F. & Yeh, H. H. A comparative study of solid-silver and silver-shell nanodimers on surface plasmon resonances. *J. Nanoparticle Res.* **13,** 637–644 (2011).

40. Kelly, K. L., Coronado, E., Zhao, L. L. & Schatz, G. C. The optical properties of metal nanoparticles: The influence of size, shape, and dielectric environment. *J. Phys. Chem. B* **107,** 668–677 (2003).

41. Hecht, B. & Novotny, L. *Principles of Nano-Optics*. (Cambridge University Press, 2012).

42. Homola, J. Present and future of surface plasmon resonance biosensors. *Anal. Bioanal. Chem.* **377,** 528–539 (2003).

43. Brolo, A. Plasmonics for future biosensors. *Nat. Photonics* **123,** 1986–1993 (2012).

44. Anker, J. N. *et al.* Biosensing with plasmonic nanosensors. *Nanosci. Technol. A Collect. Rev. from Nat. Journals* **7,** 308–319 (2009).

45. Han, X., Liu, K. & Sun, C. Plasmonics for biosensing. *Materials (Basel).* **12,** (2019).

46. McFarland, A. D. & Van Duyne, R. P. Single silver nanoparticles as real-time optical sensors with zeptomole sensitivity. *Nano Lett.* **3,** 1057–1062 (2003).

47. Mock, J. J., Smith, D. R. & Schultz, S. Local refractive index dependence of plasmon resonance spectra from individual nanoparticles. *Nano Lett.* **3,** 485–491 (2003).

48. Mustafaoglu, N., Kiziltepe, T. & Bilgicer, B. Site-specific conjugation of an antibody on a gold nanoparticle surface for one-step diagnosis of prostate specific antigen with dynamic light scattering. *Nanoscale* **9,** 8684–8694 (2017).

49. Hammond, J. L., Bhalla, N., Rafiee, S. D. & Estrela, P. Localized surface plasmon resonance as a biosensing platform for developing countries. *Biosensors* **4,** 172–188 (2014).

50. Jatschka, J., Dathe, A., Csáki, A., Fritzsche, W. & Stranik, O. Propagating and localized surface plasmon resonance sensing - A critical comparison based on measurements and theory. *Sens. Bio-Sensing Res.* **7,** 62–70 (2016).

51. Mock, J. J. *et al.* Distance-dependent plasmon resonant coupling between a gold nanoparticle and gold film. *Nano Lett.* **8,** 2245–2252 (2008).

52. Hill, R. T. *et al.* Plasmon ruler with angstrom length resolution. *ACS Nano* **6,** 9237–9246 (2012).

53. Ciracì, C. *et al.* Probing the ultimate limits of plasmonic enhancement. *Science (80-.).* **337,** 1072–1074 (2012).

54. Moreau, A. *et al.* Controlled-reflectance surfaces with film-coupled colloidal nanoantennas. *Nature* **492,** 86–89 (2012).

55. Rose, A. *et al.* Control of radiative processes using tunable plasmonic nanopatch antennas. *Nano Lett.* **14,** 4797–4802 (2014).

56. Bauch, M., Toma, K., Toma, M., Zhang, Q. & Dostalek, J. Plasmon-Enhanced Fluorescence Biosensors: A Review. *Plasmonics* **9,** 781–799 (2014).

57. Fan, J. A. *et al.* Self-assembled plasmonic nanoparticle clusters. *Opt. InfoBase Conf. Pap.* **328,** 1135–1139 (2010).

58. Gill, R. *et al.* Silver nanoparticle aggregates as highly efficient plasmonic antennas for fluorescence enhancement. *J. Phys. Chem. C* **116,** 16687–16693 (2012).

59. Bharadwaj, P. & Novotny, L. Spectral dependence of single molecule fluorescence enhancement. *Opt. Express* **15,** 14266 (2007).

60. Neumann, B. T., Johansson, M., Kambhampati, D. & Knoll, W. Surface ± Plasmon Fluorescence Spectroscopy **. **31658,** 575–586 (2002).

61. Attridge, J. W., Daniels, P. B., Deacon, J. K., Robinson, G. A. & Davidson, G. P. Sensitivity enhancement of optical immunosensors by the use of a surface plasmon resonance fluoroimmunoassay. *Biosens. Bioelectron.* **6,** 201–214 (1991).

62. Huang, C. J., Dostalek, J. & Knoll, W. Optimization of layer structure supporting long range surface plasmons for surface plasmon-enhanced fluorescence spectroscopy biosensors. *J. Vac. Sci. Technol. B Microelectron. Nanom. Struct.* **28,** 66–72 (2010).

63. Dostálek, J., Kasry, A. & Knoll, W. Long range surface plasmons for observation of biomolecular binding events at metallic surfaces. *Plasmonics* **2,** 97–106 (2007).

64. Matveeva, E. G., Gryczynski, Z. & Lakowicz, J. R. Myoglobin immunoassay based on metal particle-enhanced fluorescence. *J. Immunol. Methods* **302,** 26–35 (2005).

65. Touahir, L. *et al.* Localized surface plasmon-enhanced fluorescence spectroscopy for highly-sensitive real-time detection of DNA hybridization. *Biosens.*

Bioelectron. **25,** 2579–2585 (2010).

66. Punj, D. *et al.* A plasmonic ‘antenna-in-box’ platform for enhanced single-molecule analysis at micromolar concentrations. *Nat. Nanotechnol.* **8,** 512–516 (2013).

67. Zhang, W. *et al.* Giant and uniform fluorescence enhancement over large areas using plasmonic nanodots in 3D resonant cavity nanoantenna by nanoimprinting. *Nanotechnology* **23,** (2012).

68. Brolo, A. G. *et al.* Enhanced fluorescence from arrays of nanoholes in a gold film. *J. Am. Chem. Soc.* **127,** 14936–14941 (2005).

69. Akselrod, G. M. *et al.* Probing the mechanisms of large Purcell enhancement in plasmonic nanoantennas. *Nat. Photonics* **8,** 835–840 (2014).

70. Akselrod, G. M. *et al.* Efficient Nanosecond Photoluminescence from Infrared PbS Quantum Dots Coupled to Plasmonic Nanoantennas. *ACS Photonics* **3,** 1741–1746 (2016).

71. Akselrod, G. M. *et al.* Leveraging nanocavity harmonics for control of optical processes in 2d semiconductors. *Nano Lett.* **15,** 3578–3584 (2015).

72. Huang, J., Traverso, A. J., Yang, G. & Mikkelsen, M. H. Real-Time Tunable Strong Coupling: From Individual Nanocavities to Metasurfaces. *ACS Photonics* **6,** 838–843 (2019).

73. Huang, J., Akselrod, G. M., Ming, T., Kong, J. & Mikkelsen, M. H. Tailored Emission Spectrum of 2D Semiconductors Using Plasmonic Nanocavities. *ACS Photonics* **5,** 552–558 (2018).

74. Hoang, T. B., Akselrod, G. M. & Mikkelsen, M. H. Ultrafast Room-Temperature Single Photon Emission from Quantum Dots Coupled to Plasmonic Nanocavities. *Nano Lett.* **16,** 270–275 (2016).

75. Hoang, T. B. *et al.* Ultrafast spontaneous emission source using plasmonic nanoantennas. *Nat. Commun.* **6,** 1–7 (2015).

76. Lassiter, J. B. *et al.* Plasmonic waveguide modes of film-coupled metallic nanocubes. *Nano Lett.* **13,** 5866–5872 (2013).

77. Akselrod, G. M. *et al.* Large-Area Metasurface Perfect Absorbers from Visible to Near-Infrared. *Adv. Mater.* **27,** 8028–8034 (2015).

78. Stewart, J. W., Akselrod, G. M., Smith, D. R. & Mikkelsen, M. H. Toward

Multispectral Imaging with Colloidal Metasurface Pixels. *Adv. Mater.* **29,** (2017).

79. Bowen, P. T., Baron, A. & Smith, D. R. Theory of patch-antenna metamaterial perfect absorbers. *Phys. Rev. A* **93,** (2016).

80. Hoang, T. B., Huang, J. & Mikkelsen, M. H. Colloidal Synthesis of Nanopatch Antennas for Applications in Plasmonics and Nanophotonics. *J. Vis. Exp.* 1–8 (2016). doi:10.3791/53876

81. Maalouf, R. & Bailey, S. A review on B-type natriuretic peptide monitoring: assays and biosensors. *Heart Fail. Rev.* **21,** 567–578 (2016).

82. Benjamin, E. J. *et al.* Heart Disease and Stroke Statistics'2017 Update: A Report from the American Heart Association. *Circulation* **135,** e146–e603 (2017).

83. Ponikowski, P. *et al.* Heart failure: preventing disease and death worldwide. *ESC Hear. Fail.* **1,** 4–25 (2014).

84. Wei, Q. *et al.* Detection and spatial mapping of mercury contamination in water samples using a smart-phone. *ACS Nano* **8,** 1121–1129 (2014).

85. Wei, Q. *et al.* Fluorescent imaging of single nanoparticles and viruses on a smart phone. *ACS Nano* **7,** 9147–9155 (2013).

86. Palazzuoli, A., Gallotta, M., Quatrini, I. & Nuti, R. Natriuretic peptides (BNP and NT-proBNP): Measurement and relevance in heart failure. *Vasc. Health Risk Manag.* **6,** 411–418 (2010).

87. Hucknall, A., Rangarajan, S. & Chilkoti, A. In pursuit of zero: Polymer brushes that resist the adsorption of proteins. *Adv. Mater.* **21,** 2441–2446 (2009).

88. Whitesides, G. M. The origins and the future of microfluidics. *Nature* **442,** 368–373 (2006).

89. Juncker, D. *et al.* Autonomous microfluidic capillary system. *Anal. Chem.* **74,** 6139–6144 (2002).

90. Olanrewaju, A., Beaugrand, M., Yafia, M. & Juncker, D. Capillary microfluidics in microchannels: From microfluidic networks to capillaric circuits. *Lab Chip* **18,** 2323–2347 (2018).

91. De Gennes, P. G. Wetting: Statics and dynamics. *Rev. Mod. Phys.* **57,** 827–863 (1985).

92. Wyatt Shields, C., Cruz, D. F., Ohiri, K. A., Yellen, B. B. & Lopez, G. P.

Fabrication and operation of acoustofluidic devices supporting bulk acoustic standing waves for sheathless focusing of particles. *J. Vis. Exp.* **2016,** 1–7 (2016).

93. Tripathi, C. C., Jain, S., Joshi, P., Sood, S. C. & Kumar, D. Development of low cost set up for anodic bonding and its characterization. *Indian J. Pure Appl. Phys.* **46,** 738–743 (2008).

94. Mosterd, A. & Hoes, A. W. Clinical epidemiology of heart failure. *Heart* **93,** 1137–1146 (2007).

95. Inamdar, A. & Inamdar, A. Heart Failure: Diagnosis, Management and Utilization. *J. Clin. Med.* **5,** 62 (2016).

96. Benjamin, E. J. *et al. Heart Disease and Stroke Statistics-2019 Update: A Report From the American Heart Association*. *Circulation* **139,** (2019).

97. Heidenreich, P. A. *et al.* Forecasting the Impact of Heart Failure in the United States: A Policy Statement From the American Heart Association Council on Cardiovascular Radiology and Intervention, Council on Clinical Cardiology, Council on Epidemiology and Prevention, and Stroke C. *Circ Hear. Fail* **6,** 606–619 (2013).

98. McMurray, J. J. V. *et al.* ESC Guidelines for the diagnosis and treatment of acute and chronic heart failure 2012: The Task Force for the Diagnosis and Treatment of Acute and Chronic Heart Failure 2012 of the European Society of Cardiology. Developed in collaboration with the Heart. *Eur. Heart J.* **33,** 1787–1847 (2012).

99. Hawkins, N. M. *et al.* Heart failure and chronic obstructive pulmonary disease: Diagnostic pitfalls and epidemiology. *Eur. J. Heart Fail.* **11,** 130–139 (2009).

100. Kim, H. N. & Januzzi, J. L. Natriuretic peptide testing in heart failure. *Circulation* **123,** 2015–2019 (2011).

101. Ibrahim, N. E. & Januzzi, J. L. Established and emerging roles of biomarkers in heart failure. *Circ. Res.* **123,** 614–629 (2018).

102. Chow, S. L. *et al. Role of biomarkers for the prevention, assessment, and management of heart failure: A scientific statement from the American Heart Association*. *Circulation* **135,** (2017).

103. Kevin Range, and D. M. Y. A. M. Emerging Roles of Natriuretic Peptides and their Receptors in Pathophysiology of Hypertension and Cardiovascular Regulation. *Bone* **23,** 1–7 (2012).

104. Iqbal, N. *et al.* Cardiac biomarkers: new tools for heart failure management.

Cardiovasc. Diagn. Ther. **2,** 147–14764 (2012).

105. Masson, S. *et al.* Direct comparison of B-type natriuretic peptide (BNP) and amino-terminal proBNP in a large population of patients with chronic and symptomatic heart failure: The valsartan heart failure (Val-HeFT) data. *Clin. Chem.* **52,** 1528–1538 (2006).

106. Waldo, S. W. *et al.* Pro-B-Type Natriuretic Peptide Levels in Acute Decompensated Heart Failure. *J. Am. Coll. Cardiol.* **51,** 1874–1882 (2008).

107. Januzzi, J. L. *et al.* The N-terminal Pro-BNP investigation of dyspnea in the emergency department (PRIDE) study. *Am. J. Cardiol.* **95,** 948–954 (2005).

108. Potluri, S., Ventura, H. O., Mulumudi, M. & Mehra, M. R. Cardiac Troponin Levels in Heart Failure. *Cardiol. Rev.* **12,** 21–25 (2004).

109. Wettersten, N. & Maisel, A. Role of Cardiac Troponin Levels in Acute Heart Failure. *Card. Fail. Rev.* **1,** 102 (2015).

110. Berton, G. *et al.* C-reactive protein in acute myocardial infarction: Association with heart failure. *Am. Heart J.* **145,** 1094–1101 (2003).

111. Yin, W. H. *et al.* Independent prognostic value of elevated high-sensitivity C-reactive protein in chronic heart failure. *Am. Heart J.* **147,** 931–938 (2004).

112. Engström, G., Melander, O. & Hedblad, B. Carotid intima-media thickness, systemic inflammation, and incidence of heart failure hospitalizations. *Arterioscler. Thromb. Vasc. Biol.* **29,** 1691–1695 (2009).

113. Humeres, C. & Frangogiannis, N. G. Fibroblasts in the Infarcted, Remodeling, and Failing Heart. *JACC Basic to Transl. Sci.* **4,** 449–467 (2019).

114. Allen, J. K. *et al.* Community Outreach and Cardiovascular Health (COACH) trial: A randomized, controlled trial of nurse practitioner/community health worker cardiovascular disease risk reduction in urban community health centers. *Circ. Cardiovasc. Qual. Outcomes* **4,** 595–602 (2011).

115. van Kimmenade, R. R. *et al.* Utility of Amino-Terminal Pro-Brain Natriuretic Peptide, Galectin-3, and Apelin for the Evaluation of Patients With Acute Heart Failure. *J. Am. Coll. Cardiol.* **48,** 1217–1224 (2006).

116. devarajan, prasad. Neutrophil gelatinase-associated lipocalin: a promising biomarker for human acute kidney injury. **4,** 265–280 (2011).

117. Maisel, A. S. *et al.* Prognostic utility of plasma neutrophil gelatinase-associated

lipocalin in patients with acute heart failure: The NGAL EvaLuation Along with B-type NaTriuretic Peptide in acutely decompensated heart failure (GALLANT) trial. *Eur. J. Heart Fail.* **13,** 846–851 (2011).

118. Van Deursen, V. M. *et al.* Prognostic value of plasma neutrophil gelatinase-associated lipocalin for mortality in patients with heart failure. *Circ. Hear. Fail.* **7,** 35–42 (2014).

119. Bergeron, S., Laforte, V., Lo, P. S., Li, H. & Juncker, D. Evaluating mixtures of 14 hygroscopic additives to improve antibody microarray performance. *Anal. Bioanal. Chem.* **407,** 8451–8462 (2015).

120. Kricka, L. J. & Master, S. R. Quality control and protein microarrays. *Clin. Chem.* **55,** 1053–1055 (2009).

121. Dien et al., 2013. Facile Synthesis of Ag Nanocubes of 30 to 70 nm in Edge Length with CF3 COOAg as a Precursor. *Bone* **23,** 1–7 (2008).

122. Hoang, T. B., Huang, J. & Mikkelsen, M. H. Colloidal Synthesis of Nanopatch Antennas for Applications in Plasmonics and Nanophotonics. *J. Vis. Exp.* 1–8 (2016). doi:10.3791/53876

123. Shilo, M., Motiei, M., Hana, P. & Popovtzer, R. Transport of nanoparticles through the blood-brain barrier for imaging and therapeutic applications. *Nanoscale* **6,** 2146–2152 (2014).

124. Ankri, R., Peretz, D., Motiei, M., Sella-Tavor, O. & Popovtzer, R. New optical method for enhanced detection of colon cancer by capsule endoscopy. *Nanoscale* **5,** 9806–9811 (2013).

125. Peretz, V., Motiei, M., Sukenik, C. N. & Popovtzer, R. The Effect of Nanoparticle Size on Cellular Binding Probability. *J. At. Mol. Opt. Phys.* **2012,** 1–7 (2012).

Biography

Daniela Cruz received her Bachelor of Science degree from California State University Long Beach in 2012. She double majored in Electrical Engineering and Biomedical Engineering and served as the president of the Biomedical Engineering Society in 2011. She was also involved with the Society of Women Engineers, Society of Hispanic Professional Engineers (SHPE), Institute of Electrical and Electronics Engineers (IEEE), and was part of the Tau Beta Pi National Engineering Society. Daniela then entered the Pratt School of Engineering graduate program in the Biomedical Engineering at Duke in 2013 and joined the Lopez lab, where she worked on the assembly of plasmonic nanoparticles using acoustic fields. She later joined the Mikkelsen lab in 2015 and worked on the integration of plasmonics in planar immunoassays. Daniela received a fellowship to the NSF's Research Triangle MRSEC in 2014 and an NSF Graduate Research Fellowship in 2015. Daniela was also involved with SHPE at Duke where she served as a recruiter for the Pratt School of Engineering. A list of Daniela's publications can be found below.

1. Cruz, DF; Fontes, C; Chilkoti, A; Mikkelsen, MH. "Ultrabright Fluorescence Readout of a Point-of-Care Immunoassay using Plasmonic Metasurfaces" (Under Review).

2. Shields, CW; Cruz, DF; Ohiri, KA; Yellen, BB; López, GP. "Microfabrication of Continuous Flow Acoustofluidic Devices," Journal of Visualized Experiments: JoVE, (109) 2016.

3. Owens, CE; Shields IV, CW; Cruz, DF; Charbonneau, P; López, GP. "Highly parallel acoustic assembly of microparticles into well-ordered crystallites," ***Soft Matter***. 12.3 (2016): 717-728

4. Fu, L; Bian, C; Shields IV, CW; Cruz, DF; López, GP; Charbonneau, P. "Densest packings of hard sphere in a cylinder" ***Soft Matter***. 13.18 (2017): 3296-3306.

5. Yang, Y; Pham, AT; Cruz, DF; Reyes, B; López, GP; Yellen BB. “Assembly of Colloidal Molecules, Polymers and Crystals in Combined Acoustic and Magnetic Fields,” **Advanced Materials** 27.32 (2015): 4725-4731.

6. Cruz, DF; Khan, AH; Buma, T. “Elastomeric Photonic Crystals for Optoacoustic Detection of High Frequency Ultrasound,” IEEE Ultrasonic Symposium 2011. 1622: 234-237.